Superionic Noble Metal Chalcogenide Thermoelectrics

Thesis by

Tristan W. Day

In Partial Fulfillment of the Requirements

for the Degree of

Doctor of Philosophy

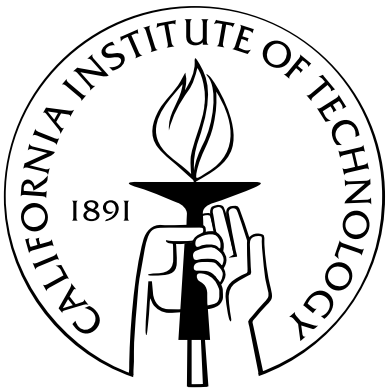

California Institute of Technology

Pasadena, California

2015

(Defended 15 May 2015)

Acknowledgments

The first and greatest acknowledgment is to my partner of over five years, Alice Robinson. Without her, this work would have been joyless and impossible.

I am grateful for endless support from my parents, Patrick and Marlena Day. Their belief in my abilities never faltered, especially when mine did.

I owe a debt to my first-year classmates Joey Ensberg, Jeff Bosco, Brett Babin, Amy Fu, Kai Yuet, and Devin Wiley for getting me through my classes and the dreaded qualifying exams.

I would like to thank Professors Rick Flagan and Julie Kornfield for being great advisors and human beings during the beginning of my time at Caltech. The three of us had a great adventure into the field of non-imaging solar concentrators, and I learned many skills from both of them. I would also like to thank them for their understanding and support as I moved to Professor Snyder's lab.

I owe many thanks to the members of my first lab, Jason Gamba, Andy Downard, Andy Metcalf, Xerxes Lopez-Yglesias, and Mandy Grantz for helping me find my way during my first two years at Caltech.

My advisor, Professor Jeff Snyder, has been great to work with. He struck a balance between providing enough guidance to get me started and giving me the independence I needed to make real progress. His jovial nature and laid-back attitude created a lab environment where people get along extremely well and make great scientific achievements because of that.

The members of the Snyder lab and the regular visitors from other labs taught me everything I needed to make my thesis work possible. I thank Aaron LaLonde for teaching me how to use all the instruments in the lab and how to make thermoelectric materials. Thanks to Nick Heinz, Zach Gibbs, Heng Wang, and Yanzhong Pei for illuminating discussions on electronic transport theory. Teruyuki Ikeda taught me a great deal about the nuts and bolts of the rapid hot press and the laser-flash thermal diffusivity analyzer every time we worked together to fix either of them; I thank him for his infinite patience. Wolfgang Zeier taught me the basics of solid-state chemistry and X-ray diffraction and helped elevate my writing above dry, line-by-line expositions. Kasper Borup lent a lot of support with instrumentation. Thanks to Fivos Drymiotis for lots of discussions on solid-state physics, possible new projects, and help with writing and editing. Thanks to Christophe Heinrich

and Kai Weldert for handling the solid-state synthesis side of collaborations with me. Special thanks to Brett Kauffman for working with me to construct a new rapid hot press. Brett consulted on the design of and fabricated all the new parts we needed to get the new press running. He has the patience of concrete, which is absolutely necessary when building a new instrument from scratch.

Ernie's Al Fresco provided hot, cheap, plentiful, and delicious food to keep me going every day. Many thanks to Ernie and the ladies.

Abstract

Measurements and modeling of Cu_2Se, Ag_2Se, and Cu_2S show that superionic conductors have great potential as thermoelectric materials. Cu_2Se and Ag_2Se are predicted to reach a zT of 1.2 at room temperature if their carrier concentrations can be reduced, and Cu-vacancy doped Cu_2S reaches a maximum zT of 1.7 at 1000 K. Te-doped Ag_2Se achieves a zT of 1.2 at 520 K, and could reach a zT of 1.7 if its carrier concentration could be reduced. However, superionic conductors tend to have high carrier concentrations due to the presence of metal defects. The carrier concentration has been found to be difficult to reduce by altering the defect concentration, therefore materials that are underdoped relative to the optimum carrier concentration are easier to optimize. The results of Te-doping of Ag_2Se show that reducing the carrier concentration is possible by reducing the maximum Fermi level in the material.

Two new methods for analyzing thermoelectric transport data were developed. The first involves scaling the temperature-dependent transport data according to the temperature dependences expected of a single parabolic band model and using all of the scaled data to perform a single parabolic band analysis, instead of being restricted to using one data point per sample at a fixed temperature. This allows for a more efficient use of the transport data. The second involves scaling only the Seebeck coefficient and electrical conductivity. This allows for an estimate of the quality factor (and therefore the maximum zT in the material) without using Hall effect data, which are not always available due to time and budget constraints and are difficult to obtain in high-resistivity materials.

Methods for solving the coherent potential approximation effective medium equations were developed in conjunction with measurements of the resistivity tensor elements of composite materials. This allows the electrical conductivity and mobility of each phase in the composite to be determined from measurements of the bulk. This points out a new method for measuring the pure-phase electrical properties in impure materials, for measuring the electrical properties of unknown phases in composites, and for quantifying the effects of quantum interactions in composites.

Contents

List of Figures

List of Tables

Chapter 1

Introduction

1.1 The thermoelectric effect

The thermoelectric effect is a phenomenon whereby two dissimilar parallel conductors in a temperature gradient (Figure 1.1) produce a voltage [1]. The charge carriers in each conductor diffuse from the side at temperature T_H to the side with temperature T_C, where T_H is greater than T_C. The resulting electric field balances with the temperature gradient driving force to establish a steady voltage V. Note that the voltage V is measured from the cold side to the hot side, so if the majority of the charge carriers are holes, V will be positive. If the majority of the charge carriers are electrons, V will be negative. This effect is also called the Seebeck effect, named after Thomas Johann Seebeck, who discovered it in 1822. The Seebeck coefficient S is defined as $dV/d\Delta T$, where ΔT is equal to $T_H - T_C$. S is a measure of the entropy transported per charged particle in the material. The more available states there are for the charge carriers, the greater S will be, i.e., S increases as the charge carrier concentration decreases. For metals, S is on the order of a few microvolts per Kelvin, for semiconductors, S is on the order of tens to hundreds of microvolts per kelvin, and for insulators S is on the order of hundreds to thousands of microvolts per kelvin.

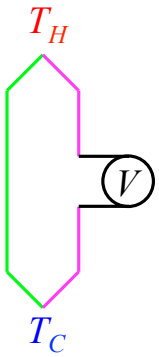

Figure 1.1: Two wires of different composition connected at both ends. The temperature difference from one end to the other creates a voltage.

If we connect alternating p-type materials (those with holes as the majority carriers) and n-type materials (those with electrons as majority carriers) electrically in series and thermally in parallel, (Figure 1.2(a)), and put the resulting thermoelectric module in a temperature gradient, the voltage it creates will be large enough to do useful electrical work, e.g., to drive a current I through the resistance R. Thermoelectric modules have been used this way to generate power for the Voyager space probes and the Mars Science Laboratory Curiosity rover [2]. Thermoelectrics are used for spacecraft power generation whenever the spacecraft is too far from the Sun to generate enough electricity (as on the Voyager probes [3]). Propane or natural-gas fired thermoelectric modules are used on Earth to augment solar power generation whenever reliable power is needed in remote places, such as on weather stations or radio repeaters. Thermoelectric modules have the potential to harvest waste heat from automobiles, industrial processes, and steam-based powerplants [3, 4].

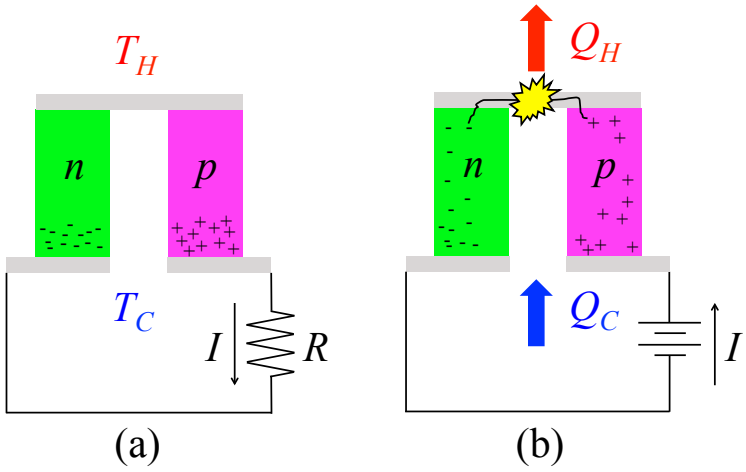

Figure 1.2: Figure 1.2(a) shows a module in a temperature gradient, which drives a current through the resistance R. Figure 1.2(b) shows an isothermal module connected to a battery, moving heat from one side to the other.

Figure 1.2(b)) shows a thermoelectric module at uniform temperature connected to a battery instead of a resistor. The battery drives a current I through the module, causing carrier recombination at the top of the module, releasing heat at a rate of Q_H. The carriers carry heat as well as charge, so heat is drawn into the bottom of the module at a rate of Q_C. Thermoelectric modules operated this way are used as solid-state coolers. Thermoelectric cooling is used on sensors in heat-seeking missiles and night-vision devices [3] because these applications require very compact cooling systems; thermoelectric modules can be made smaller than vapor-compression based systems of equal power rating [4].

Thermoelectrics have many advantages compared to other heat engines. They are solid-state devices, i.e., they have no moving parts, making them reliable and vibration-free. Power-generation thermoelectrics do not emit greenhouse gases and cooling thermoelectrics do not use greenhouse

or ozone-depleting gases. The major disadvantage of using thermoelectrics compared to vapor-compression systems, the reason why thermoelectrics have not replaced gasoline-fired automobile engines, coal-fired or nuclear steam generating plants, or greenhouse-gas based refrigerators is that they are much less efficient than those traditional heat engines and heat pumps.

1.2 Thermoelectric efficiency and zT

The efficiency of a thermoelectric material is governed by the dimensionless figure-of-merit, zT, equal to $S^2T/\rho\kappa$, where S is the Seebeck coefficient, T is the absolute temperature, ρ is the electrical resistivity, and κ is the thermal conductivity. This figure-of-merit is defined for a single material, and is distinct from the device-level figure-of-merit, ZT_{avg}, where T_{avg} is the average of the hot- and cold-side temperatures. ZT accounts for both n- and p-type materials and the geometry of the individual legs. The efficiency of a power-generating thermoelectric module η_{eff} is given by Equation 1.1 [5].

$$\eta_{eff} = \frac{T_H - T_C}{T_H} \frac{\sqrt{1 + ZT_{avg}} - 1}{\sqrt{1 + ZT_{avg}} + (T_C/T_H)} \tag{1.1}$$

The leading fraction on the right-hand side of Equation 1.1 is the Carnot efficiency, which is the same for any heat engine operating between T_H and T_C. The tailing fraction is roughly proportional to $\sqrt{ZT_{avg}}$, and it represents the irreversible losses of useful energy to electrical and thermal conduction. A similar equation holds for the coefficient of performance of a thermoelectric cooler.

The best thermoelectric materials in use today have zT around 1. For thermoelectrics to be used beyond niche applications and to be integrated into the global energy scheme, zT between 2 and 4 is needed [3, 4]. To understand how to increase zT, we show zT in Equation 1.2 in terms of the electrical conductivity σ for clarity and with κ as the sum of a lattice contribution κ_L and an electronic conductivity equal to $L\sigma T$, where L is the Lorenz number.

$$zT = \frac{S^2\sigma T}{\kappa_L + L\sigma T} \tag{1.2}$$

S decreases as a function of the carrier concentration n, but the electrical conductivity and the electronic thermal conductivity both increase with n (Figure 1.3). These relationships are at the center of the problem of increasing zT. There is an optimum carrier concentration n that maximizes zT. Thermoelectrics research is concentrated on achieving the optimum carrier concentration and on increasing the maximum possible zT.

zT can be increased by reducing the lattice thermal conductivity κ_L. Some ways of doing this include the use of secondary phases which scatter phonons [6], phonon-scattering nanostructuring [7], and alloying to create mass and strain contrast which reduce the phonon group velocity [8].

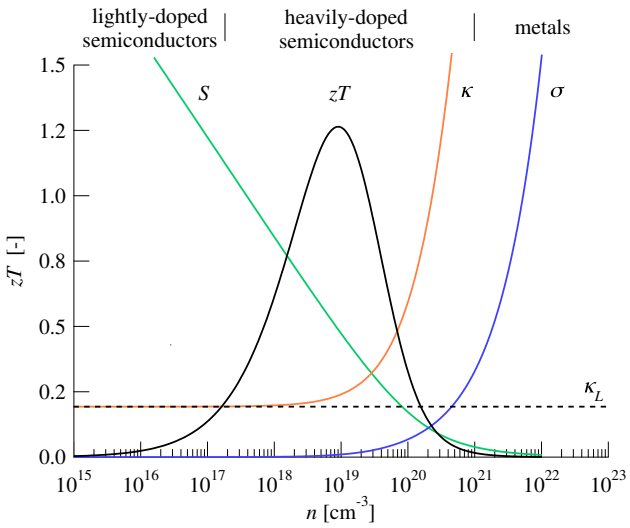

Figure 1.3: Relationships between components of zT. This figure shows that heavily doped semiconductors make the best thermoelectric materials.

zT can also be increased by increasing the so-called power factor $S^2\sigma$. This is challenging because S and σ are inversely proportional [9] and because increasing σ increases the electronic thermal conductivity. Some means of increasing the power factor include creating resonant states at the Fermi level [10], the convergence of electronic bands [11], charge carrier energy filtering [12], and charge carrier concentration optimization [9].

1.3 Summary of research

1.3.1 Superionic Noble Metal Chalcogenides

Looking at Equation 1.2 and keeping in mind that σ is equal to $ne\mu$, where n is the charge carrier concentration, e is the elementary charge, and μ is the charge carrier mobility, we see that materials with potentially high zT will have high charge carrier mobility values and low lattice thermal conductivity values. A class of materials with these attributes is the metal chalcogenides. These include PbTe [11] and alloys of $AgSbTe_2$ and GeTe, known as TAGS [13], both of which were used in radioisotope thermal generators (RTGs) on spacecraft, and Bi_2Te_3 [14], which is used in most thermoelectric refrigerators and spot-cooling modules.

An exciting new class of thermoelectrics is the superionic noble metal chalcogenides. Superionic materials are those that conduct metal ions with an ionic conductivity between 0.1 and 1 S cm^{-1} above a material-dependent transition temperature. Some examples are Ag_4RbI_5, AgI, and $Cu_4RbCl_3I_2$ [15]. The metal ions flow freely through the material while the anions remain fixed [15],

leading to low values of the lattice thermal conductivity [16]. The superionic noble metal chalcogenides are materials that conduct noble metals (those in the Cu column of the periodic table) in a fixed lattice of chalcogen atoms (S, Se, or Te), as shown in Figure 1.4. These materials have high enough charge carrier mobility to be considered for use as thermoelectrics, unlike the superionic conductors listed above. Superionic noble metal chalcogenides ensure a low lattice thermal conductivity; the bulk of the research on them in this thesis focuses on understanding and optimizing their electronic transport properties. These materials are always present with an excess or a deficiency of metal ions.

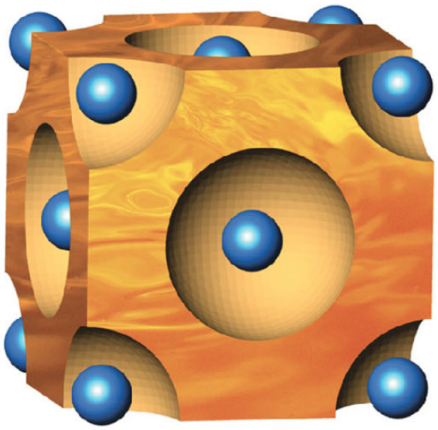

Figure 1.4: Illustration of superionic Cu_2S. The blue spheres are S atoms; the liquid-like mass is flowing Cu ions. Adapted from [17].

Some examples of superionic thermoelectrics are $AgCrSe_2$ [18], reported to reach a zT of 1 at 773 K, Ag_2Se [19, 20], reported to reach a zT of 1 at 300 K, Cu_2Se [16], reported to reach a zT of 1.5 at 1000 K, and Cu-vacancy doped $Cu_{2-x}S$ ($0 \leq x \leq 0.03$) [17], reported to reach a zT of 1.7 at 1000 K. This research is focused on characterizing and optimizing the thermoelectric properties of Ag_2Se, Cu_2Se, and Cu_2S both above their superionic transition temperatures and below them.

1.3.2 Potential for High zT

Theoretical curves of zT versus Hall carrier concentration n_H at different temperatures for Ag_2Se, $Ag_2Se_{1-x}Te_x$, Cu_2Se, and $Cu_{2-x}S$ are shown in Figure 1.5. Here we use the Hall carrier concentration n_H instead of the chemical carrier concentration n because n_H is experimentally accessible (see Section 3.2). As in Figure 1.3, each material has an optimum value of n_H at which zT is maximized. These materials all have lattice thermal conductivity values less than 1 W m^{-1} K^{-1} (Sections 4.2 and 5.4, [17, 21, 22, 23]), which contributes to high thermoelectric performance.

In general, the maximum attainable zT value increases with temperature (see Section 3.4), but Figure 1.5 shows that the predicted zT curves at temperatures greater than 520 K all have lower

maximum zT values. This is because all the materials studied above 520 K are copper chalcogenides, all of which have effective masses of 2 m_e or greater [17]. In general, increasing the effective mass reduces the maximum zT (Equation 3.35). The silver chalcogenides studied at 520 K all have effective masses of about 0.2 m_e (Section 5.4, [21]), which explains why they have greater maximum zT values.

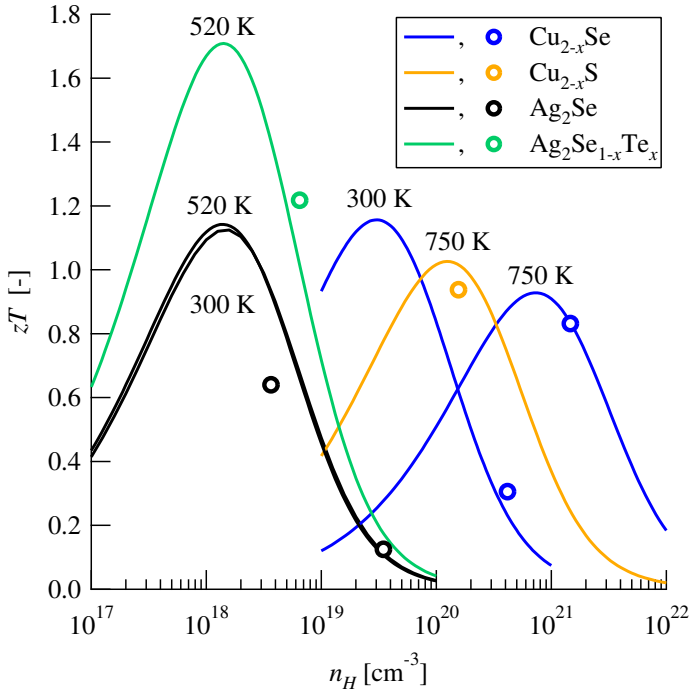

Figure 1.5: Comparison of maximum zT values for superionic noble metal chalcogenides. Curves are predictions of zT versus n_H, and points are those closest to the maximum zT values achieved so far.

The curves in Figure 1.5 at 300 K show that superionic noble metal chalcogenides have potential even in the non-ion conducting phase. This is because they have low-symmetry crystal structures, which provides a low-κ_L platform from which to develop thermoelectric materials. Superionic noble metal chalcogenides therefore have high potential as thermoelectrics due to low κ_L by different means at different temperatures.

Ag_2Se has nearly identical maximum zT values of nearly 1.2 and optimum n_H values around 10^{18} cm^{-3} between 300 K and 520 K. This is due to a shift between the mobility, effective mass, and lattice thermal conductivity across the superionic phase transition at 407 K that results in a constant quality factor (see Section 3.4). This is fortunate because optimum n_H values are usually not equal at different temperatures, which leads to a lower average zT in a given temperature range. This suggests that Ag_2Se could have high thermoelectric performance across a wide temperature range at low temperature (room temperature to 300°C) in a single composition, meaning it could

potentially be easy to implement as a thermoelectric cooler. However, its carrier concentration must be reduced from the high 10^{18} to low 10^{19} cm^{-3} range to about 1×10^{18} cm^{-3} [21].

One way of reducing the carrier concentration in Ag_2Se is to alloy it with Te to form $Ag_2Se_{1-x}Te_x$. Adding Te does not just reduce the carrier concentration; it also raises the maximum possible zT to 1.7 due to a reduction in the lattice thermal conductivity.

Cu_2Se also has potential for high thermoelectric performance at room temperature (maximum zT of 1.2), but its carrier concentration must be reduced from the middle 10^{20} cm^{-3} range to the low 10^{19} cm^{-3}.

At 750 K, $Cu_{2-x}S$ has greater potential for thermoelectric performance than does $Cu_{2-x}Se$ (maximum zT values of 1 and 0.9, respectively). Section 6.3 shows that this is because $Cu_{2-x}S$ has a lower lattice thermal conductivity, which is supported by speed of sound measurements.

1.3.3 Carrier Concentration Control

The potential for superionic conductors as thermoelectric materials is clear from Figure 1.5; each material potentially has zT values greater than or equal to 1 over a wide temperature range. However, to reach the maximum zT in each material, the carrier concentration must be controlled. With the exception of $Cu_{2-x}S$, the Hall carrier concentrations in the superionic noble metal chalcogenides in this thesis are between a factor of 2 and a factor of 10 greater than their optimum values. Superionic conductors in general have many defects, and therefore relatively high carrier concentrations, making their thermoelectric optimization a problem of removing charge carriers, rather than adding them to an intrinsic form of the material as in Bi_2Te_3 or PbTe.

Removing holes from copper selenide may be possible by adding n-type dopants. Section 4.2 shows that doping with Br on the Se site reduces the carrier concentration, but ultimately reduces the maximum potential zT through alloy scattering. A suitable dopant must be found that fills in holes but does not reduce the valence band mobility.

Silver selenide presents an even greater doping challenge because it is n-type. An acceptor must be found to remove electrons from the valence band. Even if this is possible, moving the Fermi level toward the conduction band minimum will induce bipolar conduction and reduce zT, as explained in Section 5.3. Alloying Ag_2Se with Te has been shown to reduce the carrier concentration (Section 5.4, [22]). Te is an isoelectronic substituent for Se, but it seems to reduce the carrier concentration by moving the n-type pinning energy (the maximum achievable Fermi level) toward the conduction band minimum. Other overdoped n-type superionic conductors may be susceptible to this kind of carrier-concentration reduction.

Copper sulfide is easy to optimize because it is underdoped; it is easy to synthesize the material with Cu vacancies, thereby raising the carrier concentration. Removing carriers from superionic conductors is difficult, as shown by the attempts to reduce the carrier concentrations of Cu_2Se

and Ag_2Se. Therefore, underdoped superionic noble metal chalcogenides are more likely to be low-hanging fruit for thermoelectrics researchers.

1.3.4 New Analysis and Measurement Methods

In the course of this study new methods for analyzing thermoelectric transport data were developed and an entirely new kind of measurement was devised for measuring the electronic properties of composites.

One method of determining the effective mass m^* and mobility parameter μ_0 of semiconductor materials is to make several samples with different doping levels, then measure them all at a range of temperatures. Then, curves of the Seebeck coefficient and Hall mobility versus the Hall carrier concentration at a fixed temperature are used to fit the effective mass and mobility parameter. Making the samples and measuring them consumes time and funding. While analyzing the transport data of $Ag_{2+x}Se$, we realized that the temperature-dependent transport data could be scaled by the temperature dependences expected from the single parabolic band model, allowing us to use the entire temperature-dependent data set to fit the effective mass and the mobility parameter at a fixed temperature [21]. Scaling the transport data instead of using only those points at a fixed temperature is a more efficient use of the data. Because more data points are available through temperature scaling, good estimates of m^* and μ_0 can be obtained with just one sample.

The method described above requires Hall effect measurements. It is not always possible to do these measurements, and other studies of interest may not include Hall data. For this reason we developed a method for estimating the thermoelectric quality factor (see Section 3.4), and thereby the maximum zT, without using Hall data. Plotting the Seebeck coefficient against the conductivity of samples with different doping levels at a fixed temperature and fitting the data to a curve allows an estimation of the weighted mobility, $\mu_0(m^*/m_e)^{3/2}$ [24]. Scaling the Seebeck coefficient and the conductivity with temperature makes more efficient use of the available data and yields a better estimate of the weighted mobility. After calculating the lattice thermal conductivity, for which Hall data are not required, the quality factor and the maximum zT can be estimated. Again, because multiple data points can be extracted from the temperature-dependent measurements, this can be done on a single sample, which is a very efficient way of determining whether the material merits further research based on the maximum possible zT. The details of both temperature-scaling techniques can be found in Section 3.3.

While measuring the thermoelectric properties of $Cu_{1.97}Ag_{0.03}Se$, it was found that below the superionic transition this material has a positive Seebeck coefficient and a negative Hall coefficient when both should be positive because Cu_2Se is p-type. The material is a composite of a matrix of low-mobility, p-type Cu_2Se and inclusions of high-mobility n-type CuAgSe. These inclusions were found to be the cause of the negative Hall coefficient. This effect was quantified by measuring the

resistivity tensor as a function of magnetic field strength, and then solving an effective medium model to extract the conductivity and mobility of the constituent phases. While effective medium theory has been in use since the early 20^{th} century, it has always been used to predict the properties of composites from known constituents, and never used to calculate the properties of the constituents from known composites. This new use of effective medium theory, demonstrated in Chapter 7 points out a method for calculating phase-pure transport properties in the presence of impurities, calculating transport properties of mixtures of phases of unknown composition, and quantifying the benefits of quantum interactions between phases, which are not described by classical effective medium theory.

Chapter 2

Experimental Methods

2.1 Synthesis and Chemical Characterization

2.1.1 General Methods

Bulk thermoelectric materials are made by first weighing out elements in the form of 2-3 mm shots or pellets or -120 mesh powder. The elements are stored inside vacuum desiccators or inside an Ar glovebox to avoid oxidation. Powders are weighed inside the Ar glovebox. After obtaining the desired amounts of each element, the elements are combined inside a fused quartz tube. A glass funnel is used to transfer powders into the tube to avoid loss of powder by sticking to the tube walls. When using powders, the powders must be transferred to the tube inside the glovebox, and then a valve must be fixed to the top of the tube before bringing it out of the glovebox.

The tubes are made by dividing an open-ended tube with a methane/oxygen flame to create two tubes, each with one sealed end. The flame is run along the outer surface of each tube to smooth out imperfections in the quartz. The flame is applied to the rim of the open end to remove any sharp edges. The tube is filled with acetone up to about 5 cm, and then emptied. Immediately afterward, the flame is run along the outside of the tube, pyrolyzing the acetone to leave a carbon coating on the inner surface of the tube. This coating prevents reaction of the elements with the quartz. The flame is then applied to a point about 6 cm above the tube bottom while rotating the tube to create a neck. After loading the elements into the tube, a solid fused quartz plug of outer diameter just under the inner diameter of the tube is dropped into the tube.

The element-laden tube is connected to a vacuum pumping system. A rotary-vane pump provides an initial rough vacuum of about 800 mtorr, and then a diffusion pump provides a vacuum of about 5×10^{-5} torr. When using powders, the valves to the vacuum system must be opened slowly to avoid aspirating the powder into the vacuum pump. Once a vacuum of 5×10^{-5} torr is achieved, the flame is applied to the tube section containing the solid plug. The quartz will soften and weld to the plug as the atmosphere pushes the weakened material inward. The flame is moved around the entire

circumference of this section to create a seal. Air is admitted to the section of the tube above the plug, and the flame is applied to a point above the elements and below the plug. The quality of the seal is verified by observing the tube wall bow inward.

The sealed tube, now called an ampoule, is placed in a resistively-heated furnace. When using shots or pellets, the elements are ramped at 100 K h^{-1} to about 20 K above the melting point of the compound to achieve mixing. Then the mixture is lowered to a suitable annealing temperature below the melting point and held at that temperature for a few days. The resulting ingot can either be quenched in water or allowed to cool slowly to room temperature.

The ingot is checked for phase purity with X-ray diffraction, then either cut into disks on which measurements can be performed or ground into powder in a mortar and pestle or a high-energy ball mill. The powder is hot-pressed to form disks for measurements.

Melting is a suitable technique for simple binary materials, but for tertiary materials or incongruently melting materials, solid-state powder synthesis is a better option. The metal powders come from the supplier with some oxide content. This is removed by heating the powders at 523 K under flowing forming gas (95% argon, 5% hydrogen by volume) for five hours. In this technique, the powder mixture is heated to a temperature below the melting point, but high enough to cause diffusion. It is held at this temperature for one to several days. The mixture is taken out of the ampoule and ground in a mortar and pestle. X-ray diffraction is performed on the mixture to check its phase purity, and returned to the furnace if any secondary phases are present. Once the powder is phase-pure, it is hot-pressed into disks.

The rapid hot press is a custom-built instrument [25]. It is comprised of a Centorr vacuum chamber and roughing/diffusion pump train, an Instron 5500 lbf load frame, and a Superior Induction 25 kW 80 kHz RF power supply. The powder is placed into a Grafoil lined cylindrical graphite susceptor called a die. A graphite rod is placed inside the die on top of the powder. The die is placed inside a coil of copper tubing inside the vacuum chamber. The die rests on a hydraulic ram. The chamber is evacuated to 5×10^{-5} torr, then the load is increased to 40-100 MPa. The hydraulic ram presses the die upward against a post on the ceiling of the chamber. After compressing the powder, Ar is flowed through the chamber to suppress evaporation of the powder. The RF power supply is used to raise the temperature of the die at a peak rate of 600 K min^{-1} to a set point. After applying heat and force to the powder this way, the load is released and the die is allowed to cool down.

After extracting the disk from the die, the Grafoil is shaved from the disk with a razor blade. The disk will not always have parallel faces, so the disk must be ground down with SiC paper to achieve flat, parallel faces, which are necessary for the thermoelectric properties measurements. The disk is then checked for phase purity with X-ray diffraction (XRD).

2.1.2 Silver selenide

Compositions of $Ag_{2+x}Se$ with x equal to 0, 0.0006, and 0.0027 were synthesized. Polycrystalline ingots were prepared by melting Ag (shot, 99.9999% pure, Alfa Aesar, Puratronic) and Se (shot, 99.999% pure, Alfa Aesar, Puratronic) in the desired mass ratios inside fused quartz ampoules evacuated to less than 6×10^{-5} torr. The elements were slowly brought to 1273 K, held at that temperature for 12 h, cooled to 973 K over 3 hours, annealed at 973 K for three days, and then quenched in water. Disk-shaped samples were cut from the ingots.

The remaining materials were cut into ∼6 mm pieces and ball-milled to form powders. The powders were hot-pressed at 973 K and 40 MPa for four hours under flowing argon, and then held in the hot press at 673 K and ambient pressure for two hours to relieve any internal stresses. The geometric densities of all samples were greater than 95% of their theoretical values.

An additional sample of silver selenide was synthesized by a solid state reaction. Ag (powder, -120 mesh, 99.9999% pure, Alfa Aesar, Puratronic) and Se (powder, -100 mesh, 99.999% pure, Alfa Aesar, Puratronic) were ground together in an agate mortar and pestle in an Ar glovebox, then sealed in a quartz ampoule evacuated to less than 6×10^{-5} torr. The ampoule was heated to 673 K at 100 K h^{-1}, then held at 673 K for 24 hours. The ampoule was cooled slowly to room temperature inside the furnace. The resulting powder was ground in a mortar and pestle in the Ar glovebox, and then hot-pressed at 673 K and 40 MPa for 10 minutes.

XRD was performed on a Phillips PANalytical X'Pert Pro with CuKα radiation ($\lambda_1 = 1.540590$ Å, $\lambda_2 = 1.544310$ Å) and a 2θ step size of 0.008° (Figure 2.1). Comparing the hot-pressed diffraction patterns with the reference pattern, it is clear that the resulting pellets have no impurity phases.

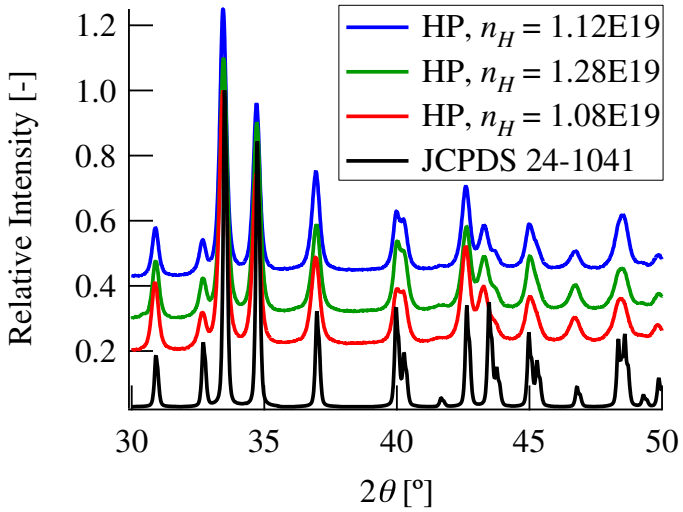

Figure 2.1: Diffraction patterns of hot-pressed $Ag_{2+x}Se$. The reference pattern JCPDS 24-1041 is from [26]. Adapted from [21] with permission from The Royal Society of Chemistry.

The differences in the transport properties between the ingot, hot-pressed, and solid-state reaction samples suggest that silver selenide is sensitive to the manner in which it is synthesized. The ingot samples had room temperature carrier concentrations between 5-7$\times 10^{18}$ cm^{-3}. The hot-pressed samples had carrier concentrations around 1×10^{19} cm^{-3}. The hot-pressed samples were ball-milled before being hot-pressed, so it is not clear which process increased the carrier concentration. The sample made by solid state reaction followed by hot-pressing had a carrier concentration of 6×10^{18} cm^{-3}. This implicates ball-milling as the process that increases the carrier concentration. The high-energy impacts of the balls on the materials may cause sufficient local heating to sublimate Se out of the material, thereby raising the carrier concentration.

2.1.3 Tellurium-doped silver selenide

Ag, Te, and Se shot, all of purity 99.999%, were placed in quartz tubes in the molar ratio 2:0.5:0.5. The quartz tubes were then evacuated, sealed, and placed inside a box furnace. The samples were subsequently heated to 1273 K, where they were allowed to remain for 5 hours, before finally being allowed to cool down to 573 K at a rate of 10 K h^{-1}, at which point the power to the furnace was turned off. The formed ingots were removed from the quartz tubes and processed for measurement. Disks of 8 mm diameter and approximately 2 mm thickness were cut from the ingots. The measured density of the disks was 8.2 g cm^{-3}.

XRD was performed on a Phillips PANalytical X'Pert Pro with CuKα radiation ($\lambda_1 = 1.540590$ Å, $\lambda_2 = 1.544310$ Å) and a 2θ step size of 0.008°. Figure 2.2 shows a shift in the peaks assigned to $Ag_2Se_{0.5}Te_{0.5}$ to lower 2θ relative to the reference pattern for Ag_2Se. This is consistent with larger Te occupying Se sites and increasing the size of the unit cell.

2.1.4 Silver-doped copper selenide

Ingots of Cu_2Se, $Cu_{1.98}Se$, $Cu_{1.97}Ag_{0.03}Se$, and $Cu_{1.97}Ag_{0.03}Se_{1.009}$ were formed by melting Cu (shot, 99.9999% pure, Alfa Aesar, Puratronic), Ag (shot, 99.9999% pure, Alfa Aesar, Puratronic), and Se (shot, 99.999% pure, Alfa Aesar, Puratronic) in quartz ampoules evacuated to less than 6×10^{-5} torr. The ampoules were ramped to 1373 K at 100 K h^{-1}, held at that temperature for 12 hours, and then quenched. The ingots were ball-milled to form powders, and then re-sealed in quartz ampoules, heated at 1273 K for 5 days, cooled to 973 K, held at that temperature for 3 days, and then quenched. The ingots thus obtained were ball-milled again and then hot-pressed at 973 K and 40 MPa for 6 hours. The geometric densities of the hot-pressed pellets were greater than 95% of their theoretical values.

XRD of $Cu_{1.97}Ag_{0.03}Se$ was performed on a Rigaku SmartLab diffractometer equipped with a CuKα source, parallel beam optics, and a Rigaku D/tex detector. Figure 2.3 shows that below the

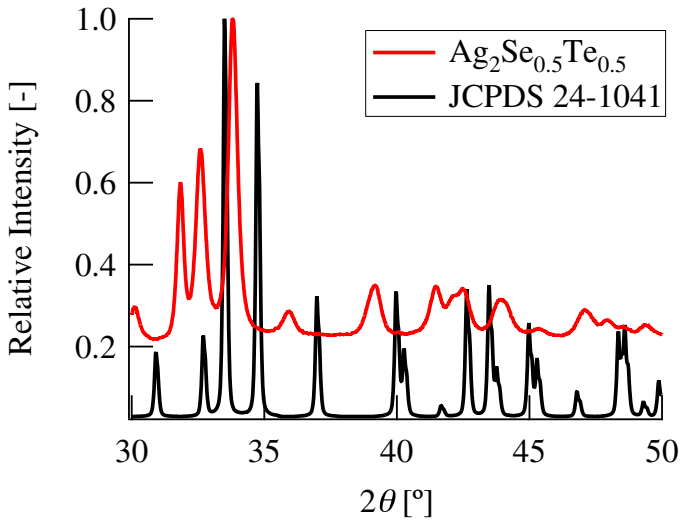

Figure 2.2: Diffraction patterns of ingot $Ag_2Se_{0.5}Te_{0.5}$. The reference pattern JCPDS 24-1041 is from [26].

superionic phase transition, $Cu_{1.97}Ag_{0.03}Se$ is a composite of a phase with the same crystal structure as Cu_2Se and a phase with the same crystal structure as CuAgSe.

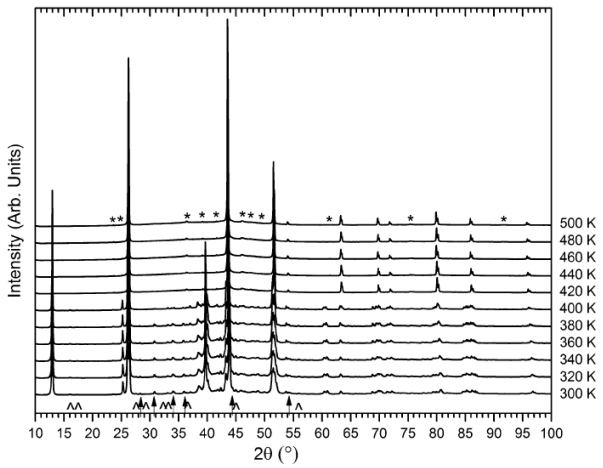

Figure 2.3: Temperature-resolved diffraction patterns of ingot $Cu_{1.97}Ag_{0.03}Se$. On the bottom, arrows mark CuAgSe peaks, while hat symbols mark impurities that dissolve at the phase transition. Asterisks mark the stable impurity peaks. Unmarked peaks on the bottom have corresponding peaks in the low-temperature structure of Cu_2Se. Reproduced with permission from Springer from [23].

XRD of Cu_2Se was performed on a Phillips PANalytical X'Pert Pro with CuKα radiation (λ_1 = 1.540590 Å, λ_2 = 1.544310 Å) and a 2θ step size of 0.008°.

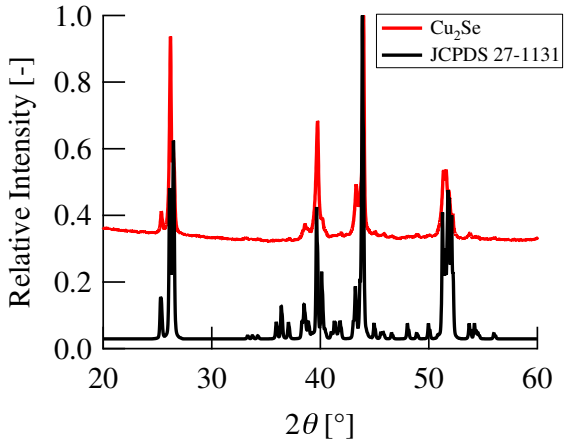

Figure 2.4: The reference pattern JCPDS 27-1131 is from [27].

2.1.5 Bromine-doped copper selenide

Cu (powder, 99.999% pure, Alfa Aesar), Se (powder, 99.999% pure, Alfa Aesar), and CuBr (powder, 99.999% pure, Sigma Aldrich) were ground in a mortar and pestle in the ratio 2:1-x:x, with x equal to 0 and from 0.02 to 0.05 in steps of 0.01, and then sealed in quartz ampoules under vacuum. The powders were ramped to 1423 K at 5 K min^{-1} and held for one hour, and then annealed at 1073 K for 48 hours. The obtained ingots were ground in a mortar and pestle, and then annealed at 1073 K for 48 hours. The ingots were ground again, and then hot-pressed at 773 K at 80 MPa for 10 minutes.

X-ray diffraction patterns were recorded with a Siemens D5000 diffractometer equipped with a Braun M50 position sensitive detector in transmission mode using Ge (200) monochromatized CuKα radiation. Samples were prepared between two layers of Scotch Magic tape.

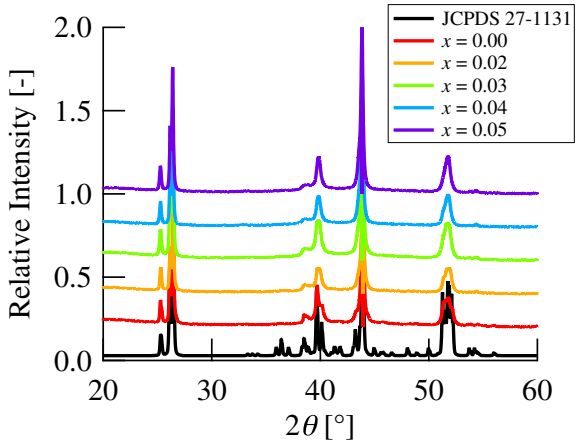

Figure 2.5: XRD patterns for $Cu_2Se_{1-x}Br_x$. The reference pattern JCPDS 27-1131 is from [27].

Since Br is nearly the same size as Se, no shift in the peaks shown in Figure 2.5 is observed, consistent with no change in the lattice parameters due to Br doping.

2.1.6 Copper sulfide

$Cu_{2-x}S$ samples were prepared by directly melting the elements Cu (shots, 99.999%, Alfa Aesar) and S (pieces, 99.999%, Alfa Aesar) in sealed silica tubes under vacuum. The element mixtures (the reported compositions are nominal compositions) were heated at a rate of 4 K min^{-1} to 1383 K and then held at this temperature for 18 hours to ensure complete melting of all elements before quenching in ice water. Next, the ingots were ground into fine powders, and then pressed into pellets for annealing at 833 K for 7 days. Finally, the obtained pellets were crushed into powders and consolidated by spark plasma sintering (Sumitomo SPS-2040) at 713 K under a load of 65 MPa for 5 minutes.

XRD of $Cu_{2-x}S$ was performed on a Rigaku Ultima IV with CuKα radiation and a 2θ step size of 0.02°.

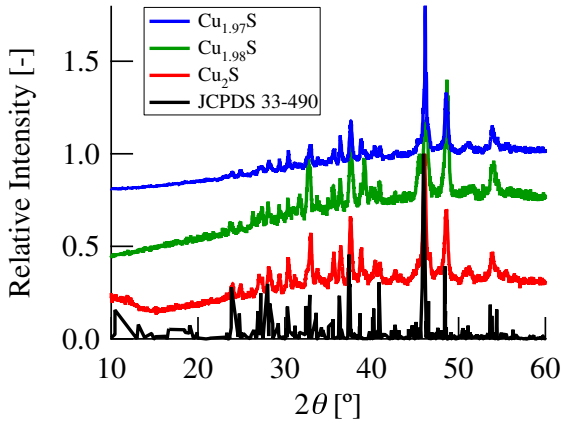

Figure 2.6: XRD patterns for $Cu_{2-x}S$. The reference pattern JCPDS 33-490 is from [28].

2.2 Measurement of Transport Properties

The Seebeck coefficient was measured on a custom-built instrument [29]. The sample is placed between two boron nitride heater blocks and then placed in thermal and electrical contact with two Nb/Chromel thermocouples. The measurement is run under vacuum. The control software oscillates the temperatures of the heater blocks such that the sample is exposed to a range of ΔT values at a constant average temperature T_{avg}. The voltage V produced by the Seebeck effect is measured for each value of ΔT (Figure 2.8). The Seebeck coefficient is the slope of the curve of V versus ΔT. This procedure is repeated at a specified set of average temperatures.

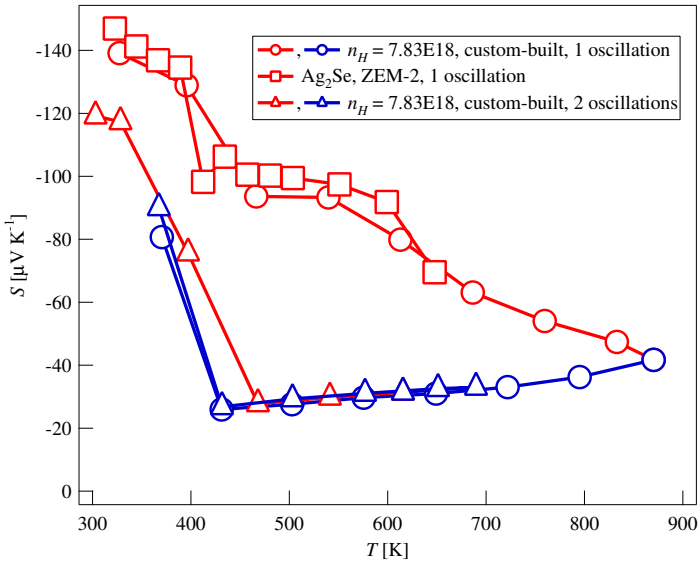

Figure 2.7: Comparison of Seebeck data obtained from using one full cycle versus two full cycles at each average temperature.

Care must be taken when measuring the Seebeck coefficient of superionic conductors using this method. Figure 2.7 shows the Seebeck versus temperature curves for two samples of silver selenide. Sample 1 was measured on the custom-built apparatus in Professor Snyder's lab, and Sample 2 was measured on a ZEM-2 commercial instrument at the University of South Carolina. Red curves are those taken on heating, blue on cooling. Using one full cycle per average temperature, as shown in Figure 2.8, produces heating and cooling curves that do not coincide. This indicates that something is wrong with either the sample or the measurement methodology. The samples were made independently by different researchers using different methods, and the heating curves of the two samples coincide. Using two full cycles per average temperature results in coincident heating and cooling curves. This suggests that there is a slow, transient process in silver selenide that results in erroneously high Seebeck values on heating, and that using two full cycles per Seebeck measurement allows this transient to decay. It was cautiously assumed that all usperionic conductors behave this way, and for this reason, all Seebeck measurements of superionic conductors were measured using two cycles.

The electrical resistivity ρ and the Hall coefficient R_H were measured on a custom-built apparatus [30]. These measurements were done in vacuum. Both quantities were measured using van der Pauw geometry, and the Hall coefficient was measured in a magnetic field of 2 T. If the electrical transport in the material is known to be influenced by a single band, the Hall carrier concentration n_H can be obtained by the relation $R_H = 1/n_H e$, and the Hall mobility μ_H from the relation $\mu_H = R_H/\rho$.

The thermal diffusivity α was measured on a Netzsch LFA-457 laser flash thermal diffusivity analyzer under flowing argon at a flow rate of 75 ml min^{-1}. The thermal conductivity κ was

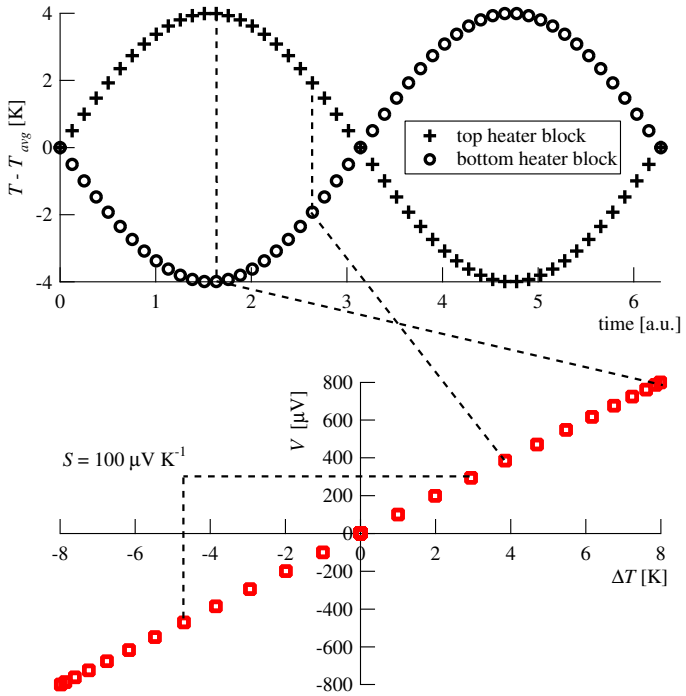

Figure 2.8: One full cycle of the Seebeck measurement. Each value of ΔT in the top graph corresponds to a voltage value in the bottom graph.

calculated from the relation $\kappa = \alpha d C_P$, where d is the density of the material and C_P is the constant pressure heat capacity. C_P can be estimated from the Dulong-Petit rule, $C_P = 3R/\bar{M}$, where R is the gas constant and $\bar{M}$ is the average molecular weight, or C_P can be measured separately.

The longitudinal speed of sound v_l and the shear speed of sound v_s can reveal information about phonon and electron scattering mechanisms. The speed of sound was measured in the laboratory of Professor W. L. Johnson using a Panametrics NDT 5800 pulser/receiver and 5 MHz and 25 MHz shear and longitudinal transducers from Ultran. The lowpass filter on the pulser/receiver was set to 35 MHz and the highpass filter was set to 1 MHz. The data were recorded on a Tektronix TDS 1012 digital oscilloscope. The speed of sound was estimated by dividing double the sample thickness by the average transit time as determined by the length of time between peaks.

Chapter 3

Charge Carrier Transport Modeling

3.1 Boltzmann Transport Equation

The equation governing the transport of particles with some distribution f of velocities $\vec{v}$ and positions $\vec{x}$ as a function of time t is the Boltzmann transport equation [1], given in Equation 3.1. In this work the term "charge carrier" refers either to an electron or a hole, and not to mobile ions, which also carry charge.

$$\frac{\partial f}{\partial t} + \vec{a} \cdot \nabla_v f + \vec{v} \cdot \nabla_x f = \left[\frac{\partial f}{\partial t}\right]_{coll} \tag{3.1}$$

$\vec{a}$ is the acceleration of the particles. The right hand side of Equation 3.1 is the result of the collision operator on $\partial f/\partial t$, which quantifies how $\partial f/\partial t$ is changed after a collision [1]. It can be shown that the right hand side of Equation 3.1 is equal to $-(f - f_0)/\tau$, where f_0 is the velocity and position distribution at equilibrium, and τ is the relaxation time, i.e. the length of time f takes to return to f_0 after a perturbation.

We are interested in the effects of electric fields $\mathscr{E}$ and temperature gradients $\partial T/\partial x$ in the x direction on the transport of charged particles. Assuming these are the only driving forces present in the system and that the system is at steady state ($\partial f/\partial t = 0$), the Boltzmann transport equation takes on the form in Equation 3.2, where e is the elementary charge, m^* is the mass of a particle, and u is the velocity in the x direction.

$$\frac{-e\mathscr{E}}{m^*}\frac{\partial f}{\partial u} + u\frac{\partial f}{\partial x} = -\frac{f - f_0}{\tau} \tag{3.2}$$

The electric fields and temperature gradients we are concerned with in thermoelectrics are very small, meaning the system is perturbed from equilibrium only slightly. This allows us to substitute the equilibrium distribution f_0 for f in the left hand side of Equation 3.2 and obtain the solution

for f, given in Equation 3.3.

$$f = f_0 - \tau\left(\frac{-e\mathscr{E}}{m^*}\frac{\partial f_0}{\partial u} + u\frac{\partial f_0}{\partial x}\right) \tag{3.3}$$

Now that we know the distribution f, we can integrate f to obtain electrical and thermal current densities if we know the forms of f_0 and τ. Since electrons are fermions, we use the Fermi distribution given by Equation 3.4, where E is the charge carrier energy and E_F is the Fermi level, both referenced to the energy band extremum. k_B is Boltzmann's constant.

$$f = \frac{1}{1 + e^{\frac{E-E_F}{k_B T}}} \tag{3.4}$$

For the relaxation time τ, we substitute the energy dependence given by Equation 3.5. The constants τ_0 and λ depend on the dominant charge carrier scattering mechanism [31].

$$\tau = \tau_0 \epsilon^{\lambda - 1/2} \tag{3.5}$$

Integrating Equation 3.4 yields the transport properties we are interested in as functions of integrals of τ and ϵ (Equations 3.6 through 3.10).

$$n_H = \frac{8\pi}{3}\left(\frac{2m^* k_B T}{h^2}\right)^{3/2} \frac{\left(\int_0^\infty \epsilon^{3/2}\tau\left(-\frac{\partial f}{\partial \epsilon}\right)d\epsilon\right)^2}{\int_0^\infty \epsilon^{3/2}\tau^2\left(-\frac{\partial f}{\partial \epsilon}\right)d\epsilon} \tag{3.6}$$

$$S = \frac{k_B}{e}\frac{\int_0^\infty \epsilon^{3/2}\left(\epsilon - \eta\right)\tau\left(-\frac{\partial f}{\partial \epsilon}\right)d\epsilon}{\int_0^\infty \epsilon^{3/2}\tau\left(-\frac{\partial f}{\partial \epsilon}\right)d\epsilon} \tag{3.7}$$

$$\mu_H = \frac{e}{m^*}\frac{\int_0^\infty \epsilon^{3/2}\tau^2\left(-\frac{\partial f}{\partial \epsilon}\right)d\epsilon}{\int_0^\infty \epsilon^{3/2}\tau\left(-\frac{\partial f}{\partial \epsilon}\right)d\epsilon} \tag{3.8}$$

$$L = \left(\frac{k_B}{e}\right)^2 \frac{\mathscr{K}_1\mathscr{K}_3 - \mathscr{K}_2^2}{\mathscr{K}_1^2} \tag{3.9}$$

$$\mathscr{K}_n = \int_0^\infty \epsilon^{n+1/2}\tau\left(-\frac{\partial f}{\partial \epsilon}\right)d\epsilon \tag{3.10}$$

If multiple scattering mechanisms contribute to scattering, then the reciprocals of the individual scattering times τ_i are added to obtain the total scattering rate τ^{-1}, given by Equation 3.11.

$$\tau^{-1} = \sum_i \tau_i^{-1} \tag{3.11}$$

Assuming a single scattering mechanism (except for ionized impurity scattering, which has a $\ln(\epsilon)$

dependence [32]) yields the transport properties as functions of Fermi integrals of order j, given by Equation 3.12. ϵ is the dimensionless charge carrier energy, E/k_BT, and η is the dimensionless Fermi level, E_F/k_BT.

$$F_j(\eta) = \int_0^\infty \frac{\epsilon^j d\epsilon}{1 + e^{\epsilon - \eta}} \tag{3.12}$$

The charge carrier scattering mechanism will determine the order j. In general, at room temperature and above, most charge carriers are scattered by acoustic phonons. We can confirm this by looking at a plot of the charge carrier mobility μ versus temperature. If acoustic phonon scattering is the dominant scattering mechanism, μ will be proportional to T^{-p}, with the value of p between 0.5 and 1.5.

Note that including multiple scattering mechanisms with different dependences on ϵ means that Equations 3.6 through 3.10 will not reduce to functions of Fermi integrals, and that the full integrals of ϵ and τ must be used.

3.2 Single Parabolic Band Model

We now have a framework for calculating transport properties, including the Seebeck coefficient, electrical resistivity, and electronic thermal conductivity. Before we apply this framework, we need to know something about the dispersion of charge carrier energy states in the material. Charge carrier energy states are built up from interactions between the charge carriers and the lattice. These states are grouped into regions in energy-momentum space called bands. An electron with momentum p, with p equal to $\hbar k$, where $\hbar$ is Planck's constant divided by 2π and k is the wavevector, has energy E given by Equation 3.13. This is referred to as a parabolic energy dispersion [33]. Other energy dispersions or bands exist, such as Kane bands [34] and linear dispersions [35], but we can confirm a parabolic energy dispersion by the behavior of the transport properties. A transport model that assumes a parabolic energy dispersion of a single band contributing to conduction is called a single parabolic band, or SPB model.

$$E = \frac{\hbar^2 k^2}{2m^*} \tag{3.13}$$

The number of bands contributing to conduction can be confirmed by the temperature dependence of the transport properties. Since the Seebeck voltages generated by electrons and holes will cancel one another out and lead to reduced Seebeck coefficients, a Seebeck coefficient that increases with temperature monotonically indicates that only one type of band is present. Electrons and holes both contribute to conduction; an exponential increase in the electrical conductivity (or decrease in the resistivity) indicates the presence of both types of charge carriers. It is possible for two bands

of the same carrier type to contribute to conduction as well. This effect can be observed as a shift in the effective mass.

m^* in Equation 3.13 is referred to as the effective mass, and is related to the curvature of the band by Equation 3.14. In general, the effective mass is an anisotropic quantity. However, without detailed knowledge of the band structure, the effective mass obtained by the single parabolic band model will be an average of the effective masses of all the bands contributing to conduction. Conversely, the single parabolic band model assumes a single value of the effective mass. The model is sometimes called the effective mass model for that reason [23]. The effective mass obtained by the single parabolic band model may change with temperature. This can indicate changing band offsets in $E-k$ space, or it can indicate band nonparabolicity. By definition, the single parabolic band model cannot explain these effects, but it remains a useful tool for predicting transport properties and optimizing thermoelectric performance.

$$m^* = \hbar^2 \left(\frac{\partial^2 E}{\partial k^2} \right)^{-1} \tag{3.14}$$

The following equations are valid for acoustic phonon scattering as the dominant scattering mechanism [31].

The Seebeck coefficient S is given by Equation 3.15. S depends only on the dimensionless Fermi level η. Equation 3.15 is always positive, so a negative sign must be multiplied by the right hand side of Equation 3.15 for n-type materials.

$$S = \frac{k_B}{e} \left(\frac{2F_1}{F_0} - \eta \right) \tag{3.15}$$

The chemical carrier concentration n is given by Equation 3.16. h is Planck's constant. n is not directly accessible by experiment; however, we can determine the Hall carrier concentration n_H from measurements of the Hall coefficient R_H and the relation $R_H = 1/n_H e$. n_H is equal to n/r_H; r_H is given by Equation 3.17. Both n and n_H are positive, so a negative sign must be added for n-type materials.

$$n = 4\pi \left(\frac{2m^* k_B T}{h^2} \right)^{3/2} F_{1/2} \tag{3.16}$$

$$r_H = \frac{3}{2} F_{1/2} \frac{F_{-1/2}}{2F_0^2} \tag{3.17}$$

The effective mass m^* is used as a fitting parameter to fit a theoretical curve of S versus n_H at a fixed temperature. Plots of S or μ_H versus n_H are referred to as Pisarenko plots [36].

The Hall mobility is obtained by dividing the Hall coefficient R_H by the electrical resistivity ρ. ρ is equal to $1/n_H e \mu_H$. The Hall mobility differs by a factor of r_H from the charge carrier mobility μ

discussed in the introduction. Again, μ_H is accessible by experiment, so our discussion of the charge carrier mobility will be in terms of the Hall mobility. The Hall mobility is given by Equation 3.18. μ_0 is the mobility parameter. The physical significance of the mobility parameter depends on the scattering mechanism. For acoustic phonon scattering, μ_0 is the mobility of a single charge carrier in a nondegenerate band. For ionized impurity scattering, it is the mobility of a single charge carrier when the ionized impurities are completely screened, i.e., in a degenerate band. μ_0 is related to the relaxation time τ and the effective mass m^* by Equation 3.19. μ_H is the average mobility of the charge carriers in the band. Since only charge carriers within $2k_BT$ of the Fermi energy E_F can reach unfilled energy states and move, the Hall mobility is reduced relative to the mobility parameter by charge carriers with zero mobility. μ_0 is used as a fitting parameter to fit a theoretical curve of μ_H versus n_H at a fixed temperature.

$$\mu_H = \mu_0 \frac{F_{-1/2}}{2F_0} \tag{3.18}$$

$$\mu_0 = \frac{e\tau_0}{m^*} \tag{3.19}$$

The electrical conductivity σ is calculated using Equation 3.20.

$$\sigma = n_H e \mu_H \tag{3.20}$$

The Lorenz number is the only undetermined part of the elecronic thermal conductivity LT/ρ, and is given by Equation 3.21.

$$L = \left(\frac{k_B}{e}\right)^2 \frac{3F_0F_2 - 4F_1^2}{F_0^2} \tag{3.21}$$

With L in hand, we can compute the lattice thermal conductivity κ_L from Equation 3.22.

$$\kappa_L = \kappa - \frac{LT}{\rho} \tag{3.22}$$

3.3 Scaled Single Parabolic Band Models

The procedure above is carried out at fixed temperature. The temperature T and the Fermi level η as represented by the Hall carrier concentration are both thermodynamic variables. We fix the temperature T in order to determine m^* and μ_0, which relate the transport properties to the Fermi level. This implies that each sample made yields one ordered pair each of S versus n_H and μ_H vs n_H at a given temperature T. Samples cost time and money to make, and it would be better if we could use the data at all temperatures measured, and not just those at the temperature of

interest. Therefore a new technique for analyzing thermoelectric transport data was developed in the course of the research in this thesis: the scaled effective mass model. We know how the Seebeck coefficient and the Hall mobility should scale with temperature. We can normalize the data by these temperature dependences and use the data at all temperatures to perform an analysis at a temperature of interest. In the degenerate limit, S is proportional to T [1]. This is expressed in Equation 3.23, which indicates the Seebeck coefficient at the temperature of interest T_{scale} and at the actual measured Hall carrier concentration $n_H(T)$ is equal to the Seebeck coefficient actually measured at T and $n_H(T)$ multiplied by a ratio of the two temperatures. A similar argument holds for the Hall mobility (Equation 3.24), which scales as T^{-p}, with the value of p depending on the scattering mechanism [31] and the temperature dependence of the effective mass. This technique is referred to as the scaled effective mass model, since it yields the effective mass and the mobility parameter as separate quantities.

$$S\left(n_H(T), T_{scale}\right) = S\left(n_H(T), T\right) \times \frac{T_{scale}}{T} \tag{3.23}$$

$$\mu_H\left(n_H(T), T_{scale}\right) = \mu_H\left(n_H(T), T\right) \times \left(\frac{T}{T_{scale}}\right)^p \tag{3.24}$$

The scaled effective mass model requires Hall data, and these are not always available to researchers. Furthermore, Hall data are not always published in studies of new materials, making it difficult for researchers to determine whether the work is worth expanding upon. The conductivity σ can be scaled in the same manner as μ_H (Equation 3.25).

$$\sigma\left(n_H(T), T_{scale}\right) = n_H(T)\, e\mu_H\left(n_H(T), T_{scale}\right) = n_H(T)\, e\mu_H\left(n_H(T), T\right) \times \left(\frac{T}{T_{scale}}\right)^p \tag{3.25}$$

After scaling the conductivity this way, the weighted mobility $\mu_0 \left(m^*/m_e\right)^{3/2}$ [24] is used as a free parameter to fit a theoretical curve to scaled Seebeck versus scaled conductivity data. This technique is referred to as the scaled weighted mobility model, since it produces an estimate of the weighted mobility rather than separate estimates of the effective mass and the mobility parameter. The lattice thermal conductivity κ_L can be obtained from the values of S, σ, and κ, and can be used with the weighted mobility to compute the quality factor, which determines the maximum achievable zT in the material and is explained in Section 3.4. The scaled weighted mobility model is shown to yield quality factors very close to those obtained through Hall measurements on $Cu_{2-x}Se$ and $Cu_{2-x}S$ in Section 6.3, and it is used in Section 5.4 to predict the maximum zT in $Ag_2Se_{1-x}Te_x$.

3.4 Quality Factor

The equations above can be combined to make predictions of zT versus Hall carrier concentration. While zT ultimately determines the efficiency of a thermoelectric material, it depends on the dimensionless Fermi level η, i.e., on the energy level of the charge carriers. It would be useful for thermoelectric materials research if there were a parameter indicative of thermoelectric performance that did not depend on η. This parameter is referred to as the quality factor [37]. The Seebeck coefficient, Hall carrier concentration, Hall mobility, and thermal conductivity all consist of a Fermi-level independent part multiplied by a function of Fermi integrals. Algebraic manipulation of Equations 3.15 through 3.22 into Equation 1.2 to separate the part that does not depend on η, as was done in [37] yields the dimensionless quality factor, given in Equation 3.26.

$$B = \frac{8\pi e}{3}\left(\frac{k_B}{e}\right)^2\left(\frac{2m_e k_B}{h^2}\right)^{3/2}\frac{\mu_0\left(m^*/m_e\right)^{3/2}T^{5/2}}{\kappa_L} \tag{3.26}$$

To understand the physical significance of the quality factor, we turn to a thermodynamic description of thermoelectric transport. By writing down the force-flux relations and deriving an equation for the rate of entropy transport $\vec{J}_S$ [38, 39], we obtain Equation 3.27. Note that both terms in the equation are negative and contain gradients of the electrical potential ϕ and the temperature T. This indicates that entropy is transported from high potential to low potential. We define the thermally-driven rate of entropy transport $\vec{J}_{ST}$ by Equation 3.28. Equation 3.28 shows that the term $1 + zT$ is related to entropy transport; this is related to the term $1 + ZT$ in the equation for thermoelectric efficiency, Equation 1.1.

$$\vec{J}_S = -\frac{S\sigma}{e}\nabla\left(e\phi\right) - \frac{\kappa + S^2\sigma T}{k_B T}\nabla\left(k_B T\right) \tag{3.27}$$

$$\vec{J}_{ST} = -\frac{\kappa + S^2\sigma T}{k_B T}\nabla\left(k_B T\right) = -\frac{\kappa}{kT}\left(1 + zT\right)\nabla\left(k_B T\right) \tag{3.28}$$

The thermal conductivity κ in zT is defined for zero electric current (Equation 3.29) and in the rest of this chapter is referred to as κ_J. It is made up of an electronic contribution κ_e and a lattice contribution κ_L. The thermal conductivity at zero electric field is given by Equation 3.30. $1 + zT$ is equal to κ_E/κ_J, and it is a ratio of the thermally-driven entropy transferred by electrical current to that transferred without electrical current.

$$\kappa_J = \kappa_e + \kappa_L \tag{3.29}$$

$$\kappa_E = \kappa_J + S^2\sigma T \tag{3.30}$$

By analogy with this physical significance of zT, the quality factor is also a ratio of thermal conductivities. It is a ratio of the characteristic thermally-driven entropy transport by electrical means to the characteristic entropy transport by mechanical means. To further solidify this interpretation, we look at the terms in Equation 3.26. Each term is a characteristic scale for one of the components of zT. The characteristic scales are defined in Equations 3.31 through Equation 3.33. Putting these scales together, B is given by Equation 3.34. In the form of Equation 3.34, B strongly resembles zT. We can think of B as a scale for zT, again as a ratio of the electrical thermal entropy transport to the mechanical thermal entropy transport. zT describes how much entropy is apportioned to each transport channel.

$$S_c = \frac{k_B}{e} \tag{3.31}$$

$$n_{Hc} = \frac{8\pi}{3}\left(\frac{2m^* k_B T}{h^2}\right)^{3/2} \tag{3.32}$$

$$\sigma_c = n_{Hc} e \mu_0 \tag{3.33}$$

$$B = \frac{S_c^2 \sigma_c T}{\kappa_L} \tag{3.34}$$

Practically, B sets the maximum achievable zT in a material. Figure 3.1 shows curves of zT versus Hall carrier concentration for different values of B and m^*.

B can be reduced to more fundamental components than those in Equation 3.26 by assuming that acoustic phonon scattering is the dominant charge carrier scattering mechanism [40]. In this case, B is given by Equation 3.35, C_{11} is a collection of elastic constants, and Ξ is the deformation potential [41].

$$B = \frac{8k_B^2\hbar}{9\pi^{3/2}} \frac{C_{11}}{m^* \Xi^2 \kappa_L} T \tag{3.35}$$

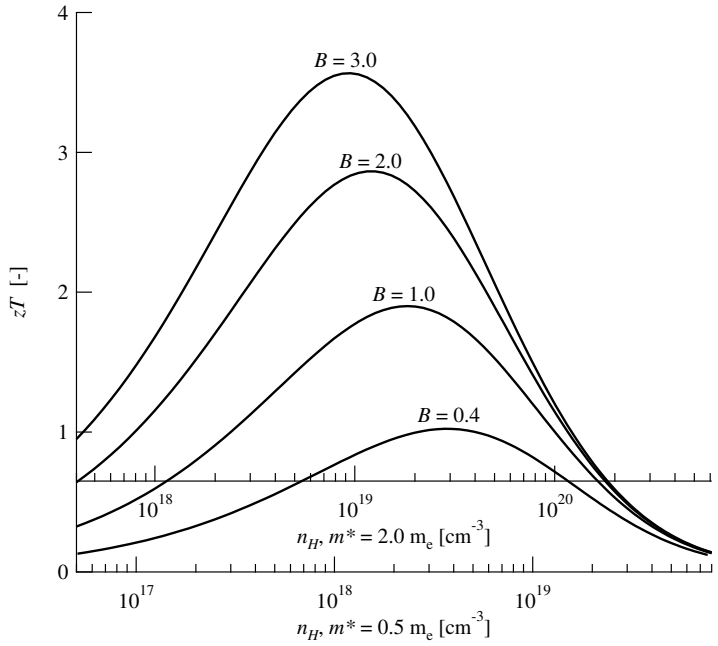

Figure 3.1: zT curves for different values of B. Note that changing the effective mass shifts the optimum Hall carrier concentration.

Chapter 4

Copper Selenide

4.1 Introduction

Copper selenide (Cu_2Se) is a p-type semiconductor with a band gap of 1.23 eV [42]. Despite this relatively large band gap, copper selenide has resistivity values of less than 1 mΩ cm because it exists with copper vacancies. Above 410 K [43], copper selenide transitions to a Cu^+ conducting phase, wherein the copper ions are mobile and described as 'liquid-like' because their diffusivity coefficient is about 10^{-5} cm^2 s^{-1}, comparable to the value for liquid water [16]. This results in lattice thermal conductivity values as low as 0.4 W m^{-1} K^{-1} and in turn a maximum zT of 1.5 at 1000 K [16], making it competitive with PbTe, the leading thermoelectric material in the hundreds of kelvin temperature range [11].

While copper selenide has been shown to have potential as a thermoelectric material at high temperature, its ionic conductivity has caused long-term stability problems for use in thermoelectric generators [44]. This spurred interest in the properties of copper selenide below the phase transition, where the ionic conductivity would not be of concern. In the first section of this chapter, we will look at the potential for copper selenide to achieve high zT values at room temperature and at an attempt to dope the material to optimize its properties. In the second section, we will turn back to the high-temperature properties and investigate the composition chosen by NASA to build radioisotope thermal generators that turned out to be problematic.

4.2 Potential for High zT at Room Temperature

We begin by looking at the transport properties of copper selenide, shown in Figure 4.1. The samples in Figure 4.1 were made by different methods and with different nominal concentrations of copper vacancies. In both methods, the initial heating step resulted in an ingot of copper selenide with a chunk of unreacted copper, which was then mixed with the ingot by different means. The samples labeled "MBM" were made by melting 3-4 mm shots of the elements, and then ball-milling the

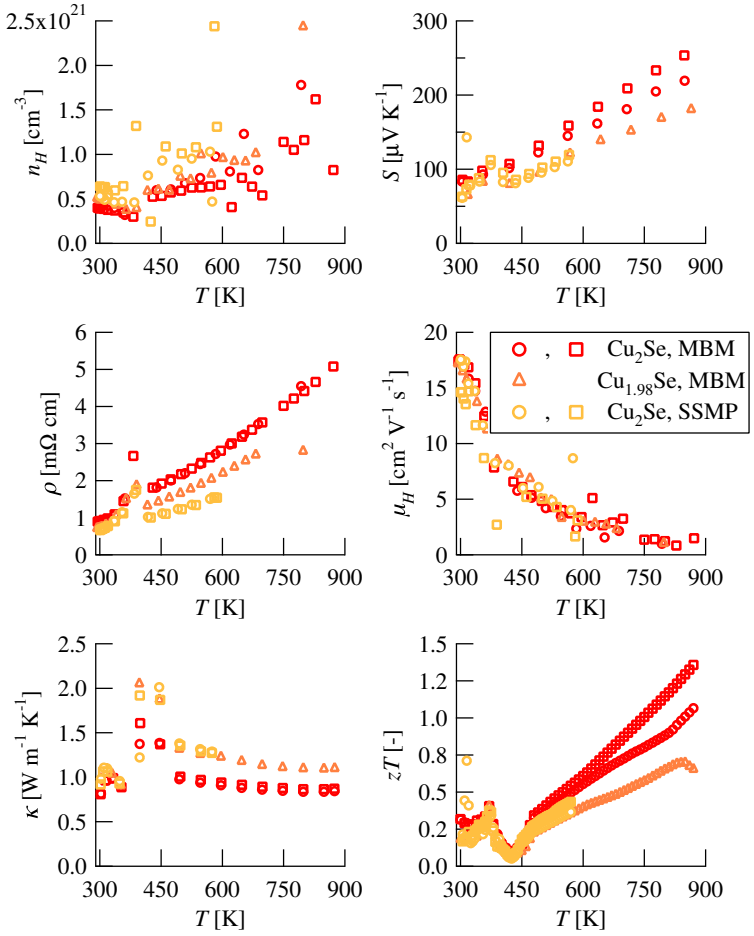

Figure 4.1: Transport properties of $Cu_{2-x}Se$ made by different methods. (a) The degree of non-stoichiometry x has a direct effect on the Hall carrier concentration n_H. Each Cu atom missing creates a positively charged hole. (b) As the carrier concentration decreases, the Seebeck coefficient S increases. Seebeck increases with temperature because the number of electronic states increases with temperature. (c) The resistivity is inversely proportional to the carrier concentration. (d) The Hall mobility decreases with temperature due to acoustic phonon scattering, as the temperature increases the more scattering sites are activated. (e) The thermal conductivity is changed by the carrier concentration through the electronic portion equal to LT/ρ. (f) Copper selenide reaches a zT of 1.2 at 900 K. It reaches much smaller values at room temperature, but these could be raised to 1.2 with proper doping (Figure 4.2).

resulting ingot, and then hot-pressing the resulting powder. The samples labeled "SSMP" were made by heating elemental powders below the melting point, and then grinding the resulting ingot in a mortar and pestle, and then hot-pressing the resulting powder. The samples with a nominal composition of Cu_2Se made by different methods exhibit different transport properties. It could be that high-energy ball-milling forced more copper into solution than did hand-grinding, or it could be that heating powdered Se resulted in more evaporation of that element than did melting solid chunks of it. The synthesis method affects the properties of the resulting samples. This variation in stoichiometry results in changes in Hall carrier concentration, which allows us to apply the SPB model to the material. The individual fits leading to estimates of the effective mass m^*, the mobility parameter μ_0, and the lattice thermal conductivity κ_L are shown in Figure 4.4, but for now we turn our attention to the resulting prediction of zT versus Hall carrier concentration, shown in Figure 4.2.

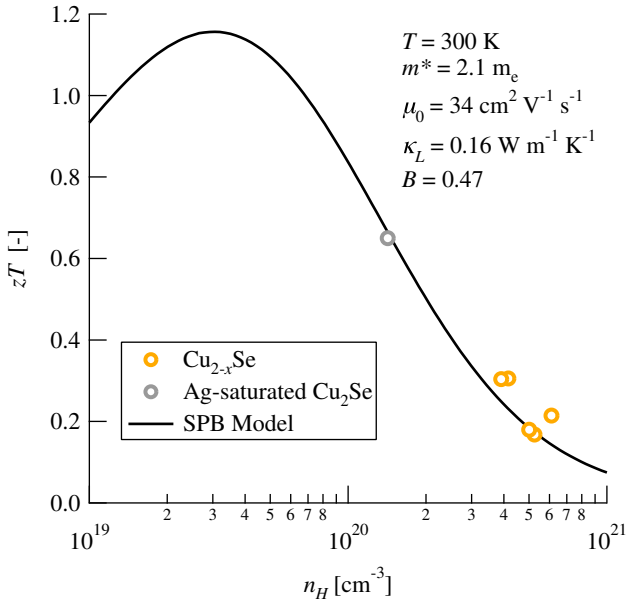

Figure 4.2: Prediction of zT versus Hall carrier concentration for Cu_2Se at 300 K. Orange symbols are $Cu_{2-x}Se$, the gray symbol represents Ag-saturated Cu_2Se as predicted from effective-medium theory and measurements of $Cu_{1.97}Ag_{0.03}Se$ (Chapter 7).

Cu_2Se is predicted to reach a maximum zT of 1.16 at 300 K. This value is greater than the state-of-the-art value of 0.9 achieved in bulk $Bi_{2-x}Sb_xTe_3$ materials at room temperature [45]. Copper selenide has a relatively low mobility parameter of 34 cm^2 V^{-1} s^{-1}, but this is offset by its low lattice thermal conductivity of 0.16 W m^{-1} K^{-1}, which is much lower than typical κ_L values of 1 W m^{-1} K^{-1} found in thermoelectric materials. However, the samples of Cu_2Se made so far have Hall carrier concentrations of 4-7$\times 10^{20}$ cm^{-3}, much greater than the optimum value of 3×10^{19} cm^{-3}. It is therefore necessary to dope the material to reduce its carrier concentration. Copper selenide

is a p-type material, so an n-type dopant is needed, i.e. one which will donate electrons to fill in the holes in copper selenide's valence band. Ag is known to reduce the carrier concentration of copper selenide this way (Section 4.3), but the electrical properties of Ag-saturated Cu_2Se extracted using the method in Chapter 7 yield a maximum zT of only 0.65, assuming the same effective mass and lattice thermal conductivity. A candidate dopant is Br substituted on the Se site to form $Cu_2Se_{1-x}Br_x$. Cu_2Se has been doped with I before, but this did not create an appreciable change in the room-temperature zT [46, 47].

The transport properties of $Cu_2Se_{1-x}Br_x$ are shown in Figure 4.3. Comparing the points with x equal to 0.00 with the other data, it is clear that substituting Br for Se has the desired effect. The Hall carrier concentration n_H decreases as x increases. The resistivity ρ and the Seebeck coefficient S both increase as x increases. The samples with x greater than zero all have markedly lower thermal conductivity than Cu_2Se. It was assumed that the samples have heat capacity equal to that measured on Cu_2Se [23]. However, the zT values at room temperature do not exceed 1, and those at high temperature are only slightly greater than the zT values of Cu_2Se. To understand why doping with Br did not result in high zT values, we look at the results of the SPB model, shown in Figure 4.4.

The top right curves of Figure 4.4 are predictions of how S will change with n_H in Cu_2Se. Orange symbols denote Cu_2Se and green symbols denote $Cu_2Se_{1-x}Br_x$. Each material was analyzed separately. The effective masses estimated for each material from the SPB model are within 2% of one another. It appears that Br does not change the curvature of the valence band of Cu_2Se. The values of κ_L for Cu_2Se and $Cu_2Se_{1-x}Br_x$ are also roughly the same, being 0.16 and 0.20 W m^{-1} K^{-1}, respectively.

The most striking difference between the two materials is the mobility parameter. Copper selenide has a mobility parameter of 34 cm^2 V^{-1} s^{-1}, but $Cu_2Se_{1-x}Br_x$ has a mobility parameter of 17 cm^2 V^{-1} s^{-1}. It appears that adding Br drastically reduces the mobility of the material. A similar effect was documented in n-type PbSe doped with metal cations whose states fell in the conduction band, affecting that band's mobility [48]. In a material influenced by a single parabolic band and with acoustic phonons as the main scatterers of electrons, the Hall mobility should decrease with Hall carrier concentration. The Hall mobility data for $Cu_2Se_{1-x}Br_x$ in Figure 4.4 exhibit a slight upward trend with Hall carrier concentration. We need to incorporate another scattering mechanism to understand this contradiction of our assumptions.

The scattering mechanism is represented by the relaxation time τ, defined for a single scattering mechanism by Equation 3.5. When one scattering mechanism does not dominate scattering in the material, multiple scattering rates must be taken into account. Each scattering rate is equal to $1/\tau_i$, where τ_i is the relaxation time for a particular scattering mechanism. The scattering rates are treated like resistors in series, so the total scattering rate $1/\tau$ is equal to the sum of the individual

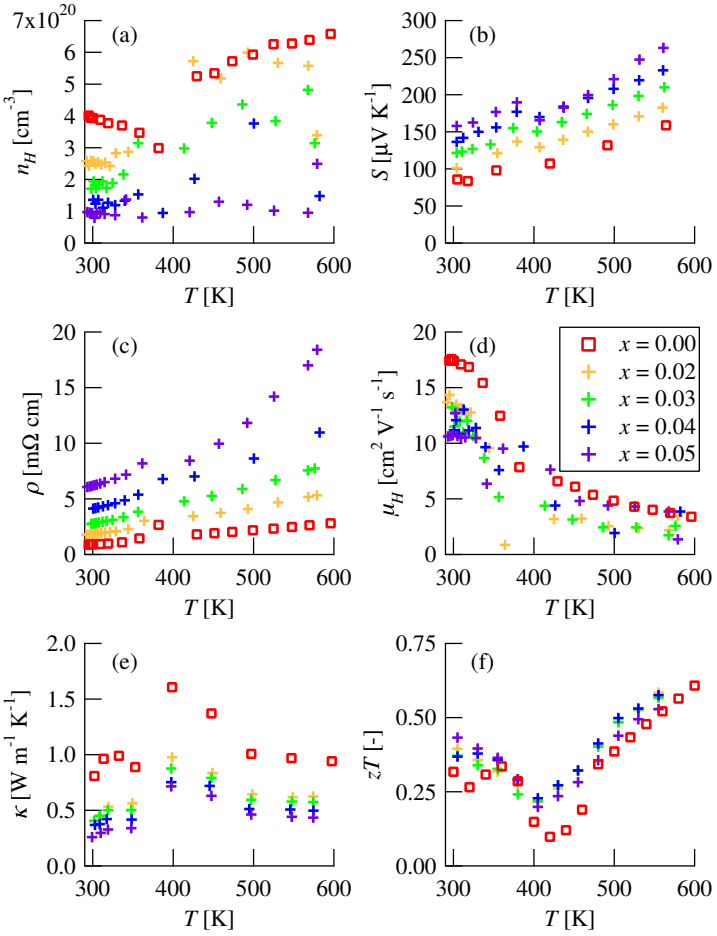

Figure 4.3: Red squares denote a nominal composition of Cu_2Se; other samples have the composition $Cu_2Se_{1-x}Br_x$. (a) Br works as a dopant in Cu_2Se, as indicated by the decreasing Hall carrier concentration as the Br content increases. (b) The Seebeck coefficient also increases as the Br content increases. (c) The resistivity shows an increasing trend with temperature, as expected for acoustic phonon scattering. (d) The Hall mobility for Br content x greater than zero should be greater than that of Cu_2Se; however, the Br-doped samples show depressed Hall mobility. (e) The thermal conductivity of the Br-doped samples is less due to a decreased electronic thermal conductivity. (f) zT of the Br-doped samples is greater than that of Cu_2Se, but does not reach the values predicted in Figure 4.2.

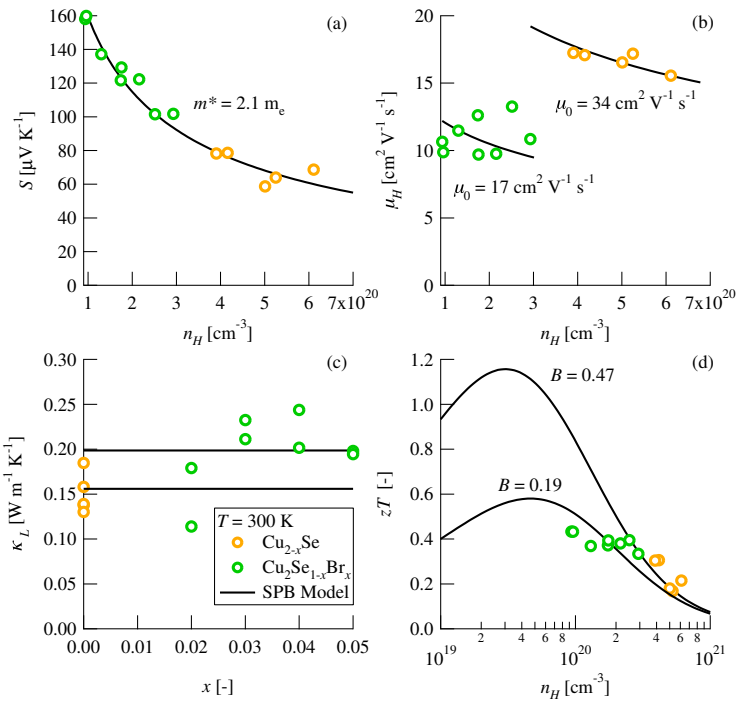

Figure 4.4: SPB results for Cu_2Se and $Cu_2Se_{1-x}Br_x$ at 300 K. (a) The Seebeck versus Hall carrier concentration data fit well to a single effective mass curve. (b) The Br-doped samples exhibit a dramatically reduced mobility paramater. (c) The Br-doped samples also have a slightly greater lattice thermal conductivity. Straight lines in the κ_L plot represent average κ_L values for each material. (d) Br doping results in greater zT; however, the zT versus Hall carrier concentration curve falls under that predicted for Cu_2Se due to the reduced mobility parameter.

scattering rates $1/\tau_i$.

The relaxation time for acoustic phonon scattering is given by Equation 4.1 [1]. Ξ is the deformation potential [41], and ϵ is the dimensionless charge carrier energy.

$$\tau_{ac} = \frac{\pi\hbar^4 v_l^2 d}{\sqrt{2}\Xi^2 \left(m^* k_B T\right)^{3/2}} \epsilon^{-1/2} \tag{4.1}$$

Since two kinds of atoms are occupying the Se site (Se and Br), it is logical to include an alloy scattering mechanism. The relaxation time for alloy scattering [49] is given in Equation 4.2. V_{atom} is equal to M/nNd, where M is the molecular weight, n is the number of atoms per formula unit, N is Avogadro's constant, and d is the density. U is the alloy scattering potential, which is similar to the deformation potential Ξ in that it describes the way the scattering mechanism changes the energy states of the charge carriers. x is the fraction of substituted atoms.

$$\tau_{alloy} = \frac{8\hbar^4}{3\sqrt{2}\pi V_{atom} x\left(1-x\right) U^2 m^{*3/2} \left(k_B T\right)^{1/2}} \epsilon^{-1/2} \tag{4.2}$$

As stated above, the total relaxation time τ is related to the total scattering rate $1/\tau$, given below.

The scattering mechanism determines the parameter λ in Equation 3.5, which in turn determines the order of the Fermi integrals used to calculate the transport properties. Since τ_{ac} and τ_{alloy} have the same dependence on ϵ, including alloy scattering does not change the order of the Fermi integrals, and μ_0 can be modeled separately. τ can be used with the effective mass m^* to calculate μ_0 with Equation 3.19.

$$\tau^{-1} = \tau_{ac}^{-1} + \tau_{alloy}^{-1} \tag{4.3}$$

Applying the combined acoustic phonon/alloy scattering model to values of μ_0 computed for each value of x with the deformation potential Ξ and the alloy scattering potential U as free parameters, we obtain a deformation potential of 5.8 eV and an alloy scattering potential of 1.1 eV. The deformation potential obtained for $Cu_2Se_{1-x}Br_x$ is equal to that obtained for Cu_2Se. The Hall mobility versus Hall carrier concentration curve accounting for acoustic phonon and alloy scattering is shown in Figure 4.5. The reduction of μ_0 in the Br-doped samples due to alloy scattering reduces the quality factor of Cu_2Se from 0.47 to 0.19. While Br acts as a dopant, i.e. it reduces the Hall carrier concentration and increases the Seebeck coefficient, the additional scattering from the dissimilar atoms on the anion site reduces the maximum possible zT to 0.6.

Table 4.1: Densities and speeds of sound of $Cu_2Se_{1-x}Br_x$ at 300 K

x	Density [kg m^{-3}]	v_l [m s^{-1}]	v_s [m s^{-1}]
0	6618	3250	1860
0.02	6530	3250	1270
0.03	6542	2700	1350
0.04	6444	2900	1270
0.05	6336	2640	1270

One might think that ionized impurity scattering would play a role in $Cu_2Se_{1-x}Br_x$ because of the deliberate introduction of bromide ions. An upward trend of μ_H with n_H can indicate ionized impurity scattering due to screening of the impurities by the charge carriers. A combined acoustic phonon and ionized impurity scattering model was applied to the data at 300 K using the equation for the ionized impurity scattering relaxation time [32] and 11.6 for the relative permittivity of $Cu_2Se_{1-x}Br_x$ [50]. The S versus n_H data along with curves resulting from combining acoustic phonon scattering with ionized impurity and alloy scattering are shown in Figure 4.6. Ionized impurity scattering is known to increase the Seebeck coefficient relative to that for acoustic phonon scattering [51, 52]. At the lowest values of n_H measured in $Cu_2Se_{1-x}Br_x$, where ionized impurity scattering would have the greatest effect, the Seebeck curve generated by the combined acoustic phonon/ionized impurity scattering model predicts Seebeck coefficients up to 25% greater than those actually observed. This systematic over-prediction of the Seebeck coefficient rules out the presence of ionized impurity scattering in this material. This is encouraging because it suggests

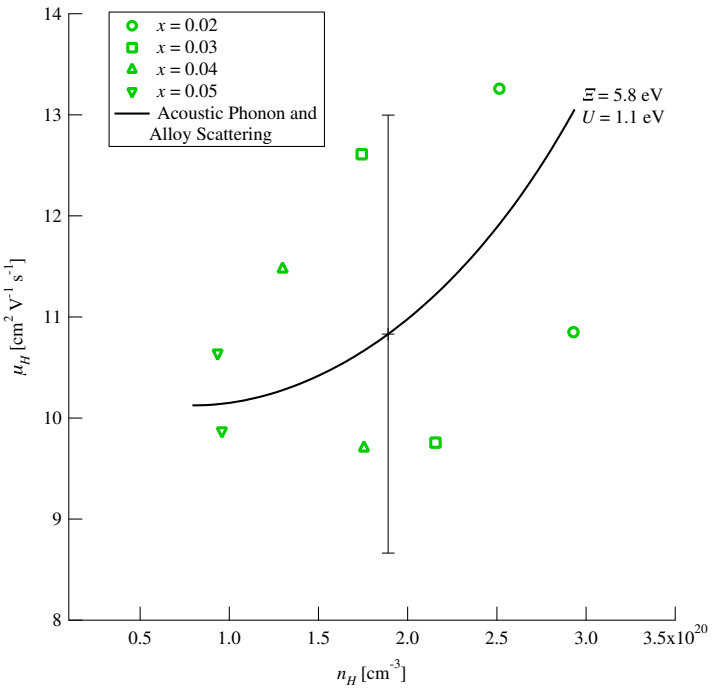

Figure 4.5: Model for Hall mobility including acoustic phonon and alloy scattering. The error bars represent a change in Ξ and U of 10%.

that doping with something other than Br may not affect the mobility parameter, whereas ionized impurity scattering implies that any dopant would reduce μ_0 and therefore reduce the maximum potential zT.

The SPB model was also applied to $Cu_2Se_{1-x}Br_x$ transport data at 550 K. The results are shown in Figure 4.7. The effective masses of Cu_2Se and of the Br-doped samples are increased relative to the values at 300 K. This increase in effective mass is responsible for the reduction in μ_0 in both types of samples relative to the values at 300 K; μ_0 depends on $m^{*-5/2}$. The trend of the Hall mobility rising with carrier concentration in the Br-doped samples at 300 K is gone at 550 K. At the higher temperature, the Hall mobility decreases with Hall carrier concentration, as expected for acoustic phonon scattering. This is because the relaxation time for acoustic phonon scattering (Equation 4.1) depends on $T^{-3/2}$, whereas that for alloy scattering depends on $T^{-1/2}$, so at higher temperatures the acoustic phonon relaxation time will be much shorter and will dominate the total scattering rate. The lower lattice thermal conductivity of the Br-doped samples (0.4 W m^{-1} K^{-1} versus 0.6 W m^{-1} K^{-1}) gives them a slight edge over Cu_2Se in maximum zT at 550 K, as shown by the predicted zT versus Hall carrier concentration curves in the bottom right plot of Figure 4.7.

The SPB results for $Cu_2Se_{1-x}Br_x$ at all temperatures at which the SPB model was applied are shown in Table 4.2.

While the failure of Br-doping to raise the room temperature zT of Cu_2Se to a competitive value

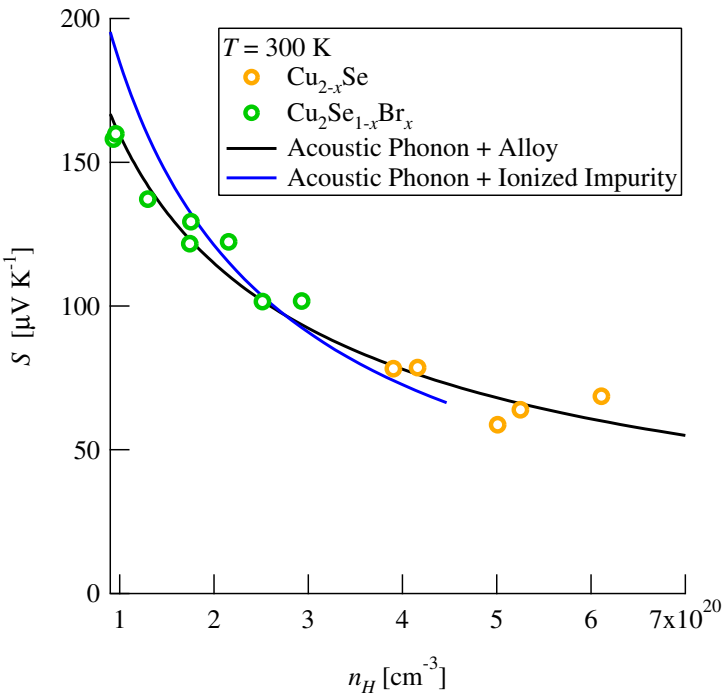

Figure 4.6: Overestimation of the Seebeck coefficient at low n_H rules out ionized impurity scattering.

Table 4.2: SPB results for $Cu_2Se_{1-x}Br_x$

	$m^*[m_e]$		μ_0[cm^2 V^{-1} s^{-1}]		κ_L [W m^{-1} K^{-1}]	
T [K]	Cu_2Se	$Cu_2Se_{1-x}Br_x$	Cu_2Se	$Cu_2Se_{1-x}Br_x$	Cu_2Se	$Cu_2Se_{1-x}Br_x$
300	2.1	2.1	34	17	0.16	0.20
350	2.3	2.4	23	12	0.31	0.30
400	3.0	2.5	12	9.1	1.3	0.68
450	2.7	3.2	11	5.5	1.0	0.58
500	3.1	3.8	8.1	3.9	0.61	0.42
550	3.5	4.3	6.1	3.3	0.60	0.41

is disappointing, it is encouraging for two reasons. First, the result shows that it is possible to reduce the hole concentration in copper selenide. Second, this result could be useful for band engineering in other materials. For example, n-type Ag_2Se, discussed in Chapter 5, has a minority carrier contribution at 300 K, where the material is predicted to have a zT of 1.2 if the carrier concentration can be reduced. Reducing the carrier concentration will strengthen the hole contribution from the valence band, reducing zT. Doping with Br to reduce the hole conductivity and counter-doping with Ag vacancies to maintain the carrier concentration could be a solution to bipolar conduction in Ag_2Se.

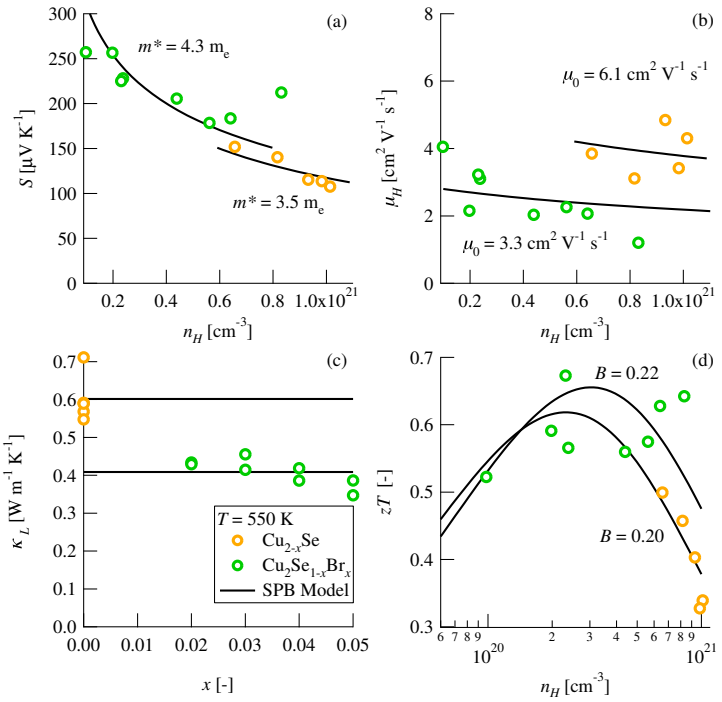

Figure 4.7: SPB results for Cu_2Se and $Cu_2Se_{1-x}Br_x$ at 550 K. (a) The presence of Br increases the effective mass of copper selenide. (b) The mobility parameter is drastically decreased at 550 K as it is at 300 K, but this is due to the increased effective mass because alloy scattering plays a much smaller role at higher temperature. (c) Doping with Br reduces the lattice thermal conductivity. Straight lines in the κ_L plot represent average κ_L values for each material. (d) The reduced lattice thermal conductivity results in slightly greater zT values for the Br-doped samples.

4.3 Ag-Doping of Cu_2Se at High Temperature

This section is an adapted reproduction, with permission, from *Materials for Renewable and Sustainable Energy*, v. 3, no. 2, (2014). Copyright 2014, Springer Science+Business Media.

A compound related to Cu_2Se is $Cu_{1.97}Ag_{0.03}Se_{1+y}$ [53], which was studied from the late 1960s through the late 1970s as a candidate for use in radioisotope thermal generators (RTGs) [44]. The compound with y equal to 0 ($Cu_{1.97}Ag_{0.03}Se$), synthesized by 3M, reached a zT of 1.1 at 870 K [44], which is comparable to the zT of 1.0 at 870 K achieved in $Cu_{1.97}Ag_{0.03}Se$ in this work. $Cu_{1.97}Ag_{0.03}Se_{1+y}$ was tested under RTG conditions (hot side between 1000 K and 1200 K, cold side between 400 K and 600 K) and exhibited a host of problems. The main problem was that copper ions would diffuse to the cold side, causing Se to evaporate from the hot side, leading to disintegration of the thermoelectric legs. This disintegration was due to the very effect that makes copper chalcogenides so attractive in the first place, the mobile copper ions that result in low lattice thermal conductivity [44]. This important engineering problem is beyond the scope of this thesis; we now turn to a single parabolic band analysis of $Cu_{1.97}Ag_{0.03}Se_{1+y}$. Recently, the "overstoichiometric"

composition $Cu_{1.98}Ag_{0.2}Se$ was studied and found to reach a maximum zT of 0.52 at 650 K before the onset of bipolar conduction [54]. Therefore we seek to analyze these materials together with $Cu_{2-x}Se$ to determine the suitability of a single model for describing them and explore whether they can achieve greater zT values.

Powder XRD (PXRD) shows that $Cu_{1.97}Ag_{0.03}Se_{1+y}$ is not single-phase (Figure 2.3); rather it is composed of $Cu_{2-x}Ag_xSe$, CuAgSe [55] and at least one more unidentified impurity phase, i.e., some of the Ag enters the Cu_2Se matrix and some forms CuAgSe (which has also been evaluated as a thermoelectric material and found to have low zT values) [56]. In $Cu_{1.97}Ag_{0.03}Se$ the CuAgSe phase is observed to dissolve at about 380 K, slightly before the superionic phase transition just above 400 K. At 420 K all peaks can be indexed and refined in the high temperature Cu_2Se structure (antifluorite, space group $Fm\bar{3}m$) except for a few, low intensity peaks from one or more unidentified impurities. The main phase peaks are satisfactorily described by the antifluorite structure when Cu interstitials are incorporated on the octahedral sites and at trigonal planar sites. The atomic positions were stable when refined. The room temperature Cu_2Se structure is not known but comparison to phase-pure Cu_2Se PXRD patterns [43] reveals another set of peaks not belonging to the impurity at high temperatures, CuAgSe, or pure Cu_2Se. These peaks disappear at the phase transition and can hence either be an impurity, which dissolves, or belong to the main phase if this has a slightly different structure than pure Cu_2Se.

In this study, the compositions Cu_2Se, $Cu_{1.98}Se$, $Cu_{1.97}Ag_{0.03}Se$, and $Cu_{1.97}Ag_{0.03}Se_{1.009}$ were synthesized and data on $Cu_{1.98}Ag_{0.2}Se$ from a recent publication by Ballikaya et al [54] are included for a more complete analysis.

The thermoelectric properties of a material depend strongly on the Hall carrier concentration, n_H, whose magnitude can vary with temperature and via chemical doping. In the aforementioned materials, n_H can be decreased by substituting Ag for Cu, or increased by adding Se to create Cu^+ vacancies. Each additional Se^{2-} ion is equivalent to 2 Cu^+ vacancies; each Cu^+ vacancy donates one hole to the valence band. Furthermore, previous work on the band gap of Cu_2Se [42] shows that the valence and conduction bands are separated by a band gap much greater than k_BT, so that only one type of carrier is present. The Hall carrier concentration for all samples is shown in Figure 4.8(a). Above the phase transition, the Hall carrier concentration of $Cu_{1.97}Ag_{0.03}Se_{1.009}$ is greater than that of $Cu_{1.97}Ag_{0.03}Se$ due to the greater deficiency of metal ions. Likewise, the Hall carrier concentration of $Cu_{1.98}Se$ is greater than that of Cu_2Se. This could be because substitution of Ag for Cu alters the native vacancy concentration of Cu_2Se. The Hall carrier concentration of $Cu_{1.98}Ag_{0.2}Se$ is at least an order of magnitude less ($\sim 10^{19}$ cm^{-3}) than the other compositions ($\sim 10^{20}$-10^{21} cm^{-3}) due to the excess of metal ions [54]. Between 750 K and 800 K, the Hall carrier concentrations of $Cu_{2-x}Se$ and $Cu_{1.97}Ag_{0.03}Se_{1+y}$ dramatically increase. The exponential character of this increase seems to indicate bipolar conduction. However, the concomitant decreases in Seebeck and resistivity are not

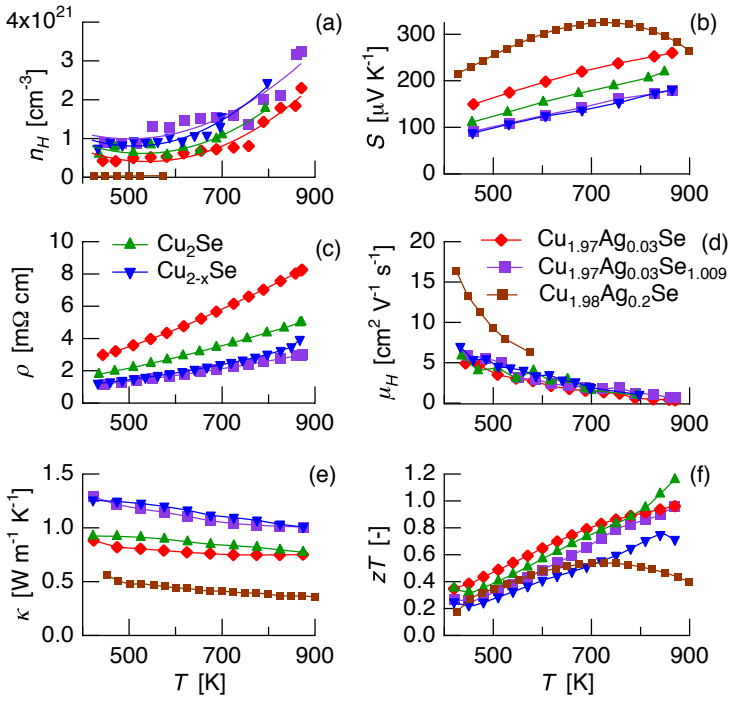

Figure 4.8: Transport properties as functions of temperature of $Cu_{2-x}Se$, $Cu_{1.97}Ag_{0.03}Se_{1+y}$ and literature data on $Cu_{1.98}Ag_{0.2}Se$ from Ballikaya et al [54]. Hall carrier concentration n_H, Seebeck coefficient S, resistivity ρ, Hall mobility μ_H, total thermal conductivity κ, and figure-of-merit zT are shown in Figures (a), (b), (c), (d), (e), and (f), respectively. The resistivity of $Cu_{1.98}Ag_{0.2}Se$ is not shown because it is several times greater than that of the other compositions. Above the phase transition and up to 780 K, $Cu_{1.97}Ag_{0.03}Se$ achieves higher zT values (Figure 4.8(f)) than do Cu_2Se and $Cu_{1.98}Se$ because its Hall carrier concentration is closer to the optimum value (Figure 4.9). $Cu_{1.98}Ag_{0.2}Se$ is under-doped compared to both compositions of $Cu_{1.97}Ag_{0.03}Se_{1+y}$, as indicated by its greater Seebeck coefficient (Figure 4.8(a)) and lower zT values at all temperatures.

observed. While Hall carrier concentration data for $Cu_{1.98}Ag_{0.2}Se$ were not available above 575 K in Ballikaya et al [54], the influence of a conduction band separated from the valence band by a band gap of order k_BT is corroborated by the decrease in the Seebeck coefficient of that composition at 725 K, shown in Figure 4.8(b).

$Cu_{2-x}Se$ and $Cu_{1.97}Ag_{0.03}Se_{1+y}$ exhibit the steady increase with temperature of the Seebeck coefficient (Figure 4.8(b)) and of the resistivity ρ (Figure 4.8(c)) expected of a single-carrier semiconductor. $Cu_{1.98}Ag_{0.2}Se$ has greater values of S and ρ than do the other samples in the entire temperature range due to its much lower Hall carrier concentration, and it shows a peak in S at about 725 K.

The Hall mobilities, μ_H, of $Cu_{2-x}Se$, $Cu_{1.97}Ag_{0.03}Se_{1+y}$ and $Cu_{1.98}Ag_{0.2}Se$ above the phase transition are low compared to those of other high-performance p-type thermoelectric materials, such as 6-40 $cm^2\ V^{-1}\ s^{-1}$ in Na-doped PbTe between 600 K and 750 K, depending on carrier concentration [57]. The Hall mobility scales with T^{-p} [31]. The average value of p taken from the

data shown in Figure 4.8(d) and above the phase transition is about 3.1. Values of p between 1 and 1.5 usually indicate that acoustic phonons limit electron mobility in the material [31], while values greater than 1.5 indicate a temperature-dependent effective mass [58].

The thermal conductivity data are shown in Figure 4.8(e). The sudden increase in κ around the phase transition temperature is due to the sharp peak in C_p [43]. $Cu_{1.98}Ag_{0.2}Se$ has the lowest thermal conductivity values because it has the lowest lattice thermal conductivity, presumably due to disorder caused by the greater amount of Ag, and because it has the lowest carrier concentration of the compositions studied, and therefore the lowest electronic thermal conductivity.

The zT data are shown in Figure 4.8(f). The zT values of $Cu_{2-x}Se$ and $Cu_{1.97}Ag_{0.03}Se_{1+y}$ all increase continuously from the phase transition temperature to the maximum temperature at which they were measured. The $Cu_{1.97}Ag_{0.03}Se$ sample reaches a zT of 1.0 at 870 K. Cu_2Se reaches a zT of 1.16 at 870 K, but between 450 K and 780 K has an average zT of 0.59, whereas $Cu_{1.97}Ag_{0.03}Se$ has an average zT of 0.66 in the same temperature range. Above 780 K, the increasing values of ρ in $Cu_{1.97}Ag_{0.03}Se$ and the decreasing values of κ in Cu_2Se mean that Cu_2Se has a greater zT. $Cu_{1.98}Ag_{0.2}Se$ reaches a peak zT of 0.52 at 650 K, then decreases due to bipolar conduction.

To understand why $Cu_{1.97}Ag_{0.03}Se$ achieves a greater zT up to 780 K than do the other samples, we analyze n_H and the effective mass m^*. The carrier mobility in this model is limited by acoustic phonon scattering and the effective mass is treated as a constant at each temperature. The results of our analysis are shown in Figure 4.9 and Table 4.3.

We estimated the effective mass m^* at 575 K (the highest temperature for which R_H data were available for $Cu_{1.98}Ag_{0.2}Se$) and 750 K (the lowest temperature at which none of the samples exhibit a sharp increase in Hall carrier concentration) by using m^* as a fitting parameter to fit a theoretical curve to S versus n_H data (Figure 4.9(a)). The effective mass increases with temperature (Table 4.3), which we predicted based on the Hall mobility data. The same trends of effective mass, Hall carrier concentration, resistivity, and Seebeck coefficient with temperature were observed by Voskanyan, et al [59], though they estimated different values of the effective mass, e.g. 2.2 m_e at 750 K as opposed to 6.2 m_e at 750 K, because they used assumed values of n_H instead of calculating them from R_H. Voskanyan, et al proposed a second valence band as a possible cause of the increasing effective mass. While this may explain of the trend of m^* with T, a two-band model is much more complex than a single band model, requires more assumptions, and does not guarantee a unique solution. Here we use a single band in this analysis in order to estimate the maximum achievable zT and optimum Hall carrier concentration in this material. We must emphasize that because the effective mass is not constant with temperature, our predictions are valid only at fixed temperatures as a function of Hall carrier concentration.

The estimated values of μ_0 (Table 4.3) fit to the data shown in Figure 4.9(b) decrease with temperature, as expected from the raw Hall mobility measurements. $Cu_{1.97}Ag_{0.03}Se_{1.009}$ has a

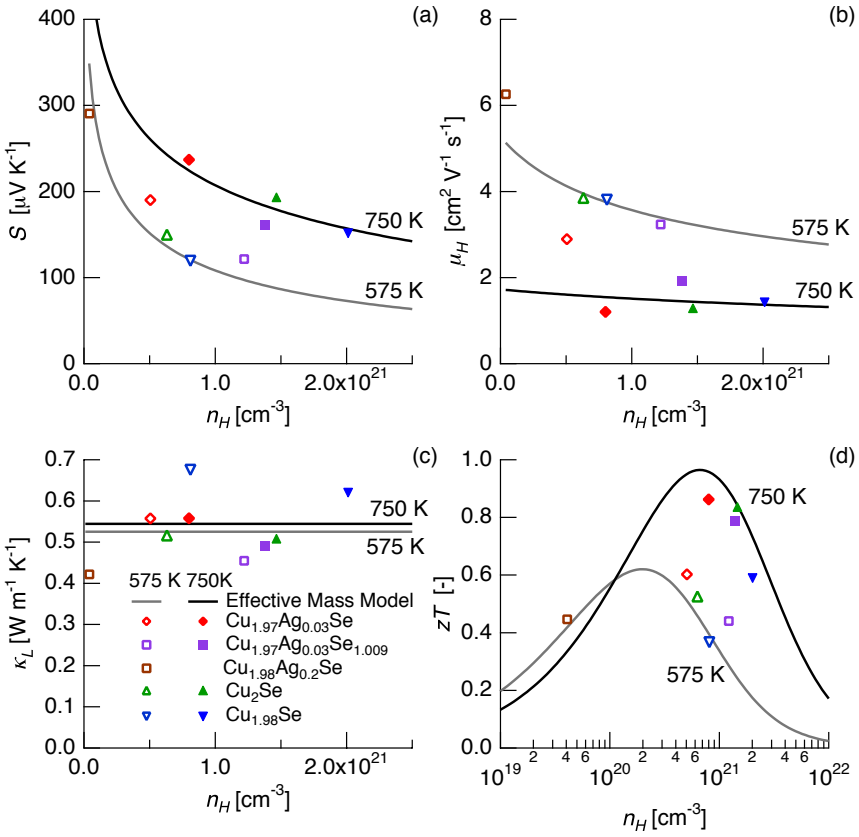

Figure 4.9: Analysis of effective mass and Hall carrier concentration explains and predicts the optimization of $Cu_{1.97}Ag_{0.03}Se$ for thermoelectric use. Figure 4.9(a) shows the Seebeck coefficient as a function of Hall carrier concentration with the effective mass as a fitting parameter. Figure 4.9(b) shows the Hall mobility as a function of Hall carrier concentration with μ_0 as a fitting parameter. The lattice thermal conductivity (Figure 4.9(c)) was computed from the resistivity and the Lorenz number L. The optimum Hall carrier concentration (Figure 4.9(d)) increases with temperature. The Hall carrier concentration of $Cu_{1.97}Ag_{0.03}Se$ also increases with temperature, so it has a Hall carrier concentration close to the optimum value up to 750 K. The lines in Figure 4.9(c) are average values of κ_L at the indicated temperature.

greater Hall mobility than does $Cu_{1.97}Ag_{0.03}Se$, despite having a greater carrier concentration and more defects.

The thermal conductivity is made up of a lattice contribution κ_L and an electronic contribution κ_e. κ_e is equal to LT/ρ, where L is the Lorenz number, given by Equation 3.21. The Lorenz numbers of the samples are between 1.5×10^{-8} and 1.9×10^{-8} V^2 K^{-2} at 575 K and 750 K.

κ_L of each composition is shown in Figure 4.9(c), along with the average κ_L at each temperature, the values of which are shown in Table 4.3. κ_L does not change significantly from 575 K to 750 K; therefore the optimization of zT in this materials system will hinge only on the electrical transport properties. The slight increase in κ_L with temperature in Table 4.3 is due to uncertainty in the calculated κ_e. Taking the estimates for m^*, μ_0, and κ_L, we can calculate a zT versus Hall carrier

concentration curve to determine the maximum zT at a given temperature and the optimum Hall carrier concentration (Figure 4.9(d)). Looking at the zT versus Hall carrier concentration curve for 575 K, it is clear that $Cu_{1.98}Ag_{0.2}Se$ is under-doped, leading to a decrease in zT above 650 K due to bipolar conduction. $Cu_{1.97}Ag_{0.03}Se$ has the Hall carrier concentration closest to the optimum value at every temperature at which we calculated an effective mass, which explains why that composition has the greatest zT of all the compositions included in the analysis.

According to our model, a maximum zT of just under 1.0 at 750 K is possible in this material system. The dimensionless quality factor B [37, 60, 40] is a measure of the maximum zT at a given temperature and depends only on material properties and temperature. The quality factors calculated for this material system increase with temperature (Table 4.3), meaning the theoretical maximum zT also increases with temperature. The quality factor of 0.36 achieved at 750 K means a maximum zT just below 1.0 is possible at that temperature; a quality factor of 0.40 is needed for a maximum zT of 1.0. Note that these quality factors are different from those originally published in [23]. This is because B will change depending on whether μ_0 is derived from μ_H or μ (see Section 3.2). All μ_0 values in this work are derived from μ_H, but the B values in this work have been adjusted to be consistent with those using μ_0 values derived from μ.

According to Figure 4.9(d), the optimum Hall carrier concentration $n_{H,opt}$ increases with temperature as well, which combined with the increasing trend with temperature of n_H in $Cu_{1.97}Ag_{0.03}Se$ means that that composition has a Hall carrier concentration close to $n_{H,opt}$ at and below 750 K.

Table 4.3: SPB results for $Cu_{1.97}Ag_{0.03}Se_{1+y}$

	575 K	750 K
$m^*[m_e]$	3.1	6.2
μ_0 [cm^2 V^{-1} s^{-1}]	5.9	1.9
κ_L [W m^{-1} K^{-1}]	0.53	0.54
$B[-]$	0.21	0.36

Our transport property measurements show that below 780 K $Cu_{1.97}Ag_{0.03}Se_{1+y}$ has superior zT values compared to $Cu_{2-x}Se$ because it has a Hall carrier concentration closer to the optimum value. We have analyzed the Hall carrier concentration and effective mass in these materials and in recently published data on $Cu_{1.98}Ag_{0.2}Se$ for a more complete analysis, and found that these materials together follow the trends expected despite the complexity of the atomic structure and presumed complexity of the electronic structure. This model predicts that a maximum zT of nearly 1.0 at 750 K is possible in this material system.

Each zT versus Hall carrier concentration curve in Figure 4.9 indicates that zT of Cu_2Se can be increased simply by reducing the Hall carrier concentration. This means that, if Cu_2Se is to be a commercially viable thermoelectric material, the addition of expensive Ag may be unnecessary. Any means of removing charge carriers from the material could improve its thermoelectric properties

above the phase transition. Such means could include anion substitution [22, 61, 62], for example doping with Br as described in Section 4.2 or doping with divalent cations [56]. Furthermore, our analysis is based only on electronic parameters, so separate optimization of the lattice thermal conductivity may improve the zT of this material even further.

4.4 Conclusions

We have seen the results of doping Cu_2Se with Cu vacancies, Ag, and Br. Doping with Br reduces the carrier concentration, but ultimately degrades the thermoelectric performance by the introduction of alloy scattering below the superionic transition and by increasing the effective mass at high temperature. Doping with vacancies or with Ag seems not to change the quality factor of Cu_2Se. It is therefore useful to look at the results of doping Cu_2Se with vacancies and with Ag together to see if the combined results (Table 4.4) follow any trends. The mobility parameter μ_0 decreases as temperature increases, as expected from Equation 4.1.

Table 4.4: SPB results for Cu_2Se

T [K]	$m^*[m_e]$	μ_0[cm^2 V^{-1} s^{-1}]	κ_L [W m^{-1} K^{-1}]
300	2.1	34	0.16
350	2.3	23	0.31
400	3.0	12	1.3
450	2.7	11	1.0
500	3.1	8.1	0.61
550	3.5	6.1	0.60
575	3.1	5.9	0.53
750	6.2	1.9	0.54

The effective mass m^* shows an overall upward trend with temperature. One way of explaining this is the influence of a second valence band. Bands within $2k_BT$ of the Fermi level will contribute to conduction, so it may be that a heavier band contributes to conduction as k_BT increases.

The trend of the lattice thermal conductivity κ_L is more complicated. κ_L increases from 0.16 W m^{-1} K^{-1} at 305 K to a maximum of 1.3 W m^{-1} K^{-1} at 400 K, then decreases as the temperature rises. The initial increase in κ_L can be understood through the superionic phase transition, which is also a structural phase transition. The spike in C_P across the phase transition increases the thermal conductivity [43]. As the material passes through 410 K and begins to conduct Cu^+, the thermal conductivity decreases due to the liquid-like conduction of metal ions.

Chapter 5

Silver Selenide

5.1 Introduction

The n-type chalcogenide $Ag_{2+x}Se$ has promising thermoelectric properties, but only a handful of studies have been conducted on it. Previous investigations on $Ag_{2+x}Se$ report that it has high electrical conductivity and low thermal conductivity and that its zT approaches 1 at room temperature [19, 20]. Lower zT values have been reported in mechanically-alloyed silver selenide [63]. The reported zT increases as temperature increases from 70 K to room temperature [20]. This is especially encouraging because $Ag_{2+x}Se$ becomes a superionic conductor around 407 K [26], as does Cu_2Se, which has been reported to have a zT that increases with temperature to 1.5 at 1000 K [16]. Cu_2Se has a low lattice thermal conductivity because the mobile Cu ions scatter phonons, an effect also seen in Ag ion-conducting $AgCrSe_2$ [18]. Considering the previously reported zT behavior and the mobile Ag ions, $Ag_{2+x}Se$ could have high zT in the superionic phase. The authors of the previous work on $Ag_{2+x}Se$ made no attempt to optimize its thermoelectric properties, suggesting that the already good thermoelectric performance of this material could be made even better. An additional feature of $Ag_{2+x}Se$ is the abundance of its elements in the Earth's crust compared to Bi_2Te_3, a thermoelectric in wide use for cooling applications [64].

While $Ag_{2+x}Se$ appears to be a good thermoelectric material, there is some discrepancy in the reported room temperature zT values. The reported zT at room temperature varies from 0.32 to 0.96 [19, 20]. Furthermore, these reports contain no measurements of the thermoelectric properties above room temperature. It seems possible that $Ag_{2+x}Se$ could be a useful thermoelectric material. However, in order to confirm this we must know how to control zT and the value of the maximum possible zT.

We will first look at the transport properties of $Ag_{2+x}Se$ and show that it is over-doped. We

will then propose some means of mitigating the effects of silver selenide's valence band on its thermoelectric performance. Last, we examine some results of doping with Te to reduce the carrier concentration.

5.2 $Ag_{2+x}Se$

In this work we measure the properties of $Ag_{2+x}Se$ from 300 K to 673 K and propose a model relating the maximum zT at room temperature and above to the Hall carrier concentration. We use a single parabolic band (SPB) model to analyze our measurements and establish the mechanism for obtaining high zT. We show that if the Hall carrier concentration were carefully reduced to 1–2$\times 10^{18}$ cm^{-3} (significantly lower than usually achieved), a zT of 1 at 300 K and above could be possible.

We propose that the carrier concentration dramatically influences the thermoelectric properties of $Ag_{2+x}Se$. Therefore, we begin our discussion of the results with the Hall carrier concentration as a function of temperature, shown in Figure 5.1(a). The curves are differentiated by their room temperature Hall carrier concentrations. The Hall carrier concentration rises then jumps to 3–5$\times 10^{19}$ cm^{-3} at the superionic phase transition temperature, measured by differential scanning calorimetry to be 407 K. Above the phase transition, some samples (Figure 5.1(a), blue and black squares) exhibit the beginning of an exponential increase in the Hall carrier concentration around 600 K, suggesting the influence of holes at that temperature.

The Hall carrier concentration as a function of the nominal Ag excess is given in Table 5.1. However, it is difficult to establish a correlation between the Ag content and the Hall carrier concentration because the actual average Ag content in the matrix phase may differ from the nominal due to the presence of small amounts of impurity phases, e.g., Se in the grain boundaries.

This could be exacerbated due to Ag ion movement during ingot consolidation and hot-pressing. These results present two challenges. First, it is difficult to establish a correlation between the carrier concentration and the Ag content. Second, the hot-pressed samples have greater carrier concentrations than do the ingot samples. To resolve this discrepancy, a sample of Ag_2Se was made with a solid-state powder reaction (SSPR) described in Section 2.1.4. This resulted in an ingot friable enough to be ground in a mortar and pestle, bypassing the ball-milling step used to make the other hot-pressed samples. The Ag_2Se powder made by SSPR was then hot-pressed. As shown in Table 5.1, the SSPR sample has a room temperature carrier concentration more similar to the ingot samples than to the other hot-pressed samples, which were powderized by ball-milling. This suggests that ball-milling drives Se out of the silver selenide ingots, thereby raising the carrier concentration.

Assuming it were possible to control the carrier concentration in $Ag_{2+x}Se$, we can estimate the maximum possible zT at any temperature after we estimate the electron effective mass m^*, the

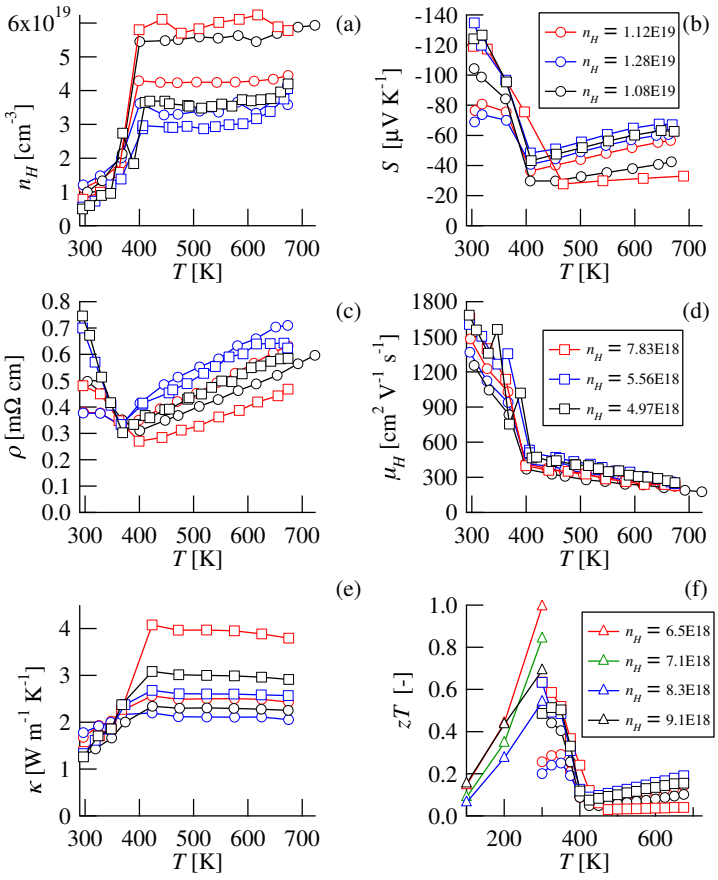

Figure 5.1: Transport properties of $Ag_{2+x}Se$. Circles represent hot-pressed samples, squares represent samples cut from ingots, and triangles are from Aliev [20]. The legends for all figures are shown in (b) and (d). Samples are identified by their room temperature n_H values in units of cm^{-3}. Only heating curves are shown.

mobility parameter μ_0, and the lattice thermal conductivity κ_L. We will estimate these parameters at 300 K, the temperature at which the highest zT in this material has been reported. Because the Hall carrier concentration behavior differs so dramatically above and below the phase transition, we will model the transport properties in each region separately. In our analysis, we use the scaled effective mass model (Section 3.3) as a first approximation for the conduction band as is commonly done to derive the density of states effective mass m^*. This formulation ignores the valence band as if it were completely filled and assumes that holes do not contribute to conduction. The exact formulas used are derived for when the electron mobility is limited by acoustic phonon scattering, which will be discussed later. The mathematical details of this model are given in Chapter 3.

The trend of the Seebeck coefficient with temperature, shown in Figure 5.1(b), can be explained by the behavior of the Hall carrier concentrations of the samples. The magnitude of the Seebeck coefficient drops from over 130 μV K^{-1} at 300 K to less than 30 μV K^{-1} at 407 K for all samples regardless of starting composition and processing method. The Hall carrier concentration is a dra-

Table 5.1: Hall carrier concentrations of $Ag_{2+x}Se$ at 300 K

Nominal Composition	Hot-Pressed [10^{18} cm^{-3}]	Ingot [10^{18} cm^{-3}]
Ag_2Se	11.2	7.83
$Ag_{2.0006}Se$	12.8	5.56
$Ag_{2.0027}Se$	10.8	4.97
Ag_2Se SSPR	6.83	-

matically increasing function of temperature in this region, which can explain the decrease in the Seebeck coefficient. Above the phase transition, where the Hall carrier concentration is relatively constant, the Seebeck coefficient increases with temperature, as expected for materials that can be approximated by a single parabolic band [1]. The Seebeck coefficients of two samples (Figure 5.1(b), blue and black squares) stop increasing around 650 K, concurrent with an observed increase in Hall carrier concentration, which is likely due to the thermal excitation of minority carriers.

We used the n_H and S data (Figure 5.2(a)) to estimate the electron effective mass m^*. The plot includes data from other studies in order to get a more representative value of m^* [19, 20]. While hysteresis between heating and cooling curves, sample inhomogeneity, and measurement instability add uncertainty to our estimate of m^*, the obvious trend seen in Figure 5.2(a) yields an m^* of 0.2 m_e below the phase transition and 0.3 m_e above the phase transition.

The changing Hall carrier concentration can also explain the trend of the resistivity with temperature, shown in Figure 5.1(c). The resistivity drops from 0.4–0.7 mΩ cm at 300 K to $\sim$0.3 mΩ cm at 407 K. The resistivities of two samples (Figure 5.1(c), blue and black squares) roll off to a constant value around 600 K in agreement with the increasing Hall carrier concentration. In the other samples above the phase transition the resistivity increases with temperature, typical of heavily doped semiconductors, due to a decrease in Hall mobility, shown in Figure 5.1(d).

A Hall mobility limited by acoustic phonon scattering will follow a T^{-p} power law, with the value of p greater than 0.5 [31]. The p values found in this study are all greater than 0.5, indicating that acoustic phonons are the dominant scatterers of electrons. There is also a drop in Hall mobility across the superionic transition. This could be because in superionic $Ag_{2+x}Se$, the Ag ions move freely and tend to scatter electrons more efficiently than a static lattice.

We estimated the mobility parameter μ_0 from the Hall mobility and Hall carrier concentration data. The mobility Pisarenko plot is shown in Figure 5.2(b). We estimate a μ_0 of 2800 cm^2 V^{-1} s^{-1} below the phase transition and 1800 cm^2 V^{-1} s^{-1} above the phase transition. The Hall mobilities from Aliev [20] (as high as 6100 cm^2 V^{-1} s^{-1}) and Ferhat [19] (as high as 11610 cm^2 V^{-1} s^{-1}) are not shown in Figure 5.2(b) because they are much greater than the values in this study.

The predicted mobility at room temperature and the optimum carrier concentration is much greater than that for other n-type thermoelectric materials. At the optimum carrier concentration of 1.6×10^{18} cm^{-3}, we predict that $Ag_{2+x}Se$ will have a Hall mobility of 2200 cm^2 V^{-1} s^{-1} at 300 K.

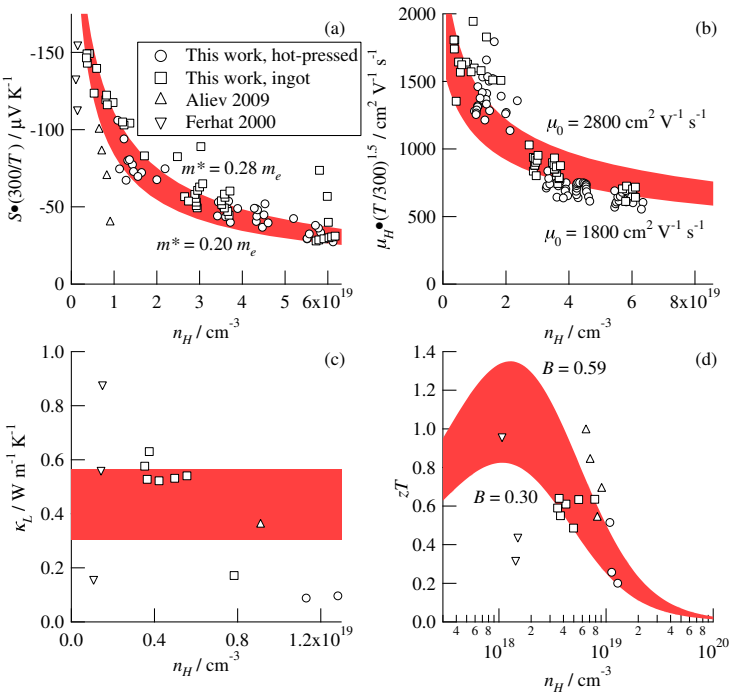

Figure 5.2: Estimation of m^*, μ_0, κ_L, and zT as a function of n_H at 300 K. Symbols have the same meaning as in Figure 5.1. The Hall mobility values from Ferhat [19] and Aliev [20] were not included in Figure 5.2(b) because they are much greater than those obtained in this study. The red bands are predicted curves with the following parameters: (a) upper bound: $m^* = 0.3\ m_e$, lower bound: $m^* = 0.2\ m_e$, (b) upper bound: $\mu_0 = 2800$ cm^2/V s, lower bound: $\mu_0 = 1800$ cm^2/V s, (c) $\kappa_L =$ 0.43 W/m K +/- 30%, 95% confidence bounds for the mean (d) upper bound: zT computed with parameters for T above phase transition and $\kappa_L = 0.4$, lower bound: zT computed with parameters for T below phase transition and $\kappa_L = 0.6$.

At their respective optimum carrier concentrations, I-doped PbTe has a Hall mobility of 1100 cm^2 V^{-1} s^{-1} [65], Te-doped Bi_2Te_3, 212 cm^2 V^{-1} s^{-1} [14], $La_{3-x}Te_4$, 4 cm^2 V^{-1} s^{-1} [66], and n-type $CoSb_3$ has a mobility of 41.2 cm^2 V^{-1} s^{-1} [67]. The large value of the Hall mobility in $Ag_{2+x}Se$ is due to the low effective mass and is the cause of the low optimal carrier concentration. As μ_0 increases, the quality factor B increases, which in turn reduces the optimal carrier concentration [65].

The total thermal conductivity κ is typically considered as containing a lattice contribution κ_L and an electronic portion κ_e as explained in Section 3.2. The electronic portion dominates the total thermal conductivity in $Ag_{2+x}Se$, shown in Figure 5.1(e). κ increases from ~1.5 W m^{-1} K^{-1} at 300 K to 2–4 W m^{-1} K^{-1} above the phase transition. This increase in κ must be driven by the decrease in the resistivity, since κ_L should decrease with temperature. Above the phase transition, κ decreases slightly with temperature. This is driven by the increase in resistivity in this region.

The lattice thermal conductivity κ_L was estimated from samples with the smallest electronic contribution to be 0.43 W m^{-1} K^{-1} with 95% confidence bounds of +/- 30% from the total thermal

conductivity data, the resistivity data, and the Lorenz number as determined by the SPB model. The calculated Lorenz numbers are all within 10% of 1.8×10^{-8} V^2 K^{-2}. The calculated lattice thermal conductivities are shown in Figure 5.2(c), along with those calculated from previous reports [19, 20].

After estimating the values of m^*, μ_0, and κ_L, we proceeded to estimate zT as a function of n_H at 300 K. Our prediction is shown in Figure 5.2(d). The model predicts a zT of 1.1 at a Hall carrier concentration of 1.6×10^{18} cm^{-3}; the predicted zT decreases rapidly above that concentration. The zT values observed in this study (Figure 5.1(f)) vary between 0.2 and 0.7 at 300 K and do not exceed 0.2 above 407 K because their Hall carrier concentrations are close to or greater than 10^{19} cm^{-3}, respectively.

Our model suggests that if the Hall carrier concentration were 1.6×10^{18} cm^{-3} above the phase transition, zT would reach approximately 1.2 at 420 K and 1.3 at 600 K. However, we assumed only a single conduction band, while the increase in Hall carrier concentration in some samples at 600 K (Figure 5.1(a)) suggests the presence of minority carriers in the valence band at high temperatures. Therefore we predict a broad zT peak near and above 1 between 420 K and 600 K, followed by a decrease in zT at higher temperatures.

The low carrier concentration in $Ag_{2+x}Se$ makes it challenging to achieve the optimum carrier concentration. Thermoelectric materials typically have optimum carrier concentrations in the middle 10^{19} cm^{-3} to the high 10^{20} cm^{-3} range. For example, I-doped PbTe exhibits a maximum zT at 2.9×10^{19} cm^{-3} [65], and Te-doped Bi_2Te_3 has a maximum zT at 2.3×10^{19} cm^{-3} [68]. n-type $CoSb_3$ has an optimum carrier concentration of 1.4×10^{20} cm^{-3} [67] and $La_{3-x}Te_4$ has an optimum carrier concentration of 9×10^{20} cm^{-3} [66]. These carrier concentrations are within the range that can be easily controlled by doping. If a composition of silver, selenium, and a third element with a Hall carrier concentration near the predicted optimum could be found, as in the bismuth antimony telluride solid solutions [69], it may be possible to achieve a zT greater than 1. Au is soluble in the superionic phase of silver selenide and Au-doping of Ag_2Se results in increased Seebeck coefficients at 603 K [70], suggesting another strategy for increasing the thermoelectric performance.

In addition to having a low optimum carrier concentration compared to other thermoelectric materials, Ag_2Se is difficult to optimize because its silver-rich form, $Ag_{2+x}Se$, is more thermodynamically stable [71, 72], just as Cu_2Se is more stable with Cu vacancies ($Cu_{2-x}Se$) [16]. This tendency toward defect-rich stoichiometry makes it difficult to reduce the carrier concentration in superionic conductors just by reducing the non-stoichiometry in the material.

We have measured the Hall carrier concentration, Seebeck coefficient, resistivity, and thermal conductivity of $Ag_{2+x}Se$ from 300 K to 673 K, a temperature range never before explored for this material. Additionally, we have successfully used a scaled effective mass model to explain the trends in the transport properties with temperature and Hall carrier concentration, and to calculate

the effective mass, mobility parameter, and lattice thermal conductivity. Our model suggests that the zT of this material is determined by the Hall carrier concentration and that a zT greater than 1 from 300 K to 600 K can be achieved if the Hall carrier concentration can be reduced to 1.6×10^{18} cm^{-3}. Hence, we have successfully explained the variation in the previously reported values of the thermoelectric efficiency of this material and have provided a mechanism for optimizing its thermoelectric performance.

5.3 Two-Band Character of $Ag_{2+x}Se$

In Section 5.2 we treated $Ag_{2+x}Se$ as being influenced by only a single conduction band at 300 K. This treatment is supported by the behavior of the Seebeck coefficient with Hall carrier concentration. The influence of the valence band would manifest itself as a peak followed by a decline in the Seebeck coefficient as the Hall carrier concentration decreases, which we do not observe. However, $Ag_{2+x}Se$ has been variously reported as a narrow-gap semiconductor [73] and as a semimetal [74], implying that the valence band should play a role as the Fermi level decreases. The two-band character of $Ag_{2+x}Se$ shows itself in measurements of the Seebeck coefficient from 20 K to 330 K, shown in Figure 5.3. As temperature increases, the Fermi level decreases (Section 3.1) and moves toward the valence band. This increases the concentration of holes in the n-type material, the Seebeck voltage of which reduces the Seebeck voltage of the electrons. Figure 5.3 contains an estimate for the band gap E_g using the Goldsmid-Sharp relation [75].

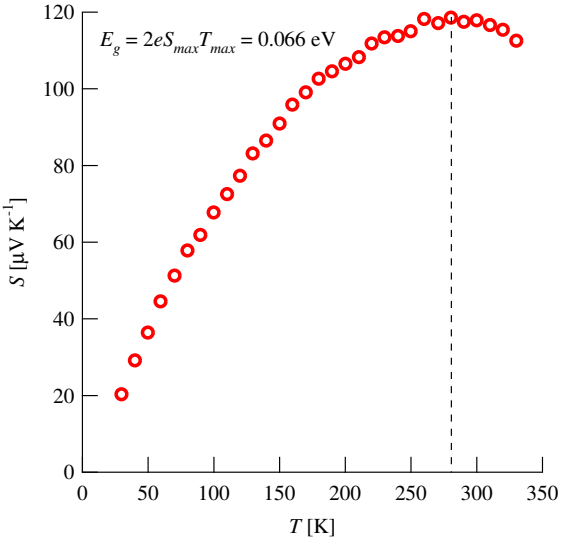

Figure 5.3: The peak in Seebeck coefficient implies the presence of minority carriers.

The previous work supporting the small or even negative band gap of $Ag_{2+x}Se$ along with our measurements of the Seebeck coefficient suggests that a two-band treatment may be necessary to

understand the transport properties of $Ag_{2+x}Se$. To begin, we need to know something about the valence band of $Ag_{2+x}Se$. The effective mass m_V^* is estimated to be 0.75 m_e from DFT calculations [74]. Scaling the conduction band mobility parameter of 1800 cm^2 V^{-1} s^{-1} by the $m^{*-5/2}$ relation (Equations 3.19 and 4.1), we estimate the mobility parameter of the valence band $\mu_{0,V}$ to be 170 cm^2 V^{-1} s^{-1}. We use these values of the valence and conduction band parameters along with the equations for the individual transport properties found in Section 3.2 to compute the two-band transport properties using Equations 5.1 through 5.4 [76]. Note that in these equations S_i and $R_{H,i}$ are signed quantities.

$$\sigma = \sum_i \sigma_i \tag{5.1}$$

$$S = \frac{\sum_i S_i \sigma_i}{\sigma} \tag{5.2}$$

$$R_H = \frac{\sum_i R_{H,i} \sigma_i^2}{\sigma^2} \tag{5.3}$$

$$\kappa = \kappa_L + \sum_i L_i \sigma_i T + \sum_i S_i^2 \sigma_i T - S^2 \sigma T \tag{5.4}$$

We convert the n_H versus zT data to R_H versus zT data, since R_H is what we actually measure; R_H cannot be converted into a single-band Hall carrier concentration if two bands influence transport. The results are shown in Figure 5.4(a) along with bounds on zT generated from the estimated valence band properties, the conduction band properties from Figure 5.2, and Equations 5.1 through 5.4. The range of possible values of R_H versus zT covers the data for $Ag_{2+x}Se$ quite well, suggesting that the influence of the valence band on transport is responsible for the low zT values observed in $Ag_{2+x}Se$.

The work suggesting two-band behavior in $Ag_{2+x}Se$ shows that as the Hall carrier concentration is reduced in the material, the valence band will degrade the thermoelectric properties. This behavior is shown in Figure 5.4(b) by the blue curve and the red curve. Some ways of dealing with this problem include reducing the valence-band mobility and increasing the band gap. We have shown in Section 4.2 that doping with Br on the Se site reduces the valence band mobility of copper selenide. The samples with composition $Cu_2Se_{0.95}Br_{0.05}$ have a mobility parameter 59% less than that of Cu_2Se (Figure 4.5). The green curve in Figure 5.4(b) was generated by assuming the same reduction in $\mu_{0,V}$ of silver selenide by doping with Br and counter-doping with Ag vacancies to maintain the same Fermi level. Previous work on Ag_2Te shows that substitution of Ag by Pb can increase the band gap by up to 40% [77]. The purple curve in Figure 5.4(b) is a prediction of η versus zT, assuming the same percent increase in the band gap of silver selenide.

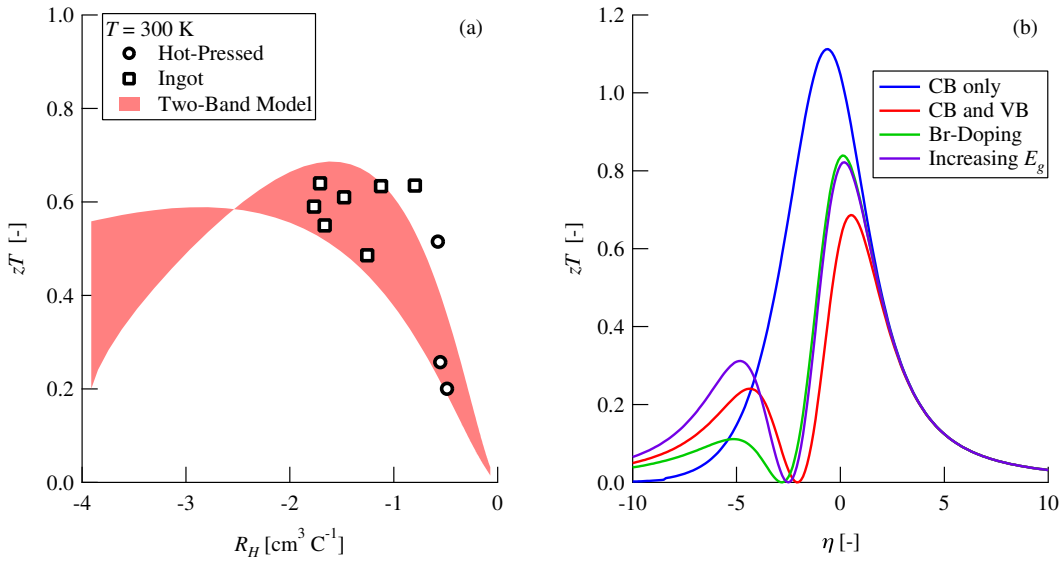

Figure 5.4: (a) The hot-pressed and ingot R_H versus zT data are well-described by a two-band model, suggesting that minority carriers are the cause of low zT values in Ag_2Se at room temperature. (b) The red curve shows the zT predicted for a single conduction band (CB) in $Ag_{2+x}Se$. The blue curve is the zT predicted for a valence band (VB) separated from the conduction band by a band gap of 0.066 eV. The green curve shows the zT expected from reducing $\mu_{0,V}$ by 59% from Br doping, and the purple curve is that from increasing E_g by 40%.

Some of the performance of $Ag_{2+x}Se$ predicted by Figure 5.2 is predicted to be recovered by either doping with Br to reduce the valence band mobility or by increasing the band gap to reduce the influence of the valence band on transport. Further work characterizing samples of $Ag_{2+x}Se$ with η closer to the valence band is needed to fully understand how to maximize the thermoelectric performance of this material.

5.4 $Ag_2Se_{1-x}Te_x$

As stated above, Ag_2Se could exhibit high thermoelectric performance if a soluble third element could reduce its carrier concentration. To that end we investigated $Ag_2Se_{0.5}Te_{0.5}$. The phase diagram of the Ag_2Se-Ag_2Te pseudo-binary system is shown in Figure 5.5, which shows a broad range of solubility of Te in Ag_2Se both above and below the superionic transition.

The transport properties of $Ag_2Se_{0.5}Te_{0.5}$ are shown in Figure 5.6. The sample was measured several times on each measurement system, and Figure 5.6 shows that the transport property curves stabilize after three measurements. The room temperature properties of $Ag_2Se_{0.5}Te_{0.5}$ are similar to those of Ag_2Se. The Hall carrier concentration of $Ag_2Se_{0.5}Te_{0.5}$ at room temperature is about 5×10^{18} cm^{-3} and zT is about 0.8, which is within the range of expected zT values in Figure 5.2.

Above the superionic transition at 407 K, the transport properties of $Ag_2Se_{0.5}Te_{0.5}$ are very

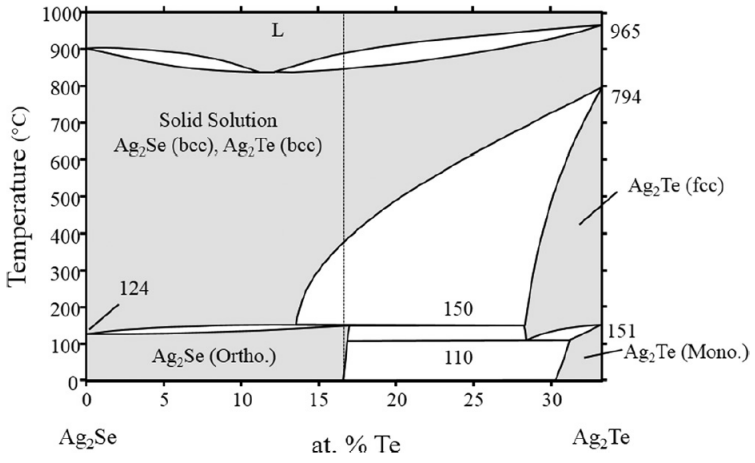

Figure 5.5: $Ag_2Se_{0.5}Te_{0.5}$ is a solid solution at room temperature and above 350°C. Reprinted with permission from *App. Phys. Lett.*, v. 103, no. 14, article no. 143906, (2013). Copyright 2013, AIP Publishing LLC.

different from those of Ag_2Se. Figure 5.6 shows that Hall carrier concentration of $Ag_2Se_{0.5}Te_{0.5}$ is an order of magnitude less than that of Ag_2Se in the same temperature range (Figure 5.1). Since Ag_2Se is overdoped at room temperature and much more so above the superionic transition, it is reasonable to think a reduction in the Hall carrier concentration at high temperature would lead to increased thermoelectric performance. The zT of $Ag_2Se_{0.5}Te_{0.5}$ versus temperature is shown in Figure 5.7.

$Ag_2Se_{0.5}Te_{0.5}$ shows a large degree of hysteresis in zT across the superionic phase transition, i.e. the heating and cooling curves in Figure 5.7 do not line up with one another below 407 K. This is possibly caused by kinetically slow processes which take longer than the measurement time to settle. However, the heating and cooling curves above the superionic phase transition do not show hysteresis. We will restrict our analysis of the thermoelectric performance to temperatures above 520 K. We will use the scaled SPB model described in Section 3.3 because only two samples are available, and we will estimate the optimum carrier concentration and maximum zT at 520 K because this is the temperature at which the maximum hysteresis-free zT value is observed. It must be mentioned that at 520 K $Ag_2Se_{0.5}Te_{0.5}$ is a composite comprising a matrix of Te-doped Ag_2Se and impurities of Se-doped Ag_2Te (see Figure 5.5), the properties of which are unknown. However, we know from simple matrix algebra that the zT of a composite cannot exceed the zT values of the components [39], assuming no interactions between the composites such as electron energy filtering, minority carrier filtering, or interfacial phonon scattering [7]. This means that the zT of $Ag_2Se_{0.5}Te_{0.5}$ is an underestimate of the matrix phase of the material, and that any prediction we make of zT will also be an underestimate. The techniques explained in Chapter 7 for extracting individual component properties from composite measurements would be useful for determining the actual zT of the value

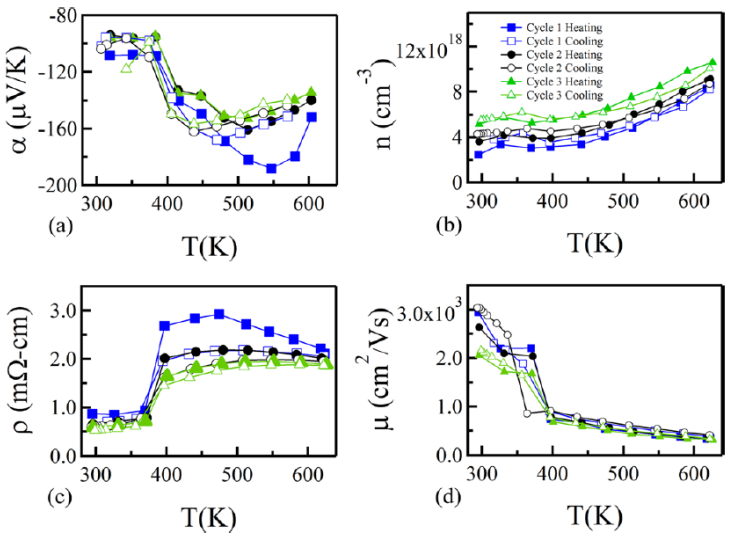

Figure 5.6: Transport properties of $Ag_2Se_{0.5}Te_{0.5}$. Consecutive measurement cycles show that the properties converge onto curves that are stable under heating and cooling. (a) The magnitude of the Seebeck coefficient reaches a peak around 450 K, and then declines due to bipolar conduction. (b) The Hall carrier concentration starts to increase around 450 K, supporting the conclusion of bipolar conduction reached through the Seebeck data. (c) The resistivity is somewhat flat above and below the phase transition. (d) The Hall mobility exhibits a high value of over 2000 $cm^2\ V^{-1}\ s^{-1}$ after multiple measurement cycles. Reprinted with permission from *App. Phys. Lett.*, v. 103, no. 14, article no. 143906, (2013). Copyright 2013, AIP Publishing LLC.

for the matrix as well as the maximum possible zT for a material with the same composition as the matrix phase. Such a measurement was not possible at the time this study was conducted due to temperature limitations of the PPMS heating equipment.

The results of the scaled SPB model on Ag_2Se and $Ag_2Se_{0.5}Te_{0.5}$ at 520 K are shown in Figure 5.8. $Ag_2Se_{0.5}Te_{0.5}$ has a slightly greater effective mass, and a much lower mobility parameter μ_0 resulting from the $m^{*-5/2}$ relation for the mobility parameter in the acoustic phonon scattering regime (Equations 3.19 and 4.1). $Ag_2Se_{0.5}Te_{0.5}$ also has a much lower lattice thermal conductivity of 0.17 W m^{-1} K^{-1} compared to the value for Ag_2Se, 0.33 W m^{-1} K^{-1}. This leads to an overall increase in the quality factor B. $Ag_2Se_{0.5}Te_{0.5}$ is also closer to its own optimum n_H value than is Ag_2Se. Both of these facts account for the zT of 1.2 reached in $Ag_2Se_{0.5}Te_{0.5}$ at 520 K, much greater than the values around 0.2 observed in Ag_2Se. If the carrier concentration of $Ag_2Se_{0.5}Te_{0.5}$ could be reduced to 1.4×10^{18} cm^{-3}, the material could achieve a zT of 1.7 at 520 K, a very competitive value for waste-heat recovery applications.

Why does adding Te to Ag_2Se improve the thermoelectric performance so much? The increase in quality factor is due to the reduced lattice thermal conductivity, which can be understood in terms of mass contrast on the anion site [78]. Mass contrast, i.e. a difference in mass between the incumbent atom and its substituent, reduces the phonon density of states, leading to a reduced group

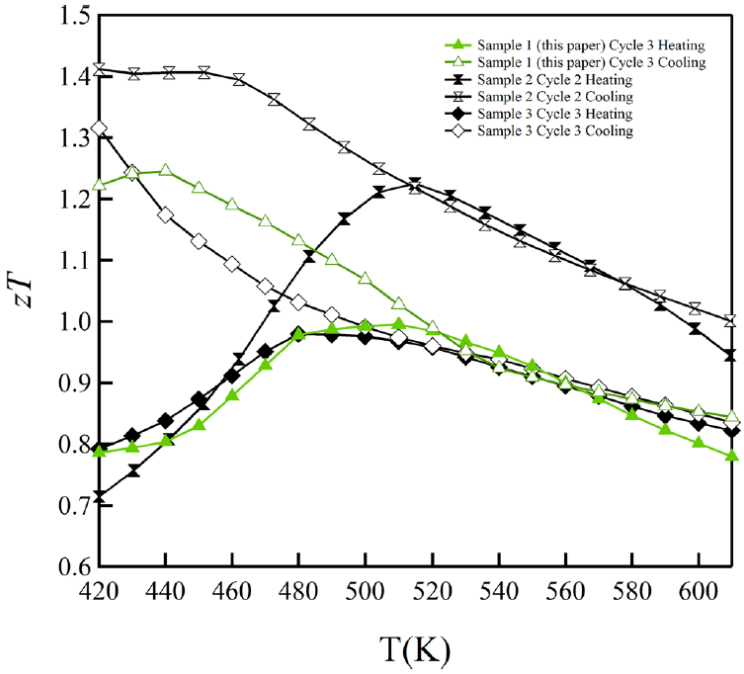

Figure 5.7: Differences in carrier concentration between samples of $Ag_2Se_{0.5}Te_{0.5}$ lead to different values of zT. Reprinted with permission from *App. Phys. Lett.*, v. 103, no. 14, article no. 143906, (2013). Copyright 2013, AIP Publishing LLC.

velocity and therefore a lower thermal conductivity. The reduction of the Hall carrier concentration is more difficult to understand, especially because previous work has shown that substituting one chalcogen for another of greater atomic mass increases the conductivity, presumably by increasing the Hall carrier concentration [62]. The chalcopyrite materials in [62] are wide-gap semiconductors, i.e. the Fermi level is in the band gap. Substituting Se for S in Cu_2ZnGeS_4 shifts the valence band toward the Fermi level due to the greater overlap of the Se orbitals, resulting in a greater carrier concentration and greater conductivity. Because Ag_2Se is an Ag^+ conductor, it contains many interstitial Ag defects [79, 80, 81], which places its Fermi level within the conduction band. Substituting Se for Te in ZnSe and CdSe is known to reduce the band gap and move the conduction band minimum closer to the n-type pinning energy, the Fermi level beyond which no further doping is possible due to the spontaneous formation of electron acceptors [82]. The carrier concentration data on $Ag_2Se_{0.5}Te_{0.5}$ in Figure 5.6(b) show an exponential increase starting at 450 K, which is not observed in the carrier concentration of Ag_2Se (Figure 5.1(a)), suggesting that adding Te reduces the band gap in Ag_2Se. We propose that substituting Te for Se in Ag_2Se moves the conduction band minimum closer to the n-type pinning energy, thereby reducing the carrier concentration in the material.

$Ag_2Se_{0.5}Te_{0.5}$ was not the only composition synthesized and measured in this study. A sample of $Ag_2Se_{0.75}Te_{0.25}$ was also synthesized, but no Hall effect data were measured on it. As a result,

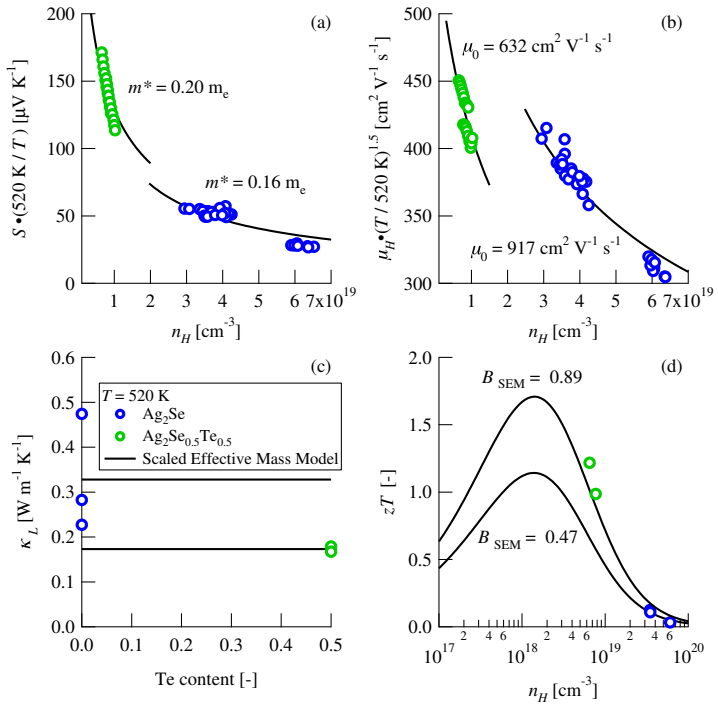

Figure 5.8: Scaled effective mass model applied to Ag_2Se and $Ag_2Se_{0.5}Te_{0.5}$ at 520 K. (a) Doping with Te results in a greater effective mass. (b) The increased effective mass of the Te-doped samples results in a lower mobility parameter. However, the weighted mobility values $(\mu_0 (m^*/m_e)^{3/2}$ for the two materials are nearly identical. (c) Mass contrast on the anion site results in a lower lattice thermal conductivity in $Ag_2Se_{0.5}Te_{0.5}$. (d) The lower thermal conductivity and the reduced Hall carrier concentration yield greater zT values for $Ag_2Se_{0.5}Te_{0.5}$, as well as a greater predicted maximum zT.

we cannot add its properties to the scaled effective mass model. We can, however, take the Seebeck coefficient, resistivity, and thermal conductivity of both compositions of $Ag_2Se_{1-x}Te_x$ and apply the scaled weighted mobility model described in Section 3.3 to obtain a quality factor for $Ag_2Se_{1-x}Te_x$ without using Hall effect data. Estimates for the weighted mobility $\mu_0 (m^*/m_e)^{3/2}$ along with model curves and the scaled S versus scaled σ data are shown in Figure 5.9, which shows that fitting the weighted mobility to scaled Seebeck coefficient versus conductivity data yields a weighted mobility very close to that obtained by the scaled effective mass model in which the effective mass and mobility parameter are modeled separately.

The lattice thermal conductivity values computed with and without Hall data are equal since they are calculated from the Seebeck coefficient and the conductivity. The estimated weighted mobility and the lattice thermal conductivity are used to calculate the quality factor from Equation 3.26. The quality factor can then be used to generate a prediction of zT versus conductivity, shown in Figure 5.9. Since the lattice thermal conductivity values from the two models are the same and the estimated weighted mobility values are very similar, Figure 5.9 shows that analyzing scaled Seebeck data versus scaled conductivity data yields a quality factor within 10% of that estimated by the

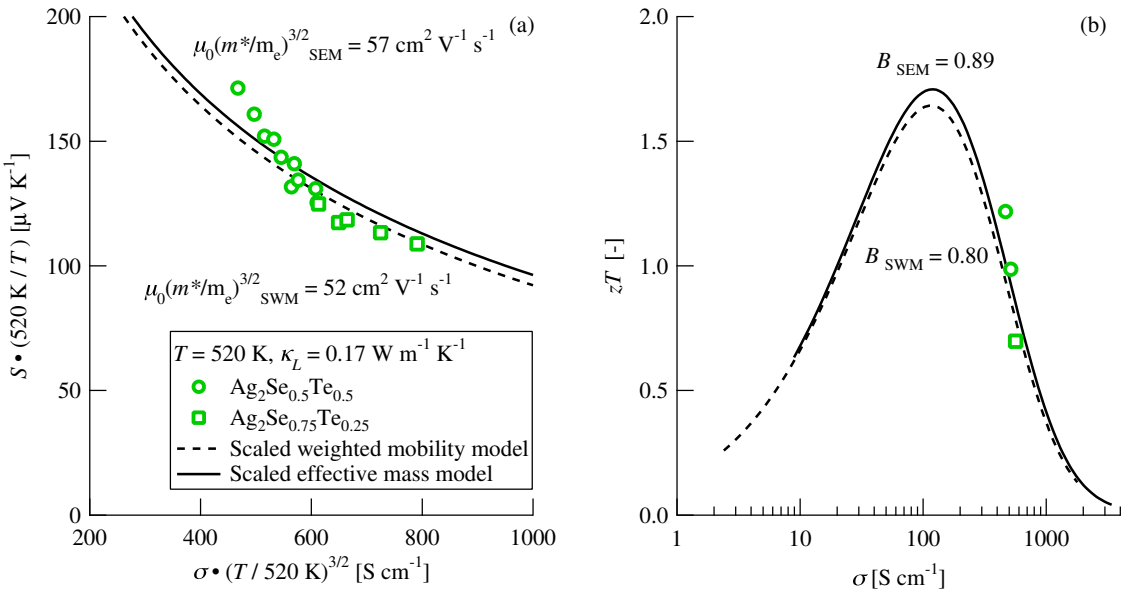

Figure 5.9: (a) The dashed line shows the result of using the weighted mobility $\mu_0 (m^*/m_e)^{3/2}$ as a fitting parameter to fit a model curve of the Seebeck coefficient versus conductivity data appropriately scaled with temperature. The values from the scaled weighted mobility model and the scaled effective mass model are within 10% of one another. (b) Using the data from $Ag_2Se_{1-x}Te_x$ at x equal to 0.25 and 0.5 and the scaled weighted mobility model yields a maximum zT of 1.6, whereas using the data with x equal to 0.5 and the scaled weighted mobility model yields a maximum zT of 1.7.

scaled effective mass model used in [21].

While Hall effect data should be taken on new thermoelectric materials in order to obtain the best understanding of the charge carrier transport, this is not always possible due to time and budget constraints. Furthermore, temperatures of interest may not be accessible in available Hall effect equipment due to the cooling requirements of the magnets. The scaled weighted mobility model allows researchers to determine the quality factor and therefore the maximum zT in new materials with small numbers of or even single samples without measuring the Hall effect. Furthermore, it allows researchers to reanalyze old data that may not include Hall carrier concentration or mobility values. The scaled weighted mobility model is a method for rapidly identifying new materials and for resurrecting previously overlooked materials with high potential for thermoelectric performance.

5.5 Conclusions

Ag_2Se shows promising thermoelectric properties, as evidenced by the scaled effective mass analysis (Figure 5.2). However, Ag_2Se is most likely a semimetal or a narrow gap semiconductor, so reducing the carrier concentration to the optimum level could result in bipolar conduction and reduced thermoelectric performance. Ways of mitigating this problem include alloying to reduce the band gap

and counterdoping with Br and Ag vacancies to reduce the valence band mobility. These methods are based on the idea that the carrier concentration can be reduced from its native level. Another way of reducing the carrier concentration is to reduce the maximum carrier concentration below its native level. This is the means by which Te reduces the carrier concentration, as shown by Hall carrier concentration measurements on $Ag_2Se_{0.5}Te_{0.5}$ and Ag_2Se (Figure 5.8). Alloying with Te has the added benefit of reducing the lattice thermal conductivity, which together with the reduced carrier concentration explains the zT of 1.2 achieved in $Ag_2Se_{0.5}Te_{0.5}$ at 520 K, and predicts a maximum zT of 1.7 in this material at the same temperature.

Chapter 6

Copper Sulfide

6.1 Introduction

Copper sulfide ($Cu_{2-x}S$) was investigated as a thermoelectric material because it transitions to a copper-ion conducting phase at 700 K, much like the high-performance thermoelectric material Cu_2Se [16].

$Cu_{2-x}S$ has been intensively studied for more than fifty years, mainly focusing on its structural complexity and applications in solar cells due to its band gap of 1.2 eV, close to the optimum value for capturing the broadest range of the solar spectrum [83, 84, 42, 85]. Similar to copper selenide, copper sulfide shows very complicated low temperature crystal structures. The stoichiometric compound Cu_2S possesses two phase transitions [86]. One is at about 370 K and another is around 700 K. Below 370 K, it is called low chalcocite γ phase (L-chalcocite). The second, between 370 K and 700 K, is called high chalcocite β phase (H-chalcocite). Above 700 K, Cu_2S transfers to α phase with a fcc cubic structure. Similar to Cu_2Se, while the sulfur atoms maintain a rigid sublattice, the Cu ions are distributed throughout many possible positions [83], which is indicative of the high degree of disorder and low threshold for ion motion that is characteristic of liquid-like behavior. Indeed, the α phase is a classic superionic phase having freely mobile copper ions [87], while the H-chalcocite β phase has recently been reported to be a solid-liquid hybrid phase with Cu in a liquid-like substructure [88].

6.2 Transport Properties

The high temperature thermoelectric properties of $Cu_{2-x}S$ synthesized and measured at the Shanghai Institute of Ceramics are shown in Figure 6.1. The ideal Cu_2S without copper deficiency is an

intrinsic semiconductor. Because of some copper deficiency, even in the sample with nominal composition Cu_2S, all samples show p-type conduction with holes as the dominant charge carriers. The measured room temperature carrier concentration is shown in Table 6.1. With increasing copper deficiency from Cu_2S to $Cu_{1.98}S$, and finally to $Cu_{1.97}S$, the hole concentration is significantly increased from about 10^{18} cm^{-3} to 10^{20} cm^{-3}, leading to increased electrical conductivity and reduced Seebeck coefficient.

Table 6.1: Debye temperature (Θ_D), coefficients of thermal expansion (CTE) of high temperature liquid-like phases, and room temperature carrier density n_H, hole mobility (μ_H), shear (v_s), longitudinal (v_l), and averaged speed of sound (v_{avg}), bulk (B_T) and shear modulus (G_T), and Grüneisen parameter (γ) of bulk $Cu_{2-x}S$ (x = 0, 0.02, 0.03) and Cu_2Se.

Material	Cu_2S	$Cu_{1.98}S$	$Cu_{1.97}S$	Cu_2Se
n_H at 300 K [10^{19} cm^{-3}]	0.48	13.30	72.70	48.30
μ_H at 300 K [cm^2 V^{-1} s^{-1}]	16.40	1.86	0.69	15.56
n_H at 750 K [10^{19} cm^{-3}]	2.76	5.22	15.6	201
S at 750 K [μV K^{-1}]	338	295	242	192
v_s [m s^{-1}]	1773	1776	1763	2320
v_l [m s^{-1}]	3634	3711	3818	3350
v_{rms} [m s^{-1}]	1991	1997	1986	2523
v_{avg} [m s^{-1}]	2393	2421	2448	2663
Θ_D [K]	237	238	237	292
B_T [GPa]	50.95	54.19	59.28	27.28
G_T [GPa]	17.77	17.87	17.66	36.29
CTE [10^{-6} K^{-1}]	29.0	38.2	37.4	23.0
γ [-]	1.67	2.33	2.49	0.77
$\kappa_{min,allmodes}$ [W m^{-1} K^{-1}]	0.64	0.65	0.66	0.67
$\kappa_{min,long}$ [W m^{-1} K^{-1}]	0.32	0.33	0.34	0.28
κ_u at 750 K [W m^{-1} K^{-1}]	1.6	1.1	1.0	16.9

The temperature dependence of the thermal conductivity is shown in Figure 6.1. Compared to the electrical properties, the thermal conductivity is much less affected by copper deficiency in $Cu_{2-x}S$. In the whole experimental temperature range, the values of the total thermal conductivity of all $Cu_{2-x}S$ (x = 0, 0.02, 0.03) samples are below 0.6 W m^{-1} K^{-1}, which is remarkably low even among thermoelectric materials.

All the $Cu_{2-x}S$ samples show three different behaviors from 300 K to 1000 K. This corresponds to the three different crystal structures mentioned above. The low-chalcocite γ phase shows an increasing electrical conductivity with increasing temperature, typical of intrinsic semiconducting behavior. The cubic-chalcocite α phase shows a decreasing electrical conductivity with increasing temperature, a typical metallic behavior. Consistent with the electrical conductivity, the Seebeck coefficient and thermal conductivity also show three different trends with temperature. The low temperature low-chalcocite γ phase shows a decreasing thermal conductivity with increasing temperature, typically observed in crystalline solids where acoustic phonons dominate heat transport [89]. The high-temperature high-chalcocite β and cubic-chalcocite α phases show a more temperature-independent

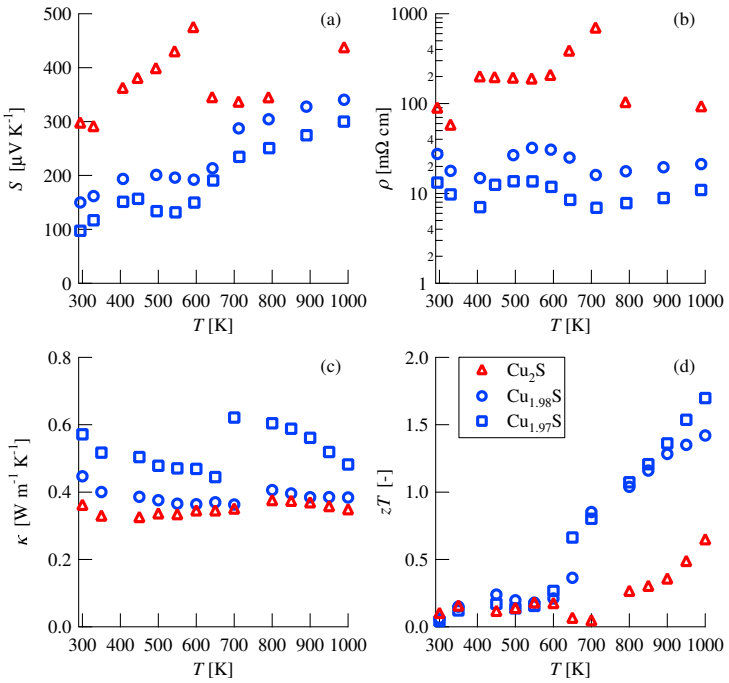

Figure 6.1: Transport properties of $Cu_{2-x}S$. (a) Changing the degree of non-stoichiometry x leads to dramatic changes in the Seebeck coefficient. The phase transitions at 370 K and 700 K are manifested as abrupt changes in the Seebeck coefficient. (b) The resistivity likewise changes over two orders of magnitude due to changes in the copper vacancy concentration. (c) The thermal conductivity is below 1 W m^{-1} K^{-1} at all temperatures in all samples due to the mobile Cu ions in the superionic phase and the low-symmetry crystal structure at lower temperatures. (d) $Cu_{1.97}S$ achieves a zT of 1.7 at 1000 K. The zT plot also highlights the difference in thermoelectric properties between the samples with x greater than zero and that with x equal to zero. This is because the presence of copper vacancies results in a different crystal structure and therefore different transport behavior.

thermal conductivity, which indicates the high disorder of the liquid-like copper ions.

The calculated thermoelectric figure-of-merit zT is shown in Figure 6.1. Similar to the individual electrical and thermal properties, zT also shows three different trends in the measured temperature range, corresponding to the low-chalcocite γ, high chalcocite β, and cubic-chalcocite α phases, respectively. The large band gap in $Cu_{2-x}S$ results in low electrical conductivity but large Seebeck coefficient. In addition, a large band gap is needed for high zT at high temperature to avoid bipolar conduction (Figure 6.1). The measured maximum zT values reach 1.4 at 1000 K for $Cu_{1.98}S$, and 1.7 at 1000 K for $Cu_{1.97}S$, among the highest values in bulk thermoelectric materials, and greater than the highest measured zT of $Cu_{2-x}Se$, 1.5 at 1000 K [16].

6.3 Optimization of Thermoelectric Performance

In order to understand why $Cu_{2-x}S$ has superior thermoelectric performance compared to $Cu_{2-x}Se$, we modeled the electronic properties of both systems using a single parabolic band model with the hole mobility limited by acoustic phonon scattering. Stoichiometric Cu_2S was excluded from the analysis because it has a different crystal structure from that of the vacancy-doped compound [86]. This model assumes a single type of carrier, so we apply the model at 750 K to avoid the region of bipolar conduction in $Cu_{2-x}Se$ and to avoid the phase transition around 700 K in $Cu_{2-x}S$. Our estimates of the effective mass m^*, the mobility parameter μ_0, the deformation potential Ξ, the lattice thermal conductivity κ_L, the quality factor B (Equation 3.26), the optimum Hall carrier concentration, and the maximum predicted zT of both materials are shown in Table 6.2, and the predicted curves of zT versus Hall carrier concentration are shown in Figure 3. The Lorenz numbers calculated are about 1.6×10^{-8} V^2 K^{-2} for $Cu_{2-x}Se$ and $Cu_{2-x}S$.

Table 6.2: Comparison of electronic band parameters and lattice thermal conductivities of $Cu_{2-x}S$ and $Cu_{2-x}Se$ at 750 K.

Material	$Cu_{2-x}S$	$Cu_{2-x}Se$
$m^*[m_e]$	2.1	6.5
μ_0 [cm^2 V^{-1} s^{-1}]	7.7	1.9
Ξ [eV]	7.7	3.3
κ_L [W m^{-1} K^{-1}]	0.38	0.58
B [-]	0.40	0.35
$n_{H,opt}$ [10^{20} cm^{-3}]	1.3	7.9
zT_{max} [-]	1	0.93

Comparing the mobility parameters and effective masses of $Cu_{2-x}S$ and $Cu_{2-x}Se$, the numerator of the quality factor of $Cu_{2-x}Se$ is greater than that of $Cu_{2-x}S$, which explains why the highest reported power factor for $Cu_{2-x}Se$, 12 μW cm^{-1} K^{-2}, is greater than that of $Cu_{2-x}S$, 8.1 μW cm^{-1} K^{-2}. However, $Cu_{2-x}S$ has a greater quality factor due to its lower lattice thermal conductivity, which is why $Cu_{2-x}S$ has a greater potential maximum zT, as shown in Figure 6.2. Since both materials are in the ion-conducting phase at 700 K, their thermal transport behavior is comparable to that of an amorphous phase, meaning the minimum thermal conductivity is a function of only the atomic volume and the speed of sound (Equation 6.1). Table 6.1 shows that $Cu_{2-x}S$ has a lower mean speed of sound than does Cu_2Se, which explains its lower lattice thermal conductivity. According to Figure 6.2 and our estimates of the optimum Hall carrier concentrations from the single parabolic band model, the $Cu_{2-x}S$ samples also have Hall carrier concentrations closer to their respective optimum than do the $Cu_{2-x}Se$ samples, which is why the particular $Cu_{2-x}S$ samples measured have greater zT values than those reported for $Cu_{2-x}Se$. The detrimental effect of the higher deformation potential [90] in $Cu_{2-x}S$ is compensated by the lower effective mass [60] compared to Cu_2Se (see Equation 3.35).

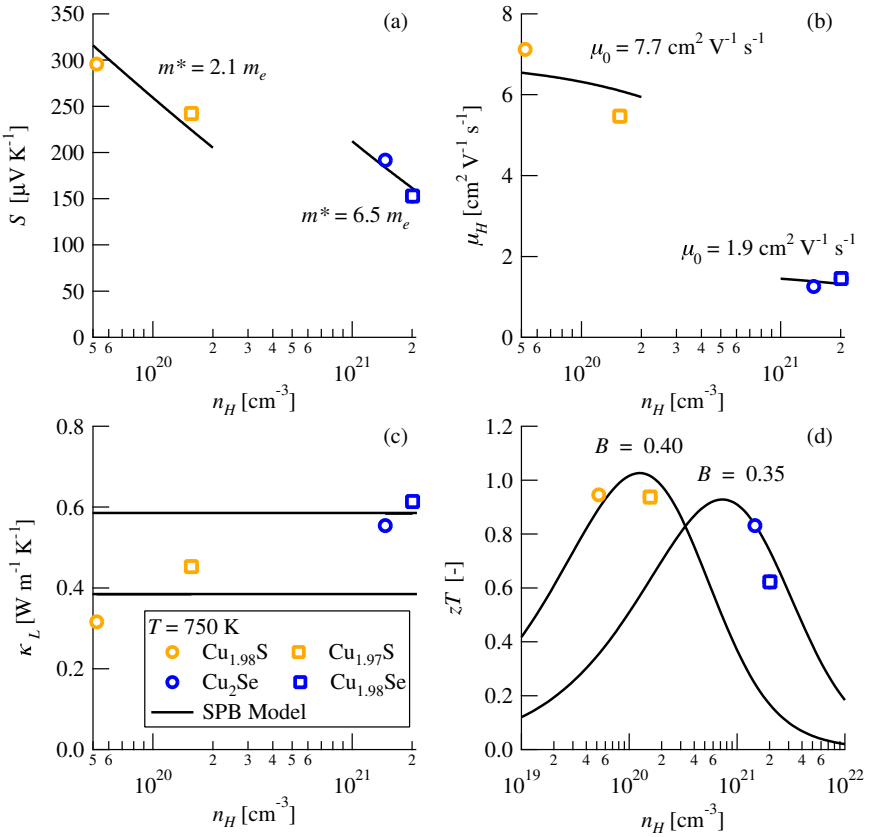

Figure 6.2: (a) Copper sulfide has a lower effective mass than does copper selenide. (b) The lower effective mass in copper sulfide results in a greater mobility parameter. (c) Copper sulfide has a lower lattice thermal conductivity, a result which is supported by speed of sound measurements. (d) Copper sulfide ultimately achieves greater zT values than does copper selenide due to its lower lattice thermal conductivity and its more optimum Hall carrier concentration.

Another advantage of $Cu_{2-x}S$ over Cu_2Se is the ease with which it can be doped. The stoichiometric compound Cu_2S has a Hall carrier concentration of 3.7×10^{19} cm^{-3} at 750 K; raising that value to the optimum of 1.2×10^{19} cm^{-3} is a simple matter of synthesizing the material with Cu vacancies. Cu_2Se, on the other hand, is overdoped, i.e., a means is needed to remove holes from the material. This can be done to some extent with Ag-doping (see Section 4.3) above the superionic transition at 407 K, but is much more difficult to do at room temperature because the optimum carrier concentration is about 3×10^{19} cm^{-3}, far below the lowest carrier concentration achieved in Cu_2Se in this study, which is about 4×10^{20} cm^{-3}.

Here again we point out the utility of obtaining a quality factor from scaled conductivity data. Hall effect measurements are usually conducted on a temperature ramp, i.e., the sample is heated at a consistent rate of change of temperature, and resistivity and Hall coefficient measurements are performed while the temperature changes. This technique leads to scattered Hall carrier concentration data for high-resistivity samples (greater than 10 mΩ cm). In this case, the Hall carrier

concentration must be measured multiple times at a fixed temperature in order to obtain an accurate measurement. This was done for $Cu_{2-x}S$ and also for $Cu_{2-x}Se$ in order to acquire consistent results for comparing the two materials. This is a time-consuming way to optimize the thermoelectric properties. The resistivity is easier to measure on a temperature ramp, so for high-resistivity materials, more resistivity versus temperature data points can be collected than can Hall carrier concentration versus temperature points. This results in a faster estimate for the quality factor in high-resistivity materials than could be derived from Hall effect data. The data and predicted curve for the scaled Seebeck coefficient and conductivity of $Cu_{2-x}S$ at 750 K are shown in Figure 6.3. The curves generated by the scaled weighted mobility model are very close to those generated by the scaled effective mass model using fixed-temperature Hall effect data.

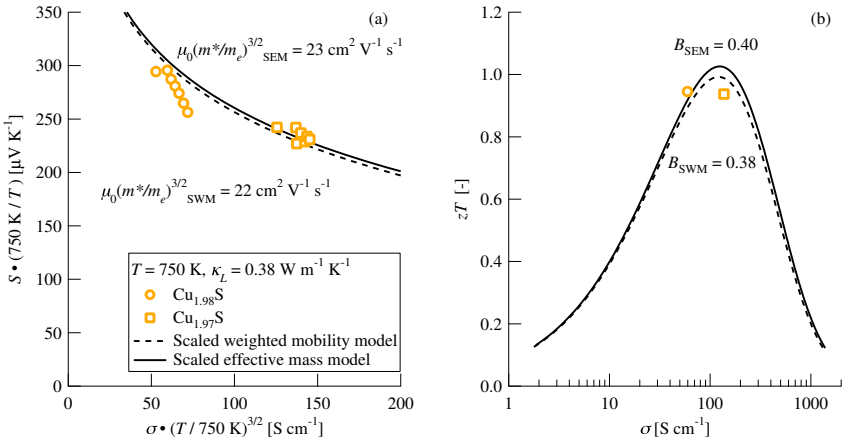

Figure 6.3: Estimating the weighted mobility from scaled Seebeck and conductivity data on $Cu_{2-x}S$ leads to a quality factor within 5% of that derived from Hall effect data.

The same analysis was performed for $Cu_{2-x}Se$, and the results are shown in Figure 6.4. Again, the quality factor obtained from temperature-ramped resistivity data (0.29) is within 17% of that obtained with steady-state Hall data (0.35), showing that the scaled weighted mobility model is a good tool for estimating the viability of the material as a thermoelectric. It must be noted that the scaled effective mass curve in Figure 6.4 overestimates the data because it is based on steady-state Hall data, whereas the curve from the scaled SPB model without Hall data is based on a ramped resistivity measurement.

6.4 Low Thermal Conductivity

The low thermal conductivity of Cu_2S is particularly surprising because Cu_2S consists of relatively light elements [89]. Small, light elements generally make stronger, more covalent bonds than the heavier elements in the same family. Such strong bonds lead to stiffer elastic constants and higher

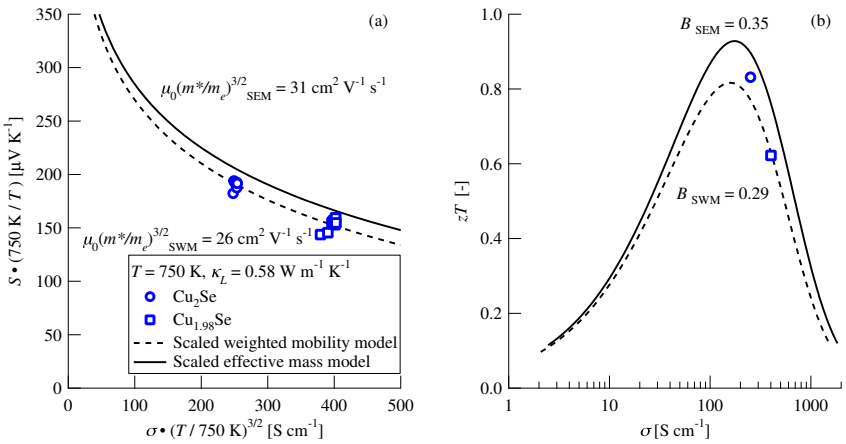

Figure 6.4: Despite differences between the fixed-temperature Hall data and the resistivity data taken during a temperature ramp, the scaled Seebeck and conductivity method yields a quality factor close to that obtained from Hall data.

speeds of sound. This in turn leads to higher thermal conductivity in both the thermal diffusion limited regime of a disordered solid (glass) as well as the acoustic phonon dominant regime typical of crystalline solids (κ_u in Table 6.1). Cu_2S remarkably has lower thermal conductivity than its heavier counterpart Cu_2Se, which can be traced, in part, to its lower average speed of sound. The longitudinal speed of sound v_l (and bulk modulus, B_T) in Cu_2S is actually higher than that of Cu_2Se, as one might have expected from the smaller and more covalent sulfide compared to the selenide. However the transverse phonons travel more slowly in Cu_2S than in Cu_2Se: the shear speed of sound v_s and bulk modulus G_T are remarkably lower in Cu_2S than in Cu_2Se. This leads to an overall reduction in average speed of sound (both arithmetic and geometric averages) and lower estimate for the minimum thermal conductivity (κ_{min}), which is the expected thermal conductivity in the diffusive limit of highly disordered, amorphous solids [91]. Clearly, the shear modes of Cu_2S, even in the crystalline low temperature γ phase, are extraordinarily soft.

As observed in Cu_2Se the liquid-like ionic motion also leads to lower than expected heat capacity as the modes can no longer store elastic energy. This reduction in heat capacity is even more pronounced in Cu_2S than in Cu_2Se, as shown in Figure 6.5. While Cu_2Se shows an essentially temperature independent C_p up to 800 K [16], the C_p of Cu_2S is clearly decreasing to below the Dulong-Petit value derived for solids with shear modes that store elastic energy. The reduced C_p in the β phase is consistent with the report by Gronvold and Westrum [92]. The low and decreasing C_V leads to low thermal conductivity due to its contribution to $\kappa_L \sim v_{avg} C_V l/3$ (l is phonon mean free path), but this may also be an indicator of extreme softening of shear modes that drastically reduces the transverse phonon velocity. The findings in Cu_2S also suggest that liquid-like materials may also possess inherently low speed of sound and high Grüneisen parameter, a measure of bond anharmonicity in the material (which also contributes to greater Umklapp scattering and therefore

lower κ_u).

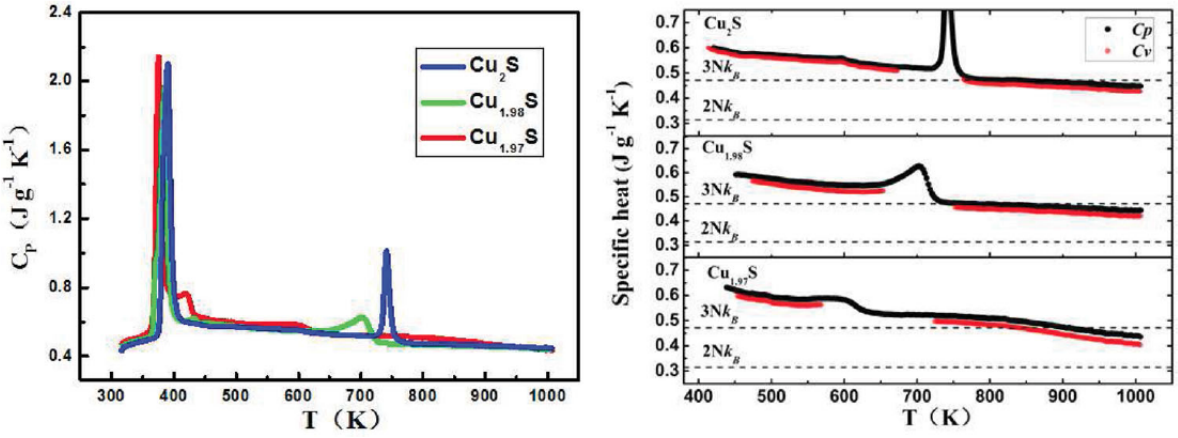

Figure 6.5: The decrease in heat capacity to below the $3Nk_B$ value is evidence for the softening of shear modes in $Cu_{2-x}S$.

The estimated lattice thermal conductivity of $Cu_{2-x}S$ is below even that expected for a glass or a liquid. The minimum thermal conductivity κ_{min} calculated from the high temperature limit of Cahill's formula [91] in Table 6.1 should give a good estimate for the lattice thermal conductivity when all of the phonons (transverse and longitudinal) are completely scattered (Equation 6.1). This is typically a good estimate not only for solid amorphous glasses but also liquids whose thermal conductivity does not differ significantly from that of glasses [93]. Some low dimensional structures, however, do show thermal conductivity significantly below κ_{min} that appears to be due to the reduction of the number of heat propagating modes, particularly shear modes [94]. If some shear modes (approximately half) are removed from Equation 6.1, the calculated κ_{min} values (Table 6.1) are close to the estimated κ_L values for $Cu_{2-x}S$ and $Cu_{2-x}Se$ (Table 6.2). If only the longitudinal modes contribute, $\kappa_{min,long}$ is calculated (Table 6.1). Thus the reduction in the heat capacity of the shear modes appears to reduce the lattice thermal conductivity to below that of a normal amorphous solid. The absence of shear modes is supported by heat capacity data (Figure 6.5), which show the heat capacity descending below the $3Nk_B$ limit.

$$\kappa_{min} = \frac{1}{2}\left(\frac{\pi}{6}\right)^{1/3} k_B V_{atom}^{-2/3} \left(2v_s + v_l\right) \tag{6.1}$$

In conclusion, we show that liquid-like copper sulfide $Cu_{2-x}S$ has exceptional thermal and electrical transport properties. $Cu_{2-x}S$ can be modeled as a heavily doped semiconductor with lower effective mass and greater deformation potential than Cu_2Se. The disordered copper ions in the liquid-like sublattice not only strongly scatter phonons, they also diminish the heat capacity of lattice vibrations much more clearly in $Cu_{2-x}S$ than in Cu_2Se. The lower lattice thermal conductivity observed in $Cu_{2-x}S$ than observed in Cu_2Se also is correlated to the extraordinarily low trans-

verse acoustic phonon velocity as well as anharmonicity as measured by Grüneisen parameter, both of which further lead to low thermal conductivity. As a result, the total thermal conductivity in $Cu_{2-x}S$ is less than 0.6 W m^{-1} K^{-1} in the whole temperature range, leading to a maximum zT value of 1.7 at 1000 K. We expect the discovery of high thermoelectric performance copper sulfides could attract great attention within the waste heat recovery industry due to their unique combination of elements that are low cost, nontoxic, and earth-abundant.

Chapter 7

Effective Medium Theory and Resistivity Tensor Measurements

7.1 Introduction

Great strides have been made in improving thermoelectric performance by combining solid phases. Microstructuring to scatter phonons while maintaining high carrier mobilities [95] is a proven method for reducing the lattice thermal conductivity [96]. The high potential for inclusions to improve the electronic properties of thermoelectrics by doping [97, 98], electron filtering [99], and composition modulation [6] has lead to values of the thermoelectric figure-of-merit zT greater than unity, approximately the value used in commercial modules.

The mechanisms described above use a second phase or microstructure to affect the performance of the matrix phase due to quantum mechanical or other nanometer-size effects on the transport properties. This is because the zT of a composite material cannot be improved by the combination of two phases in a parallel, series or arbitrary mixture which can be described by classical phenomena [39]. Secondary phases are also of concern because phase-pure synthesis of some materials is challenging, making measurement of the electronic properties of the target compound difficult [100]. Sometimes composites are discovered that have high thermoelectric performance despite containing impurities, such as $Ag_2Se_{0.5}Te_{0.5}$ (see Section 5.4, [22]), or that could have high performance in phase-pure form, but whose phase-pure properties are obscured by those of the impurity phase, such as Ag-doped Cu_2Se (see Section 4.2, [54, 43]). It would be useful to have a technique for determining zT in the matrix phase without investing the funding and labor needed to make a phase-pure sample.

Interpretation of transport measurements of multiphase materials is critical for thermoelectric

optimization and application; however, no one has demonstrated a method for separating the transport properties of each phase in a composite from measurements of the bulk material.

Exploring the transport properties of thermoelectric materials can be thought of as changing thermodynamic variables within the materials and observing the changes in the transport properties. Up to this chapter, those thermodynamic variables have been limited to the absolute temperature and the chemical potential (also called the Fermi level). The absolute temperature yields information about the band gap (Figure 5.3, [75]) and the scattering mechanism (Equations 3.5, 4.1, 4.2, [31]). The chemical potential determines the Hall carrier concentration and the Seebeck coefficient, the analysis of which is the starting point for the SPB model (Section 3.2). Making samples with different chemical potentials and measuring them at different temperatures has yielded the results in this thesis, but it is a time-consuming method. For materials in which multiple bands are suspected to contribute to conduction, even more samples must be made to resolve the multiband transport features. The magnetic field strength is also a thermodynamic variable, one that can be changed to reveal information about the band parameters in a single sample at a single temperature.

According to the equation of motion for a charge carrier in orthogonal electric and magnetic fields, a material with single free-electron band conduction will not exhibit magnetoresistance [101, 102], and the Hall coefficient will be linear with the magnetic field strength. However, if two such free electron bands contribute to conduction, the resistivity and Hall coefficient (or Hall resistivity) will be nonlinear with magnetic field strength [33]. The resulting curves of resistivity and Hall coefficient (or Hall resistivity) are determined by the conductivity and mobility of each band. We can use effective medium theory to extend the two-band picture to a two-phase picture.

In this work we seek to provide a method for extracting the conductivity and mobility of each phase in a composite from measurements of the in-line and Hall resistivity of the bulk, using effective medium theory. Effective medium theory can be used to derive expressions for two-phase transport properties of any kind, including the electrical conductivity [39, 103], Seebeck coefficient [39], and the thermal conductivity [104, 105], meaning that effective medium theory can be united with microstructure engineering to design electronically optimized, low lattice thermal conductivity thermoelectric materials. We take the first step toward such an optimization by applying Stroud's powerful coherent potential approximation [103] along with magnetic-field dependent resistivity measurements to determine the conductivity and mobility of each phase in a two-phase composite. Our approach does not include nanoscale effects, so it can also be used to distinguish between bulk and nanoscale contributions, or it can be used in conjunction with models of small-size properties, as some researchers have already done [104]. Because the model does not include nanoscale or quantum effects, some prior knowledge of the presence of these effects in the material is needed. This prior knowledge could include TEM images showing nanoscale interfaces, or information about band alignment between the phases. Once it is known whether these effects play a role in the material,

the model provides a baseline for quantifying their benefits.

This derivation yields quantitative correction terms that can be applied to analyze transport data. In many cases this method would give quantitative justification for use of a single phase approximation. In other cases this method will give a quantitative correction factor. The method also identifies the volume-fraction weighted Hall conductivity of the matrix phase and the magnetoresistance contribution of each phase as the critical scaling factors which ultimately determine what level of correction or even appropriateness a single phase transport model may have.

In general, the contribution of each phase in a composite to the magnetoresistance and to the Hall effect depends on its charge carrier mobility multiplied by the magnetic field strength. Because the dependence is nonlinear, we can use a magnetic field to distinguish the effect each phase has on electrical transport in a composite. $Cu_{1.97}Ag_{0.03}Se$ contains an impurity phase with a high mobility that exerts a disproportionate influence on the transport properties, providing us with a model system to show the viability of this approach. The synthesis details of $Cu_{1.97}Ag_{0.03}Se$ are given in Section 2.1.4.

X-ray diffraction data (Figure 2.3) show that this composition comprises two phases: the matrix with the crystal structure of Cu_2Se, and an impurity phase with the crystal structure of CuAgSe, which dissolves into the matrix around 390 K [43, 23]. The number of phases is confirmed by scanning electron microscopy, (Figure 7.1 inset), which shows the gray matrix phase and a light-colored impurity phase. The dark spots are voids; according to geometric density measurements the sample has only 3% porosity. $Cu_{1.97}Ag_{0.03}Se$ displays unusual electrical properties below its superionic phase transition at 407 K (Figure 7.1). It has a Seebeck coefficient greater than zero, indicating holes as the majority carriers, but a Hall coefficient R_H less than zero, indicating electrons have a strong influence on the electrical conductivity in this composite. This opposite behavior is rare in materials, but occurs in some elemental metals like Li, Cu, Ag, and Au [106], and in some semiconductors such as $AgSbTe_2$ and in PbTe-PbS alloys [107]. In these cases, band structure effects can explain these properties [108]. However, in the case of $Cu_{1.97}Ag_{0.03}Se$, R_H becomes positive as soon as the impurity phase dissolves, suggesting that only the impurity phase is n-type with an electron mobility much greater than that of the matrix. Indeed, the CuAgSe impurity phase is n-type and has high mobility, around 2000 $cm^2\ V^{-1}\ s^{-1}$ at room temperature, nearly two orders of magnitude greater than that of Cu_2Se, the apparent matrix phase [54].

The lack of a fully confirmed crystal structure for the highly Cu-disordered Cu_2Se [109] and the conflicting carrier types make $Cu_{1.97}Ag_{0.03}Se$ a challenging material on which to develop an electrical transport model. The disparity of the electron mobility values between its phases makes it a perfect model system for the combination of magnetic-field dependent resistivity measurements and effective medium theory. This technique allows us to extract the resistivity tensor of each phase, the results of which we show below.

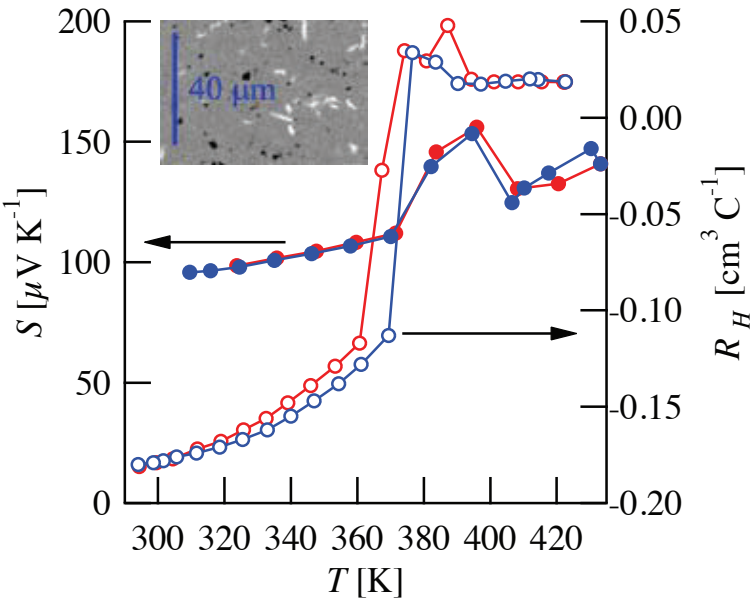

Figure 7.1: Hall coefficient R_H (open symbols) and Seebeck coefficient S (closed symbols) data below the phase transition in $Cu_{1.97}Ag_{0.03}Se$. The positive Seebeck coefficients indicate holes and the negative Hall coefficient indicates electrons as the majority carriers, showing the conflicting properties in this composite. Heating data are shown in red and cooling data in blue. The inset is an SEM micrograph of the material at room temperature.

7.2 Resistivity Tensor Measurement Methods

The data in Figure 7.1 were taken on a custom-built Hall effect system with van der Pauw geometry and a magnetic field of +/- 2 T [30]. The data in Figure 7.6 were taken on a Quantum Design Physical Property Measurement System (PPMS) with its stronger magnet and more sensitive measurements. The in-line resistivity ρ_{xx} and the Hall resistivity ρ_{yx} were measured by the four-point method with alternating current using the Electrical Transport Option at a range of magnetic field strengths between 14 T and -14 T. Electrical leads were fixed to the sample using silver epoxy. A current of 10 mA and a frequency of 3 Hz were used to measure ρ_{xx}. A current of 4 mA and a frequency of 15 Hz were used to measure ρ_{yx}. These parameters yielded the smallest phase angles between the input current and output voltage for each measurement.

The measurements of ρ_{yx} are offset by a term that increases with magnetic field due to imperfect alignment of the voltage leads. Therefore, the ρ_{yx} data shown in this work were obtained by the following correction [110]:

$$\rho_{yx,data}(B) = \rho_{yx,measured}(B) - \rho_{yx,data}(0)\frac{\rho_{xx,measured}(B)}{\rho_{xx,measured}(0)} \tag{7.1}$$

The effective medium model was fitted to the data with a MATLAB script that minimized the differences between the model values and the data values in both ρ_{xx} and ρ_{yx} and between their

derivatives as a function of magnetic field strength. The matrix phase was modeled as a group of spherical crystallites. The impurity phase was modeled as a group of prolate spheroidal crystallites, with the ratio of the minor axis to the major axis set at 0.1. This number was determined from SEM micrographs (Figure 7.1 inset) showing the impurity phase. The effect of the 3% porosity on the transport measurements was estimated to be a 2% increase in ρ_{xx} and a 3% increase in ρ_{yx} using the effective medium model and treating the voids as spheres with zero conductivity. We therefore neglect the effect of the porosity on the transport measurements.

7.3 Effective Medium Theory

The simplest model for a two-phase composite is one that treats the two phases as parallel or series conductors. For example, for parallel conductors the in-line, zero magnetic field conductivity of this composite, $\sigma_{0,xx}$ is the volume-fraction weighted sum of the component in-line conductivity values at zero field, given by Equation 7.2:

$$\sigma_{0,xx} = \sum_{i=1}^{2} f_i \sigma_{0,i} \tag{7.2}$$

f_i is the volume fraction of phase i, and $\sigma_{0,i}$ is the in-line conductivity at zero magnetic field. The effective Hall coefficient $R_{H,e}$ is given by a weighted sum of each component R_H, $R_{H,i}$ [111]:

$$R_{H,e} = \frac{\sum_{i=1}^{2} \left(f_i \sigma_{0,i}\right)^2 R_{H,i}}{\left(\sum_{i=1}^{2} f_i \sigma_{0,i}\right)^2} \tag{7.3}$$

However, these expressions are only valid at low magnetic field strength, and provide no means to separate the contributions of each phase based on their responses to the magnetic field.

Stroud developed an effective medium model for predicting the resistivity tensor of a composite made up of multiple solid phases [103]. Each constituent is represented by a conductivity tensor $\boldsymbol{\sigma}_i$, given by Equation 7.4 [112]. Tensors are represented by bold symbols. $\sigma_{0,i}$ is the electrical conductivity at zero field, B is the magnetic field strength, and μ_i is the electron mobility. The magnetic field always points in the z-direction. In our measurement geometry, the electric field $\mathscr{E}$ is always perpendicular to B. The longitudinal magnetoresistance is zero, since that phenomenon is proportional to $\mathscr{E} \cdot B$ for free electron conduction [102], so $\sigma_{i,zz}$ does not depend on B. In this work we assume that the materials are "isotropic" in the sense that in each phase σ_{xx} is equal to σ_{yy}. The anisotropy in this tensor is due only to the strength of the magnetic field. At zero field, the diagonal terms are all equal, and the off-diagonal terms are zero. At finite magnetic field values, the upper left and center diagonal terms will be different from the lower right diagonal term because the magnetic field points in the z-direction. At finite magnetic field values, only the xy and yx off-diagonal terms

will be non-zero, again because the magnetic field always points in the z-direction.

$$\boldsymbol{\sigma}_i = \sigma_{0,i} \begin{bmatrix} \dfrac{1}{1+(\mu_i B)^2} & \dfrac{\mu_i B}{1+(\mu_i B)^2} & 0 \\ \dfrac{-\mu_i B}{1+(\mu_i B)^2} & \dfrac{1}{1+(\mu_i B)^2} & 0 \\ 0 & 0 & 1 \end{bmatrix} \tag{7.4}$$

The model yields an effective resistivity tensor given by Equation 7.5. The inverse of any conductivity tensor is a resistivity tensor, which is useful because our measurements are of resistivity values. $\boldsymbol{\sigma}_i$ and $\boldsymbol{\sigma}_e$ in general are not isotropic, as evidenced by the different values of ρ_{xx} and ρ_{yx} in Figure 7.6. However, the behavior of $\boldsymbol{\sigma}_i$ with B is completely specified by just two parameters, $\sigma_{0,i}$ and μ_i. Electronic bands in a phase are represented by tensors with the form of Equation 7.4, and $\boldsymbol{\sigma}_i$ for a multiband material is the sum of these tensors.

$$\boldsymbol{\sigma}_e = \begin{bmatrix} \sigma_{e,xx} & \sigma_{e,xy} & 0 \\ -\sigma_{e,xy} & \sigma_{e,xx} & 0 \\ 0 & 0 & \sigma_{e,zz} \end{bmatrix} \tag{7.5}$$

Stroud solved the electrostatic equations to yield the coherent potential approximation, given by Equation 7.6 [103]. This equation expresses the effective conductivity tensor as a volume-fraction weighted sum of the conductivity tensors of the constituent phases. Since Equation 7.6 is a tensor equation, it contains two independent equations that can be numerically solved for $\sigma_{e,xx}$ and $\sigma_{e,xy}$, with $\sigma_{0,i}$ and μ_i as fitting parameters.

$$\mathbf{0} = \sum_{i=1}^{2} f_i \left(\boldsymbol{\sigma}_i - \boldsymbol{\sigma}_e\right) \left(\boldsymbol{I} - \left(\boldsymbol{\sigma}_i - \boldsymbol{\sigma}_e\right) \boldsymbol{\Gamma}_i\right)^{-1} \tag{7.6}$$

The depolarization tensor $\boldsymbol{\Gamma}_i$ relates the electric field inside a crystallite of phase i to that outside it [113], and therefore depends on the shape of the crystallite and on the anisotropy of $\boldsymbol{\sigma}_e$ [103]. $\boldsymbol{I}$ is the identity tensor. $\boldsymbol{\Gamma}_i$ is given by Equaton 7.7. S' is the surface of the crystallite, $\vec{x}$ is a position vector, $\vec{x}'$ is a position vector from the center of the crystallite to the surface, and $\vec{n}'$ is a surface normal unit vector, and x' is a component of $\vec{x}'$. $G\left(\vec{x}-\vec{x}'\right)$ is the Green's function used to solve the electrostatic equation in the material [103]; it is given by Equation 7.8.

$$\boldsymbol{\Gamma}_i = -\oint_{S'} \nabla G\left(\vec{x}-\vec{x}'\right) \vec{n}' d^2x' \tag{7.7}$$

$$G\left(\vec{x}-\vec{x}'\right) = \frac{1}{4\pi\sigma_{e,xx}\sigma_{e,zz}^{1/2}} \left(\frac{(x-x')^2}{\sigma_{e,xx}} + \frac{(y-y')^2}{\sigma_{e,xx}} + \frac{(z-z')^2}{\sigma_{e,zz}} \right)^{-1/2} \tag{7.8}$$

Equation 7.7 is the most general equation for $\mathbf{\Gamma}_i$. In this study we will take the matrix phase to be a collection of spheres of different sizes such that no gaps exist between the spheres. Equation 7.7 depends only on the shape of the crystallites and not on their absolute size. We will take the impurity phase crystallites to be prolate spheroidal in shape, which is supported by the SEM image in Figure 7.1. When all the phases in a composite are spheres or spheroids, the depolarization tensor takes the form of Equation 7.9.

$$\mathbf{\Gamma}_i = \begin{bmatrix} \Gamma_{i,xx} & 0 & 0 \\ 0 & \Gamma_{i,yy} & 0 \\ 0 & 0 & \Gamma_{i,zz} \end{bmatrix} \tag{7.9}$$

$\Gamma_{i,zz}$ for a prolate spheroid is given by Equation 7.10. ν_a is the aspect ratio of the prolate spheroid, i.e. the ratio of the length its minor axis to that of its major axis. g, given by Equation 7.11 is referred to in this work as the anisotropy factor. It is a ratio of the shape anisotropy of crystallite i to the electrical anisotropy of the composite. Neither of these quantities are related to crystal structure anisotropy. ν_a is a ratio of the shortest dimension of the crystallite to its longest, and the denominator of g is a ratio of the conductivity of the composite at magnetic field strength B to that at zero field.

$$\Gamma_{i,zz} = -\frac{1}{\sigma_{e,zz}} \frac{g}{1-g} \left(1 - \frac{\arctan\sqrt{g-1}}{\sqrt{g-1}} \right) \tag{7.10}$$

$$g = \frac{\nu_a^2}{\sigma_{e,xx}/\sigma_{e,zz}} \tag{7.11}$$

$\Gamma_{i,xx}$ is given by Equation 7.12.

$$\Gamma_{i,xx} = \frac{1}{2\sigma_{e,xx}} \left(1 - \Gamma_{i,zz}\sigma_{e,zz} \right) \tag{7.12}$$

To first order, the volume-fraction weighted Hall conductivity of a single phase $\sigma_{i,xy}$ is $f_i\sigma_{0,i}\mu_i B$, where f_i is the volume fraction of phase i. If the fractional contribution of the matrix phase to the Hall conductivity, $|f_1\sigma_{0,1}\mu_1| \ / \ \sum |f_i\sigma_{0,i}\mu_i|$ is less than unity, and at least one of the phases has a magnetoresistance contribution $\mu_i B$ of order one, the impurity phase will make a measurable contribution to both the in-line and Hall resistivity, and both quantities will be nonlinear as a function of magnetic field, providing data from which the individual conductivity and mobility values can be extracted.

7.4 Sensitivity Analysis

Before we discuss the results of applying the effective medium model to the resistivity tensor data, we will perform a sensitivity analysis on the model, i.e., we will determine how accurately it yields the conductivity and mobility of each phase.

The sensitivity of the model to the aspect ratio ν_a of the prolate spheroidal impurity phase was explored. The aspect ratio was varied from 0.1 (the value estimated from SEM images) to 0.2 and 0.05 (Figure 7.2). These curves show that changing ν_a by a factor of 2 changes the model values of ρ_{yx} by a maximum of 9% and has a negligible effect on ρ_{xx}. The insensitivity of the model to ν_a is fortunate for the purpose of extracting electrical properties from each phase because the aspect ratio must be estimated from the average size of the crystallites, making it difficult to obtain an accurate estimate of ν_a. The model is insensitive to ν_a because of the low aspect ratio (0.1) of the impurity crystallites. Looking at a plot of $\Gamma_{i,jj}$ (Equations 7.10 through 7.12 versus g (Equation 7.11), shown in Figure 7.3, it is clear that in the low ν_a portion of the $\Gamma_{i,jj}$ curves $\Gamma_{i,jj}$ does not change much with g.

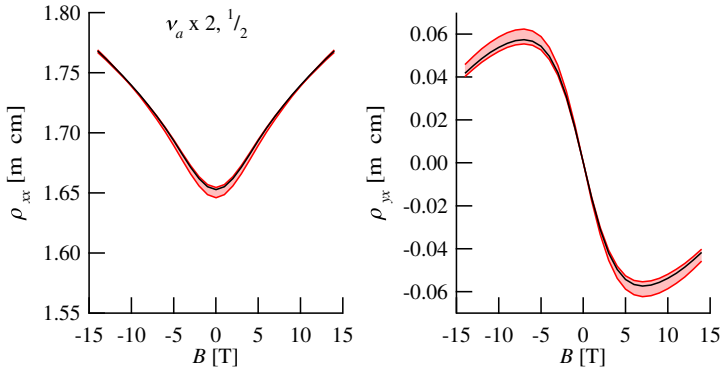

Figure 7.2: Effect of changing the impurity phase aspect ratio ν_a.

We varied the conductivity and mobility of each phase and band by 10% from the fit values while keeping the other parameters constant, except for $\mu_{impurity,2}$, which was varied by 20%. This was done to the fit at 300 K. The results for ρ_{xx} and ρ_{yx} are shown in Figures 7.4 and 7.5, respectively, with the original fit as a black line and the change to the curve resulting from changing a parameter by +/- 10% shown as a red band. Figures 7.4 and 7.5 show that the matrix phase conductivity $\sigma_{0,matrix}$ has the most influence on ρ_{xx} and ρ_{yx}. Changing $\sigma_{0,matrix}$ by 10% creates changes on the order of 10% in ρ_{xx} and 100% in ρ_{yx}. The conductivity of Band 1 in the impurity phase, $\sigma_{0,impurity,1}$ has a similar influence on ρ_{yx}, but creates changes of only 3% in ρ_{xx}. Varying $\sigma_{0,impurity,2}$ by 10% causes ρ_{yx} to change by about 7%, which is detectable in the PPMS. The sensitivity analysis shows that the conductivity values can be determined within 10%. Varying the mobility values by 10% moves the fit curves of ρ_{xx} by less than 1%. However, 10% variation in the mobility of the matrix

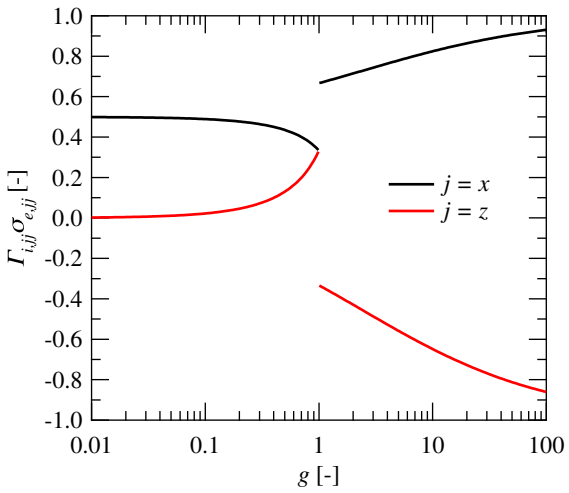

Figure 7.3: Depolarization tensor elements $\Gamma_{i,jj}$ versus the anisotropy factor g (Equation 7.11).

and of Band 1 in the impurity phase creates changes of about 8% in ρ_{yx}. The mobility value of Band 2 in the impurity phase is more difficult to determine because its contributions to ρ_{xx} and ρ_{yx} are smaller (Equation S4). Varying $\mu_{impurity,2}$ by 20% affects the ρ_{yx} fit curves by about 10% at most. Therefore, the model can determine the mobility of minority bands to within 20%, where by minority bands we mean those with conductivity values of order 10% of the other bands in the same phase.

7.5 Results and Discussion

A representative measurement of the in-line resistivity ρ_{xx} and the Hall resistivity ρ_{yx} at 300 K, including the transport model, is shown in Figure 7.6.

The in-line resistivity ρ_{xx} rises with positive and negative magnetic field, but its rate of change with B decreases with increasing B. This is referred to as saturating behavior. This is because each phase's contribution to ρ_{xx} is weighted by $1/\left(1+(\mu_i B)^2\right)$, meaning that as B increases, the contribution of the high mobility phase decreases, causing the rate of change of ρ_{xx} with B to decrease. The Hall resistivity ρ_{yx} exhibits linear behavior from 0 T to about +/- 4 T. Again, this is because of the way ρ_{yx} is weighted with B. Each phase's contribution is weighted by $\mu_i B/\left(1+(\mu_i B)^2\right)$. At low values of B, the Hall resistivity will be dominated by the high mobility phase. As B increases, the high mobility phase will continue to dominate, but its contribution will decrease as the denominator $\left(1+(\mu_i B)^2\right)$ increases, leading to decreasing values of ρ_{yx} with B. Note, however, that if the Hall resistivity ρ_{yx} is converted to a Hall coefficient R_H according to $R_H = \rho_{yx}$ / B, R_H stays negative across the entire range of B values, meaning that the n-type impurity phase is the majority contributor to the Hall effect in this material.

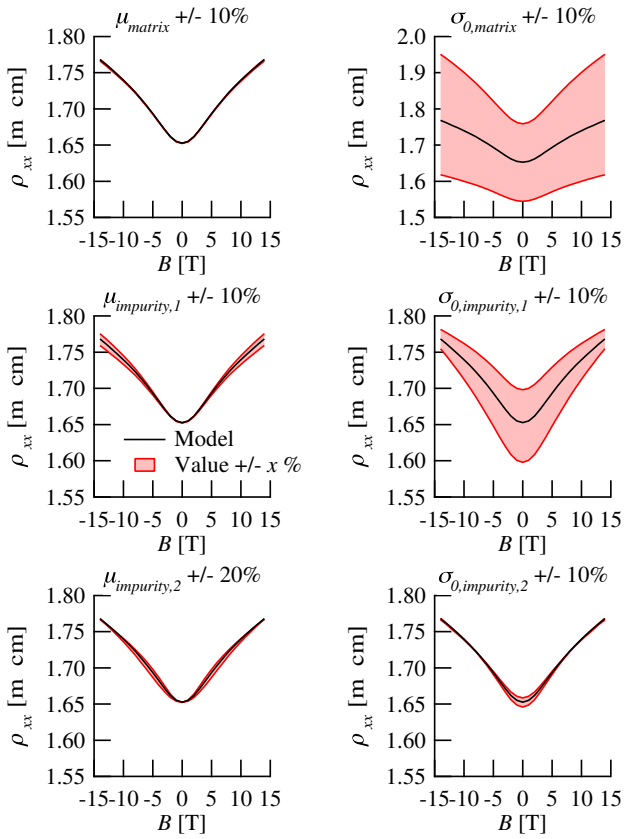

Figure 7.4: Sensitivity analysis of ρ_{xx}.

Each electronic band in each phase is characterized by a zero-field conductivity $\sigma_{0,i}$ and an electron mobility μ_i. We modeled the matrix phase as a single-band material, and the impurity phase as a two-band material, for a total of six free parameters.

The estimates for $\sigma_{0,i}$ are shown in Table 7.1 along with error bounds from the sensitivity analysis. Ishiwata, et al used two conduction bands to model the resistivity tensor components of CuAgSe [56], a strategy suggested by the nonlinear behavior of ρ_{xx} and ρ_{yx} with magnetic field observed in that work. For this reason, we have adopted the same strategy. The total conductivity of the impurity phase differs by up to 20% of that of CuAgSe. This suggests that while the impurity phase has the crystal structure of CuAgSe [23], the impurity phase has a slightly different composition.

Table 7.1: Zero-field conductivity of $Cu_{1.97}Ag_{0.03}Se$ as a function of temperature.

$\sigma_{0,i}$ [S cm^{-1}]	300 K	333 K	350 K	366 K	380 K
Impurity Phase, Band 1	1169 ± 120	1101 ± 110	1006 ± 100	985 ± 100	846 ± 85
Impurity Phase, Band 2	147 ± 15	120 ± 12	148 ± 15	83 ± 8	34 ± 3
Impurity Phase, total	1316 ± 130	1221 ± 120	1154 ± 120	1067 ± 110	880 ± 88
CuAgSe [56]	1305	1332	1208	1132	1052
Matrix	547 ± 55	517 ± 52	492 ± 49	458 ± 46	309 ± 31
Cu_2Se [43]	853	768	731	650	497

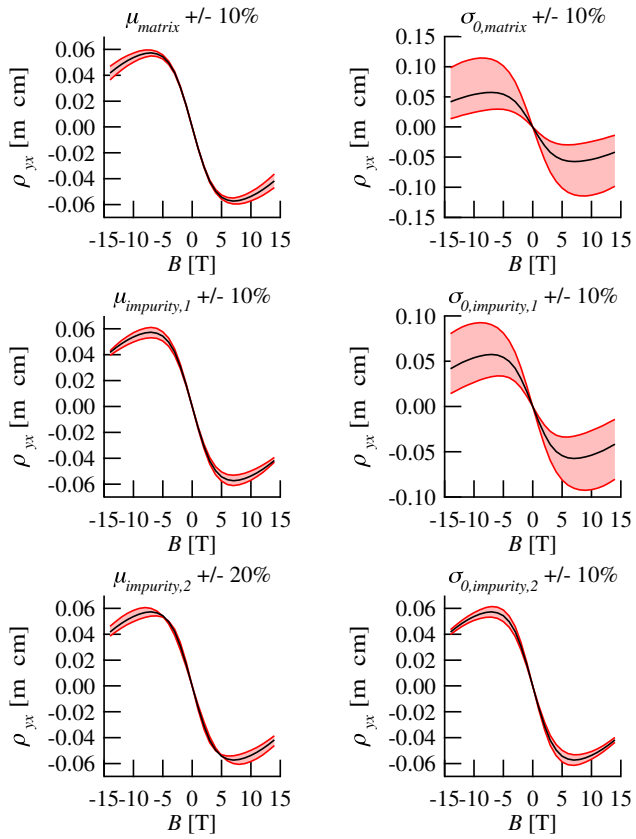

Figure 7.5: Sensitivity analysis of ρ_{yx}.

The estimates for the carrier mobility of each phase are shown in Table 7.2 along with error bounds from the sensitivity analysis. The units of 10^{-4} T^{-1} are numerically equal to units of cm^2 V^{-1} s^{-1}, but it is more instructive to use inverse units of magnetic field strength to illustrate that the carrier mobility is a weighting factor for the electrical conductivity of each phase and each band. The $\mu_i B / \left(1 + (\mu_i B)^2\right)$ term reaches a maximum when $\mu_i B$ equals one, which for the high mobility band of the impurity phase is when $|B|$ is between 6 and 9 T, depending on temperature. At this value of $|B|$, ρ_{yx} reaches an extremum, and ρ_{xx} reaches an inflection point as the influence of the second phase declines due to saturation (see Figure 7.6).

Table 7.2: Single band mobility of $Cu_{1.97}Ag_{0.03}Se$ as a function of temperature.

μ_i [10^{-4} T^{-1}]	300 K	333 K	350 K	366 K	380 K
Impurity Phase, Band 1	-164 ± 16	-167 ± 17	-149 ± 15	-138 ± 14	-50 ± 5
Impurity Phase, Band 2	-1458 ± 300	-1504 ± 300	-1090 ± 220	-1235 ± 240	-1178 ± 240
CuAgSe [56]	-2191	-	-	-	-
Matrix	24 ± 2	22 ± 2	24 ± 2	25 ± 3	50 ± 5
Cu_2Se [43]	13	12	11	11	10

Looking at Table 7.1 and Table 7.2 reveals the cause of the nonlinear Hall effect in this material.

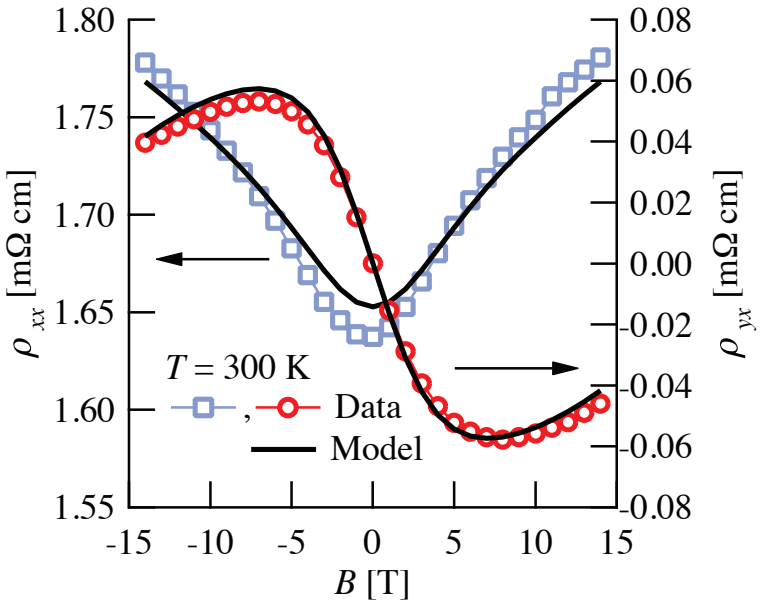

Figure 7.6: Resistivity measurements as a function of magnetic field B at 300 K. A composite of two phases guarantees nonlinear behavior in the magnetoresistance ρ_{xx} (open symbols) and the Hall effect ρ_{yx} (open symbols) due to the differences in the weighting of each phase by its electron mobility.

At all temperatures studied, the material contains at least one band with a great enough mobility such that $\mu_i B$ is of order one; the contribution of the matrix phase to the Hall effect $|f_1\sigma_{0,1}\mu_1|$ / $\sum|f_i\sigma_{0,i}\mu_i|$ is at most 85% and is as low as 50%. These two facts guarantee that the impurity phase will have an enormous influence on the Hall effect in the material, despite its making up less than 3% of the sample volume.

The electron mobility of the high-mobility band in the impurity phase is less than that reported for pure CuAgSe (Table 7.2). This is because the impurity phase has a greater electron concentration that does pure CuAgSe (Figure 7.7), which leads to a lower electron mobility when electron scattering is dominated by acoustic phonons [1].

Looking at the fit parameters together and as functions of temperature indicates that metal atoms move between the matrix and impurity phases. Computing the Hall carrier concentration of the matrix with the relation $n_H = \sigma$ / $e\mu$, where e is the elementary charge, and for the impurity phase with Equation 7.13 (adapted from the equation for R_H [76] by the relation $R_H = 1$ / $n_H e$), we see that the carrier concentration of the matrix is reduced compared to that of Cu_2Se, and that of the impurity phase is increased relative to CuAgSe (Figure 7.7).

$$n_H = \frac{(\sigma_1 + \sigma_2)^2}{e\,(\sigma_1\mu_1 + \sigma_2\mu_2)} \tag{7.13}$$

In the matrix, this must be due to Ag dissolving in the lattice. This is supported by X-ray

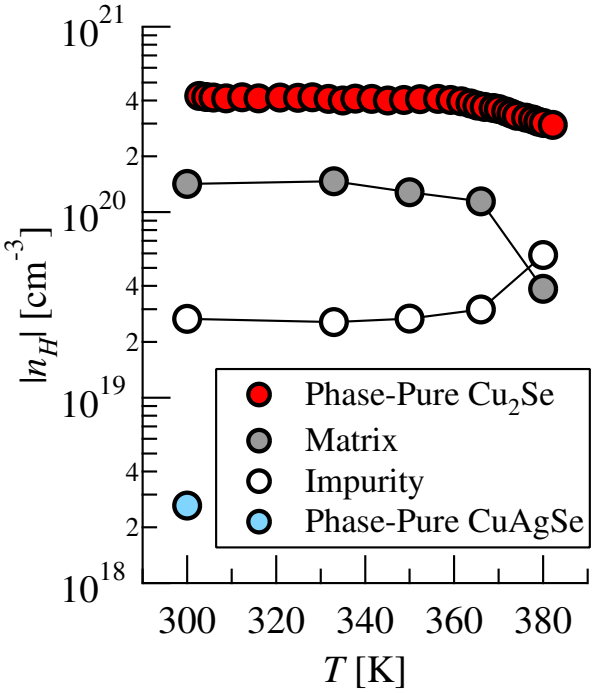

Figure 7.7: Hall carrier concentrations measured on pure Cu_2Se [43] and CuAgSe [56] and extracted from the model for the matrix and impurity phases.

diffraction by Brown et al [43] in which the reflections of $Cu_{1.97}Ag_{0.03}Se$ are shifted to smaller values of 2θ, indicating a larger lattice, which is consistent with the larger Ag cations located on vacant Cu sites [114]. Ordinarily these vacant sites create holes in Cu_2Se; an Ag atom on such a site donates an electron and reduces the number of positive charge carriers. Ag has been shown to reduce the carrier concentration in Cu_2Se [23], further supporting the idea that the matrix is Ag-doped Cu_2Se. In general, because the impurity phase dissolves into the matrix at higher temperatures, slightly different values of the cation ratios are not surprising.

The matrix phase and Cu_2Se both show a gradual decline of carrier concentration with temperature, but between 366 K and 380 K the carrier concentration of the matrix drops more sharply than does the carrier concentration of Cu_2Se. In this temperature range, Ag becomes more soluble in the matrix. The introduction of more Ag into the matrix fills more holes in the valence band of the matrix, reducing the carrier concentration. This is consistent with the jump in the matrix phase mobility, as the mobility tends to increase as the carrier concentration decreases.

The increase in the Hall carrier concentration of the impurity phase relative to CuAgSe could be due to an elevated cation to anion ratio. The dependence of the Hall carrier concentration of the impurity phase on temperature is more complicated because of the mobility-dependent contribution of each band. It is difficult to distinguish from the model parameters in Tables 7.1 and 7.2 the effects of temperature, mass exchange between the phases, and the changing energy difference between the

two bands. However, Figure 7.7 shows that the Hall carrier concentration of the impurity phase gradually rises and then jumps between 366 K and 380 K. Between these two temperatures, the conductivity of Band 1 drops much less than does the conductivity of Band 2 (Table 7.2). This means that the carrier concentration will be more influenced by Band 1, the band containing more carriers, and that the overall Hall carrier concentration will increase.

7.6 Conclusions

The classical influence of an impurity phase on the resistivity tensor of $Cu_{1.97}Ag_{0.03}Se$ and the interest in using impurity phases to create beneficial quantum effects in thermoelectrics drove us to introduce effective medium theory as a tool for optimizing phase-segregated thermoelectrics. We have shown that useful information on each band in each phase can be gathered by measuring the independent components of the resistivity tensor at high magnetic fields. In combination with X-ray diffraction and classic thermoelectric characterization techniques, we present a powerful tool to model and understand multiphase behavior in semiconductors, in order to optimize materials compositions for high figure-of-merit thermoelectrics, such as composites of Sb_2Te_3 and PbTe [115], Ag_2Te and PbTe [98], In_2Te_3 and Bi_2Te_3 [116], or $AgSbTe_2$ with nanodot inclusions [6], as well as to quantify the negative effects of impurities.

Bibliography

[1] A. H. Wilson. *The Theory of Metals*. The Syndics of the Cambridge University Press, 1958.

[2] A. D. LaLonde, Y. Pei, H. Wang, and G. J. Snyder. Lead telluride alloy thermoelectrics. *Materials Today*, 14(11):526–532, 2011.

[3] L. E. Bell. Cooling, Heating, Generating Power, and Recovering Waste Heat with Thermoelectric Systems. *Science*, 321:1457–1461, 2008.

[4] C. B. Vining. An inconvenient truth about thermoelectrics. *Nature Materials*, 8(2):83–85, 2009.

[5] Frank Kreith. *Radiation Heat Transfer for Spacecraft and Solar Power Plant Design*. International Textbook Company, 1962.

[6] K. F. Hsu, S. Loo, F. Guo, W. Chen, J. S. Dyck, C. Uher, T. Hogan, E. K. Polychroniadis, and M. G. Kanatzidis. Cubic $AgPb_mSbTe_{2+m}$: Bulk Thermoelectric Materials with High Figure of Merit. *Science*, 303:818–821, 2004.

[7] A. J. Minnich, M. S. Dresselhaus, Z. F. Ren, and G. Chen. Bulk nanostructured thermoelectric materials: current research bulk nanostructured thermoelectric materials: current research and future prospects. *Energy and Environmental Science*, 2(5):466–479, 2009.

[8] H. Wang, A. D. LaLonde, Y. Z. Pei, and G. J. Snyder. The criteria for beneficial disorder in thermoelectric solid solutions. *Advanced Functional Materials*, 23(12):1586–1596, 2013.

[9] G. J. Snyder and E. S. Toberer. Complex thermoelectric materials. *Nature Materials*, 7(2):105–114, 2008.

[10] J. P. Heremans, B. Wiendlocha, and A. M. Chamoire. Resonant levels in bulk thermoelectric semiconductors. *Energy and Environmental Science*, 5(2):5510–5530, 2012.

[11] Y. Z. Pei, X. Y. Shi, A. D. LaLonde, H. Wang, L. D. Chen, and G. J. Snyder. Convergence of electronic bands for high performance bulk thermoelectrics. *Nature*, 473(7345):66–69, 2011.

[12] J. M. O. Zide, D. Vashaee, Z. X. Bian, G. Zeng, J. E. Bowers, A. Shakouri, and A. C. Gossard. Demonstration of electron filtering to increase the Seebeck coefficient in $In_{0.53}Ga_{0.47}As/In_{0.53}Ga_{0.28}Al_{0.19}As$ superlattices. *Physical Review B*, 74(20):205335, 2006.

[13] E. A. Skrabek and D. S. Trimmer. *Thermoelectrics Handbook*, chapter 22. CRC Press LLC, Boca Raton, 1995.

[14] H. Scherrer and S. Scherrer. *Thermoelectrics Handbook*, chapter 19. CRC Press LLC, Boca Raton, 1995.

[15] Y. Y. Gurevich and A. K. Ivanov-Shits. *Semiconductors and Semimetals*, volume 26, chapter Semiconductor Properties of Superionic Materials. Academic Press, 1988.

[16] H. Liu, X. Shi, F. Xu, L. Zhang, W. Zhang, L. Chen, Q. Li, C. Uher, T. Day, and G. J. Snyder. Copper ion liquid-like thermoelectrics. *Nature Materials*, 11(5):422–425, 2012.

[17] Y. He, T. Day, T. S. Zhang, H. L. Liu, X. Shi, L. D. Chen, and G. J. Snyder. High thermoelectric performance in non-toxic earth-abundant copper sulfide. *Advanced Materials*, 26(23):3974–3978, 2014.

[18] F. Gascoin and A. Maignan. Order-Disorder Transition in $AgCrSe_2$: A New Route to Efficient Thermoelectrics. *Chemistry of Materials*, 23(10):2510–2513, 2011.

[19] M. Ferhat and J. Nagao. Thermoelectric and transport properties of β-Ag_2Se compounds. *Journal of Applied Physics*, 88(2):813–816, 2000.

[20] F. Aliev, M. Jafarov, and V. Eminova. Thermoelectric Figure of Merit of Ag_2Se with Ag and Se Excess. *Atomic Structure and Nonelectronic Properties of Semiconductors*, 43(8):1013–1015, 2009.

[21] T. Day, F. Drymiotis, T. S. Zhang, D. Rhodes, X. Shi, L. D. Chen, and G. J. Snyder. Evaluating the potential for high thermoelectric efficiency of silver selenide. *Journal of Materials Chemistry C*, 1(45):7568–7573, 2013.

[22] F. Drymiotis, T. Day, D. R. Brown, N. A. Heinz, and G. J. Snyder. Enhanced thermoelectric performance in the very low thermal conductivity $Ag_2Se_{0.5}Te_{0.5}$. *APL Materials*, 103(14):143906, 2013.

[23] T. W. Day, K. A. Borup, T. S. Zhang, F. Drymiotis, D. R. Brown, X. Shi, L. D. Chen, B. B. Iversen, and G. J. Snyder. High-temperature thermoelectric properties of $Cu_{1.97}Ag_{0.03}Se_{1+y}$. *Materials for Renewable and Sustainable Energy*, 3(2):26, 2014.

[24] G. A. Slack. *Thermoelectrics Handbook*, chapter 34. CRC Press LLC, Boca Raton, 1995.

[25] A. D. LaLonde, T. Ikeda, and G. Jeffrey Snyder. Rapid consolidation of powdered materials by induction hot pressing. *Review of Scientific Instruments*, 82(2):025104, 2011.

[26] T. Sakuma, K. Iida, K. Honma, and H. Okazaki. X-Ray Diffraction Study on a Superionic Conductor: α-Ag_2Se. *Journal of the Physical Society of Japan*, 43(2):538–543, 1977.

[27] R. D. Heyding and R. M. Murray. Queen's University, Kingston, Ontario, Canada. private communication, 1974.

[28] H. T. Evans. The crystal structures of low chalcocite and djurleite. *Zeitschrift fur Kristallographie*, 150(1):299–320, 1979.

[29] S. Iwanaga, E. S. Toberer, A. D. LaLonde, and G. J. Snyder. A high temperature apparatus for measurement of the Seebeck coefficient. *Review of Scientific Instruments*, 82(6):063905, 2011.

[30] K. A. Borup, E. S. Toberer, L. D. Zoltan, G. Nakatsukasa, M. Errico, J. P. Fleurial, B. B. Iversen, and G. J. Snyder. Measurement of the electrical resistivity and hall coefficient at high temperatures. *Review of Scientific Instruments*, 83(12):123902, 2012.

[31] V. I. Fistul. *Heavily Doped Semiconductors*. Plenum Press, 1969.

[32] D. Chattopadhyay and H. J. Queisser. Electron scattering by ionized impurities in semiconductors. *Reviews of Modern Physics*, 53(4):745–768, 1981.

[33] N. W. Ashcroft and N. David Mermin. *Solid State Physics*. Brooks/Cole Thomson Learning, 1976.

[34] E. O. Kane. Energy band structure in p-type germanium and silicon. *Journal of Physics and Chemistry of Solids*, 1(1):82–99, 1956.

[35] A. A. Abrikosov. Quantum magnetoresistance. *Physical Review B*, 58(5):2788–2794, 1998.

[36] A. F. Ioffe. *Physics of Semiconductors*. Academic, New York, 1960.

[37] R. P. Chasmar and R. Stratton. The thermoelectric figure of merit and the thermoelectric figure of merit and its relation to thermoelectric generators. *Journal of electronics and control*, 7(1):52–72, 1959.

[38] T. C. Harman and J. M. Honig. *Thermoelectric and Thermomagnetic Effects and Applications*. McGraw-Hill, New York, 1967.

[39] D. J. Bergman and O. Levy. Thermoelectric properties of a composite medium. *Journal of Applied Physics*, 70(11):6821–6833, 1991.

[40] H. Wang, G. J. Snyder, Y. Pei, and A. D. LaLonde. *Thermoelectric Nanomaterials*, chapter 1. Springer Series in Materials Science. Springer, 2013.

[41] J. Bardeen and W. Shockley. Deformation potentials and mobilities in non-polar crystals. *Physical Review*, 80(1):72–80, 1950.

[42] G. P. Sorokin, Y. M. Papshev, and P. T. Oush. Photoconductivity of Cu_2S, Cu_2Se, and Cu_2Te. *Soviet Physics Solid State*, 7(7):1810–1811, 1966.

[43] D. R. Brown, T. Day, K. A. Borup, S. Christensen, B. B. Iversen, and G. J. Snyder. Phase transition enhanced thermoelectric figure-of-merit in copper chalcogenides. *APL Materials*, 1(5):052107, 2013.

[44] D. R. Brown, T. Day, T. Caillat, and G. J. Snyder. Chemical Stability of $(Ag,Cu)_2Se$: a Historical Overview. *Journal of Electronic Materials*, 42(7):2014–2019, 2013.

[45] H. Scherrer and S. Scherrer. *Thermoelectrics Handbook: Macro to Nano*, chapter 27. CRC Press LLC, Boca Raton, 2006.

[46] H. Liu, X. Yuan, P. Lu, X. Shi, F. Xu, Y. He, Y. Tang, S. Bai, W. Zhang, L. Chen, Y. Lin, L. Shi, H. Lin, X. Gao, X. Zhang, H. Chi, and C. Uher. Ultrahigh Thermoelectric Performance by Electron and Phonon Critical Scattering in $Cu_2Se_{1-x}I_x$. *Advanced Materials*, 25(45):6607–6612, 2013.

[47] L. Zhao, X. Wang, F. F. Yun, J. Wang, Z. Cheng, S. Dou, J. Wang, and G. J. Snyder. The Effects of Te^{2-} and I^- Substitutions on the Electronic Structures, Thermoelectric Performance, and Hardness in Melt-Quenched Highly Dense $Cu_{2-x}Se$. *Advanced Electronic Materials*, (1400015), 2015.

[48] H. Wang, X. Cao, Y. Takagiwa, and G. J. Snyder. Higher mobility in bulk semiconductors by separating the dopants from the chargeconducting band – a case study of thermoelectric PbSe. *Materials Horizons*, 2015.

[49] J. W. Harrison and J. R. Hauser. Alloy Scattering in Ternary III-V Compounds. *Physical Review B*, 13(12):5347–5350, 1976.

[50] Copper selenides (Cu_2Se, $Cu_{2-x}Se$) optical and further properties. In O. Madelung, U. Rossler, and M. Schulz, editors, *Non-Tetrahedrally Bonded Elements and Binary Compounds I*, volume 41C of *Landolt-Börnstein - Group III Condensed Matter*, chapter 77, pages 1–6. Springer Berlin Heidelberg, 1998.

[51] *Semiconductor Thermoelements and Thermoelectric Cooling.* Infosearch, London, 1960.

[52] H. J. Goldsmid. Increasing the thermoelectric figure of merit for bismuth and bismuth-antimony. In I. Kim, editor, *PROCEEDINGS ICT 07: TWENTY-SIXTH INTERNATIONAL CONFERENCE ON THERMOELECTRICS*, pages 362–365. International Thermoelectrics Society, 2007.

[53] E. F. Hampl. U. s. patent 3,853,632. Technical report, Minnesota Mining and Manufacturing Company, 1974.

[54] S. Ballikaya, H. Chi, J. R. Salvador, and C. Uher. Thermoelectric Properties of Ag-Doped Cu_2Se and Cu_2Te. *Journal of Materials Chemistry A*, 1(40):12478–12484, 2013.

[55] S. Miyatani. Electronic and Ionic Conduction in $(Ag_xCu_{1-x})_2Se$. *Journal of the Physical Society of Japan*, 34(2):423–431, 1973.

[56] S. Ishiwata, Y. Shiomi, J. S. Lee, M. S. Bahramy, T. Suzuki, M. Uchida, R. Arita, Y. Taguchi, and Y. Tokura. Extremely high electron mobility in a phonon-glass semimetal. *Nature Materials*, 12(6):512–517, 2013.

[57] Y. Pei, A. D. LaLonde, S. Iwanaga, and G. J. Snyder. High thermoelectric figure of merit in heavy hole dominated PbTe. *Energy and Environmental Science*, 4(6):2085–2089, 2011.

[58] Y. I. Ravich, B. A. Efimova, and I. A. Smirnov. *Semiconducting Lead Chalcogenides*. Plenum Press, 1970.

[59] A. A. Voskanyan, P. N. Inglizyan, S. P. Lalykin, I. A. Plyutto, and Y. M. Shevchenko. Electrical properties of copper selenide. *Soviet Physics Semiconductors*, 12(11):1251–1253, 1978.

[60] Y. Pei, H. Wang, and G. J. Snyder. Band engineering of thermoelectric materials. *Advanced Materials*, 24(46):6125–6135, 2012.

[61] B. A. Mansour, F. El Akkad, and T. Hendeya. Electrical and thermoelectric properties of some copper chalcogenides. *Physica Status Solidi A*, 62(2):495–501, 1980.

[62] T. Day, C. P. Heinrich, W. G. Zeier, G. J. Snyder, and W. Tremel. Effect of Isovalent Substitution on the Thermoelectric Properties of the $Cu_2ZnGeSe_{4-x}S_x$ Series of Solid Solutions. *Journal of the American Chemical Society*, 136(1):442–448, 2014.

[63] C. Lee, Y. Park, and H. Hashimoto. Effect of nonstoichiometry on the thermoelectric properties of a Ag_2Se alloy prepared by a mechanical alloying process. *Journal of Applied Physics*, 101(2):024920, 2007.

[64] G. B. Haxel, J. B. Hedrick, and G. J. Orris. Rare earth elements—critical resources for high technology. Technical Report Fact Sheet 087-02, United States Geological Survey, 2002.

[65] Y. Pei, A. D. LaLonde, H. Wang, and G. J. Snyder. Low effective mass leading to high thermoelectric performance. *Energy and Environmental Science*, 5(7):7963–7969, 2012.

[66] A. F. May, J. P. Fleurial, and G. J. Snyder. Thermoelectric performance of lanthanum telluride produced via mechanical alloying. *Physical Review B*, 8(12):125205, 2008.

[67] T. Caillat, A. Borschevsky, and J. P. Fleurial. Properties of single crystalline semiconducting $CoSb_3$. *Journal of Applied Physics*, 80(8):4442–4449, 1996.

[68] D. M. Rowe, editor. *Thermoelectrics Handbook*. CRC Press, 1995.

[69] D. M. Rowe, editor. *Thermoelectrics Handbook: Macro to Nano*. CRC Press, 2006.

[70] G. A. Wiegers. Electronic and Ionic Conduction of Solid Solutions $Ag_{2-x}Au_xSe$ ($0 \leq x \leq 0.5$). *Journal of the Less-Common Metals*, 48(2):251–268, 1976.

[71] S. Miyatani. Ionic Conduction in β-Ag_2Te and β-Ag_2Se. *Journal of the Physical Society of Japan*, 14(8):996–1002, 1959.

[72] S. Miyatani, Y. Toyota, T. Yanagihara, and K. Iida. α-Ag_2Se as a Degenerate Semiconductor. *Journal of the Physical Society of Japan*, 23(1):35–43, 1967.

[73] R. Dalven and R. Gill. Energy Gap in β-Ag_2Se. *Physical Review*, 159(3):645–649, 1967.

[74] C. M. Fang, R. A. de Groot, and G. A. Wiegers. Ab initio band structure calculations of the low-temperature phases of Ag_2Se, Ag_2Te and Ag_3AuSe_2. *Journal of Physics and Chemistry of Solids*, 63(3):457–464, 2002.

[75] H. J. Goldsmid and J. W. Sharp. Estimation of the thermal band gap of a semiconductor from Seebeck measurements. *Journal of Electronic Materials*, 28(7):869–872, 1999.

[76] A. F. May and G. J. Snyder. *Thermoelectrics and its Energy Harvesting*. CRC Press LLC, Boca Raton, 2012.

[77] Y. Z. Pei, N. A. Heinz, and G. J. Snyder. Alloying to increase the band gap for improving thermoelectric properties of Ag_2Te. *Journal of Materials Chemistry*, 21(45):18256–18260, 2011.

[78] P. G. Klemens. Thermal resistance due to point defects at high temperatures. *Physical Review*, 119(2):507–509, 1960.

[79] M. H. Hebb. Electrical conductivity of silver sulfide. *Journal of Chemical Physics*, 20(1):185–190, 1952.

[80] S. Miyatani and Y. Suzuki. On the electric conductivity of cuprous sulfide: Experiment. *Journal of the Physical Society of Japan*, 8(5):680–681, 1953.

[81] J. B. Boyce and B. A. Huberman. Superionic conductors: Transitions, structures, dynamics. *Physics Reports*, 51(4):189–265, 1979.

[82] A. Zunger. Practical doping principles. *Applied Physics Letters*, 83(1):57–59, 2003.

[83] Q. Xu, B. Huang, Y. F. Zhao, Y. F. Yan, R. Noufi, and S. H. Wei. Crystal and electronic structures of Cu_xS solar cell absorbers. *Applied Physics Letters*, 100(6):061906, 2012.

[84] H. T. Evans. Crystal structure of low chalcocite. *Nature Physical Science*, 232(29):69–70, 1971.

[85] S. Kashida, W. Shimosaka, M. Mori, and D. Yoshimura. Valence band photoemission study of the copper chalcogenide compounds, Cu_2S, Cu_2Se and Cu_2Te. *Journal of Physics and Chemistry of Solids*, 64(12):2357–2363, 2003.

[86] D. J. Chakrabarti and D. E. Laughlin. The Cu-S (Copper-Sulfur) system. *Bulletin of Alloy Phase Diagrams*, 4(3):254–271, 1983.

[87] E. Hirahara. The physical properties of cuprous sulfides-semiconductors. *Journal of the Physical Society of Japan*, 6(6):422–427, 1951.

[88] L. W. Wang. High Chalcocite Cu_2S: A Solid-Liquid Hybrid Phase. *Physical Review Letters*, 108(8):085703, 2012.

[89] E. S. Toberer, A. Zevalkink, and G. J. Snyder. Phonon engineering through crystal chemistry. *Journal of Materials Chemistry*, 21(40):15843–15852, 2011.

[90] H. Wang, Y. Z. Pei, A. D. LaLonde, and G. J. Snyder. Weak electron–phonon coupling contributing to high thermoelectric performance in n-type PbSe. *Proceedings of the National Academy of Science*, 109(25):9705–9709, 2012.

[91] D. G. Cahill, S. K. Watson, and P. O. Rohl. Lower limit to the thermal conductivity of disordered crystals. *Physical Review B*, 46(10):6131–6140, 1992.

[92] F. Gronvold and E. F. Westrum. Thermodynamics of copper sulfides. 1. Heat capacity and thermodynamic properties of copper (I) sulfide, Cu_2S, from 5 K to 950 K. *Journal of Chemical Thermodynamics*, 19(11):1183–1198, 1987.

[93] G. A. Slack. *Solid State Physics*, volume 34, chapter 22. Academic Press, New York, 1979.

[94] C. Chiritescu, D. G. Cahill, N. Nguyen, D. Johnson, A. Bodapati, P. Keblinksi, and P. Zschack. Ultralow thermal conductivity in disordered, layered WSe_2 crystals. *Science*, 315(5810):351–353, 2007.

[95] N. A. Heinz, T. Ikeda, Y. Z. Pei, and G. J. Snyder. Applying quantitative microstructure control in advanced functional composites. *Advanced Functional Materials*, 24(15):2135–2153, 2013.

[96] M. Schwall, L. M. Schoop, S. Ouardi, B. Balke, C. Felser, P. Klaer, and H. J. Elmers. Thermomagnetic Properties Improved by Self-Organized Flower-Like Phase Separation of Ferromagnetic $Co_2Dy_{0.5}Mn_{0.5}Sn$. *Advanced Functional Materials*, 22(9):1822–1826, 2012.

[97] M. Zebarjadi, G. Joshi, G. Zhu, B. Yu, A. Minnich, Y. Lan, X. Wang, M. Dresselhaus, Z. Ren, and G. Chen. Power factor enhancement by modulation doping in bulk nanocomposites. *Nano Letters*, 11(6):2225–2230, 2011.

[98] Y. Z. Pei, N. A. Heinz, A. D. LaLonde, and G. J. Snyder. Combination of large nanostructures and complex band structure for high performance thermoelectric lead telluride. *Energy and Environmental Science*, 4(9):3640–3645, 2011.

[99] D. Vashaee and A. Shakouri. Improved thermoelectric power factor in metal-based superlattices. *Physical Review Letters*, 92(10):106103, 2004.

[100] W. G. Zeier, A. D. LaLonde, Z. M. Gibbs, C. P, M. Panthofer, G. J. Snyder, and W. Tremel. Influence of a Nano Phase Segregation on the Thermoelectric Properties of the p-Type Doped Stannite Compound $Cu_{2+x}Zn_{1-x}GeSe_4$. *Journal of the American Chemical Society*, 134(16):7147–7154, 2012.

[101] E. H. Putley. *The Hall Effect and Related Phenomena*. Butterworths, London, 1960.

[102] S. Wang. *Solid-State Electronics*. McGraw-Hill, 1966.

[103] D. Stroud. Generalized effective-medium approach to the conductivity of an inhomogeneous material. *Physical Review B*, 12(8):3368–3373, 1975.

[104] A. Minnich and G. Chen. Modified effective medium formulation for the thermal conductivity of nanocomposites. *Applied Physics Letters*, 91(7):073105, 2007.

[105] C. W. Nan, R. Birringer, D. R. Clarke, and H. Gleiter. Effective thermal conductivity of particulate composites with interfacial thermal resistance. *Journal of Applied Physics*, 81(10):6692–6699, 1997.

[106] B. Xu and M. J. Verstraete. First Principles Explanation of the Positive Seebeck Coefficient of Lithium. *Physical Review Letters*, 112(19):196603, 2014.

[107] C. M. Jaworksi, M. D. Nielsen, H. Wang, S. N. Girard, W. Cai, W. D. Porter, M. G. Kanatzidis, and J. P. Heremans. Valence-band structure of highly efficient p-type thermoelectric PbTe-PbS alloys. *Physical Review B*, 87(4):045203, 2013.

[108] V. Jovovics and J. P. Heremans. Measurements of the energy band gap and valence band structure of $AgSbTe_2$. *Physical Review B*, 77(24):245204, 2008.

[109] K. Kashida and J. Akai. X-ray diffraction and electron microscopy studies of the room-temperature structure of Cu_2Se. *Journal of Physics C: Solid State Physics*, 21(31):5329–5336, 1988.

[110] M. Levy and M. P. Sarachik. Measurement of the Hall coefficient using van der Pauw method without magnetic field reversal. *Review of Scientific Instruments*, 60(7):1342–1343, 1989.

[111] R. L. Petritz. Theory of an Experiment for Measuring the Mobility and Density of Carriers in the Space-Charge Region of a Semiconductor Surface. *Physical Review*, 110(6):1254–1262, 1958.

[112] V. Guttal and D. Stroud. Nonsaturating magnetoresistance and Hall coefficient reversal in a model composite semiconductor. *Physical Review B*, 73(8):085202, 2006.

[113] L. A. Apresyan and D. V. Vlasov. On the Depolarization Factors for Anisotropic Ellipsoids in Anisotropic Media. *arXiv:1303.7341*, 2013.

[114] M. K. Balapanov, R. K. Ishembetov, Y. K. Yulaeva, and R. A. Yakshibaev. Thermodynamic Properties of Solid Solutions of Superionic Copper, Silver, and Lithium Chalcogenides. *Russian Journal of Electrochemistry*, 47(12):1337–1342, 2011.

[115] T. Ikeda, N. J. Marolf, K. Bergum, M. B. Toussaint, N. A. Heinz, V. A. Ravi, and G. J. Snyder. Size control of Sb_2Te_3 Widmanstatten precipitates in thermoelectric PbTe. *Advanced Functional Materials*, 59(7):2679–2692, 2011.

[116] N. A. Heinz, T. Ikeda, and G. J. Snyder. Formation of highly oriented large nanoscale In_2Te_3 precipitates in bulk Bi_2Te_3. *Acta Materialia*, 60(11):4461–4467, 2012.